The isotopic composition of CO_2 and H_2O_v fluxes in a managed beech forest

Instrument tests and ecological application
of two laser-based absorption spectrometers

Dissertation
to attain the doctoral degree (Dr. rer. nat.)
of the Faculty of Forest Sciences and Forest Ecology
Georg-August-Universität Göttingen

Submitted by
Jelka Braden-Behrens
born on the 21st March 1986 in Bremen

Göttingen, 04/2018

1. Referee: Prof. Dr. Alexander Knohl
2. Referee: Prof Dr. David Bowling
3. Referee: Prof. Dr. Dirk Hölscher
Date of oral examination: 05.06.2018

Abstract: The isotopic composition of CO_2 and H_2O_v fluxes in a managed beech forest - Instrument tests and ecological application of two laser-based absorption spectrometers

Stable isotopes provide valuable insights into the coupled carbon dioxide (CO_2) and water vapor (H_2O_v) cycle on scales ranging from one leaf to global. In particular for applications under field conditions, recent progress in laser-based measurement techniques enhanced the potential of stable isotope research to investigate CO_2 and water vapor (H_2O_v) exchange processes. Here we present two experiments which use two laser-based infrared spectrometers and two ecosystem-scale methods to measure isotopic compositions of different parts of the CO_2 and H_2O_v cycle. Both experiments were carried out in a managed beech forest in central Germany and simultaneously analyze two isotopes. We measured δ^{13}C and δ^{18}O of nighttime CO_2 exchange (respiration) with the Keeling plot method as well as δ^{18}O and δD of evapotranspiration (ET) with the eddy covariance method. The two laser spectrometers used in this study were newly designed and developed and needed rigorous instrument tests. Thus, we present instrument characteristics such as accuracy and precision for both analyzers. Our results show that, with an intense calibration strategy, the accuracy and precision of the two laser-based analyzers are comparable to other more frequently used laser-based spectrometers. Combining these two spectrometers with the two ecosystem-scale methods enabled us to capture the temporal variability of the different flux components with uncertainties below the observed seasonal variability. With the Keeling plot approach, the uncertainty of the measured isotopic composition of nighttime CO_2 exchange is 0.8‰ for both δ^{13}C and δ^{18}O (based on 90 min timescale) and the uncertainty of the eddy covariance measurements of the isotopic composition of ET is 0.5 ‰ for δ^{18}O and 1 ‰ for δD (on hourly timescale). The obtained time series directly reveal distinct characteristics of the underlying processes, such as a sharp (30 ‰ in 10 days) decrease in the δ^{18}O composition of nighttime CO_2 exchange after a short and early snow event. In the case of ET, the dual isotope approach (i.e. a plot in the δ^{18}O-δD-plane) allows to separate the transpiration-dominated from the evaporation-dominated periods. Further, correlating the isotopic composition of nighttime CO_2 exchange with potential meteorological drivers, we found that for the period when the ecosystem was a net CO_2 sink the δ^{13}C of nighttime CO_2 exchange is linked to net radiation. This correlation has a time-lag consistent with the time lag between assimilation and respiration. However, the sign of this correlation disagrees with an interpretation of this correlation with ^{13}C discrimination during assimilation. Regarding the isotopic composition of H_2O_v above the forest, we found no evidence that ET dominantly drives its temporal variability on both diurnal and seasonal timescale, even if measured close to the canopy and when transpiration is high. Conclusively this thesis shows that measurements of the stable isotopic compositions in CO_2 and H_2O_v fluxes provide additional information about the underlying processes. Simultaneous measurements of δ^{13}C and δ^{18}O in CO_2 on the one hand and simultaneous measurements of δ^{18}O and δD in H_2O_v on the other hand highlight the potential of instruments capable of dual isotope analysis.

Key words:
Stable isotopes, carbon dioxide, water vapor, eddy covariance, Keeling plot, respiration, evapotranspiration

Zusammenfassung: Die Isotopenkomposition von CO_2 und H_2O_v Flüssen in einem bewirtschafteten Buchenwald - Instrumententests und ökologische Anwendung zweier laserbasierter Absorptionsspektrometer

Stabile isotope bieten wertvolle Einblicke in den gekoppelten Kohlendioxid (CO_2) und Wasserdampf (H_2O_v) Kreislauf auf Skalen von einem Blatt bis hin zu globalen Skalen. Vor allem bezogen auf Anwendungen unter Feldbedingungen haben neuere Entwicklungen laserbasierter Messtechniken das Potential der Erforschung von CO_2- und H_2O_v-Austauschprozessen mittels stabiler Isotope verstärkt. Hier stellen wir zwei Experimente vor, in denen zwei laserbasierte Infrarotspektrometer und zwei Methoden auf Ökosystemskala genutzt werden um die Isotopenkomposition verschiedener Komponenten des CO_2 und H_2O_v Kreislaufs zu messen. Beide Experimente wurden in einem bewirtschafteten Buchenwald in Mitteldeutschland durchgeführt und analysieren jeweils zwei Isotope gleichzeitig. Wir haben die δ^{13}C- and δ^{18}O-Komposition des nächtlichen CO_2-Austauschs (Respiration) mit der Keeling-Plot-Methode gemessen, sowie die δ^{18}O- und δD-Komposition der Evapotranspiration (ET) mit der Eddy-Kovarianz-Methode. Die beiden hier verwendeten Laserspektrometer sind neu konzipiert und entwickelt und bedurften umfassenden Instrumententests. Deswegen zeigen wir Instrumentencharakteristika für beide Spektrometer, beispielsweise bezüglich Präzision und Genauigkeit. Unsere Ergebnisse zeigen, dass mit einer intensiven Kalibrierstrategie Präzisionen und Genauigkeiten erreicht werden, die vergleichbar zu denen anderer häufiger genutzter laserbasierter Spektrometern sind. Die Kombination der beiden Spektrometer mit den beiden Methoden auf Ökosystemskala ermöglichte die Erfassung der zeitlichen Variabilität der verschiedenen Flusskomponenten mit Unsicherheiten die kleiner sind als die gemessene saisonale Variabilität. Die Unsicherheit der mit der Keeling-Plot-Methode gemessenen Isotopenkomposition des nächtlichen CO_2-Austauschs ist 0.8 ‰ für δ^{13}C sowie δ^{18}O (auf 90 min Zeitskala) und die Unsicherheit der mit der Eddy-Kovarianz-Methode gemessenen Isotopenkomposition der ET ist 0.5 ‰ für δ^{18}O und 1 ‰ für δD (auf stündlicher Zeitskala). Die gemessenen Zeitreihen lassen direkt bestimmte Eigenschaften der zugrundeliegenden Prozesse erkennen, wie eine deutliche Abnahme der δ^{18}O-Komposition des nächtlichen CO_2-Austauschs im Anschluss an ein kurzes und frühes Schneeereignis. Im Falle der ET erlaubt der Ansatz der dualen Isotopenanalyse (d.h. ein Plot in der δ^{18}O-δD-Ebene) eine Unterscheidung zwischen evaporations- und transpirationsdominierten Perioden. Darüber hinaus fanden wir durch die Korrelation der Isotopenkomposition des nächtlichen CO_2-Austauschs mit potenziellen meteorologischen Treibern heraus, dass die δ^{13}C-Werte der Respiration für die Zeitperiode in welcher der Wald eine CO_2-Senke darstellt mit der gemessenen Nettostrahlung zusammenhängt. Diese Korrelation hat einen zeitlichen Abstand, der mit der Zeit zwischen Assimilation und Respiration übereinstimmt. Das Vorzeichen dieser Korrelation hingegen widerspricht einer Interpretation dieser Korrelation über ^{13}C-Diskriminierung während der Assimilation. Bezogen auf die Isotopenkomposition des H_2O_v über dem Wald, fanden wir keinerlei Hinweise darauf, dass ET die gemessene zeitliche Variation dominiert - weder auf täglicher noch auf saisonaler Zeitskala, insbesondere auch nah über dem Blattwerk und während einer Zeit großer Transpiration. Abschließend folgern wir, dass die Messung der Isotopenkomposition in CO_2 and H_2O_v-Flüssen zusätzliche Informationen über die zugrunde liegenden Prozesse

liefert. Die simultane Messung von $\delta^{13}C$ und $\delta^{18}O$ in CO_2 sowie von $\delta^{18}O$ und δD in H_2O_v hebt zudem das Potential von Messgeräten hervor, die zwei Isotope gleichzeitig analysieren können.

Schlagwörter: Stabile Isotope, Kohlenstoffdioxid, Wasserdampf, Eddy-Kovarianz, Keeling-Plot, Respiration, Evapotranspiration

Declaration

I hereby declare that I wrote this PhD thesis under the supervision of Prof. Alexander Knohl. Any sources of information and used literature have been acknowledged.

Göttingen, April 2018 Jelka Braden-Behrens

Contents

CHAPTER 1

Introduction

1.1 Background: Using stable isotopes to trace CO_2 and H_2O exchange

1.1.1 CO_2 and H_2O exchange processes between the atmosphere and the biosphere

Biogeochemical cycles play an important role in the global climate system and to achieve a better understanding of their role, research on the atmosphere-ecosystem exchange of trace gases is fundamental (Moncrieff et al., 1997b). In this thesis, I focus on the analysis of biosphere-atmosphere carbon dioxide (CO_2) and water vapor (H_2O_v) exchange processes of a managed beech forest on an ecosystem scale, shown in Fig. 1.1. The main processes that yield an exchange of CO_2 between the atmosphere and the biosphere are photosynthesis and respiration. In a forest ecosystem, photosynthesis takes place in different canopy layers (understory/overstory), plant species, and parts of the plants (sun and shade leafs). Similarly, ecosystem integrated respiration is composed of respiration from the soil, the stem, and the leaves. Respiration can be divided into autotrophic respiration[1] (the utilization of newly assimilated carbon by living plants) and heterotrophic respiration (the utilization of dead plant material by microorganisms), as described e.g. by Affek et al. (2014). The main processes that yield an exchange of H_2O between the ecosystem and the atmosphere are precipitation and evapotranspiration (ET), the latter being composed of evaporation and transpiration. Additionally, dew formation can remove H_2O_v from the SBL. In a forest ecosystem, evaporation can originate from different sources such as from soil, wet vegetation, rivers and lakes (see e.g. Rosenberg, 1974) or falling raindrops (see

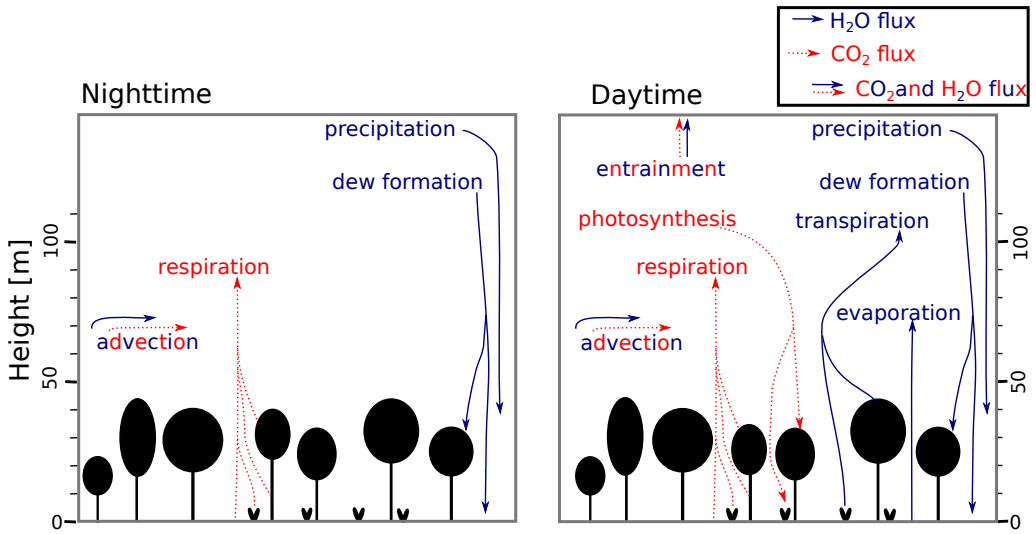

Figure 1.1: CO_2 fluxes (red dashed arrows) and H_2O fluxes (blue dashed arrows) in the surface boundary layer (SBL) above a forest ecosystem during nighttime (left) and daytime (right).

1 In particular with respect to soil respiration, the term 'autotrophic' is used inconsistently among different authors. In this thesis, I use the term 'authotrophic soil respiration' synonymously to 'root-derived soil respiration', which includes respiration from the living root tissue, rhizomicrobial respiration and respiration from mycorrhizal symbiotic funghi (cf. Moyano et al., 2009).

e.g. Ambach et al., 1968). Transpiration on the other hand is defined as the evaporation of water that has passed through the plants (see e.g. Rosenberg, 1974).

The measured H_2O_v and CO_2 mole fractions in the surface boundary layer (SBL) are further influenced by additional exchange processes that are not directly related to the local ecosystem, such as advection and entrainment (cf. Fig. 1.1 and 1.2). While advection is horizontal transport due to mean horizontal wind, entrainment is related to boundary layer growth and mixes air from the free atmosphere into the atmospheric boundary layer (ABL), as described e.g. by Stull (1988). As the air entrained into the boundary layer from above contains less CO_2 and H_2O_v than the air in the ABL, entrainment yields a net CO_2 and H_2O_v removal from the ABL (see also Lee et al., 2006, for H_2O). On an initially cloud-free day, starting from a stable boundary layer at midnight, the turbulent mixing layer develops about half an hour after sunrise (Stull, 1988). As the turbulence in the mixing layer is normally convectively driven (Stull, 1988), this layer is also called the convective mixing layer. In general, the characteristic of the atmosphere-biosphere exchange processes in the SBL varies from the addition/removal of the respective flux component to a stably stratified atmosphere (more prevalent during nighttime) to turbulent transport (more prevalent during daytime), cf. Fig. 1.2. This has some consequences for the applicability of different methods to measure fluxes on an ecosystem scale, as discussed in section 1.2.

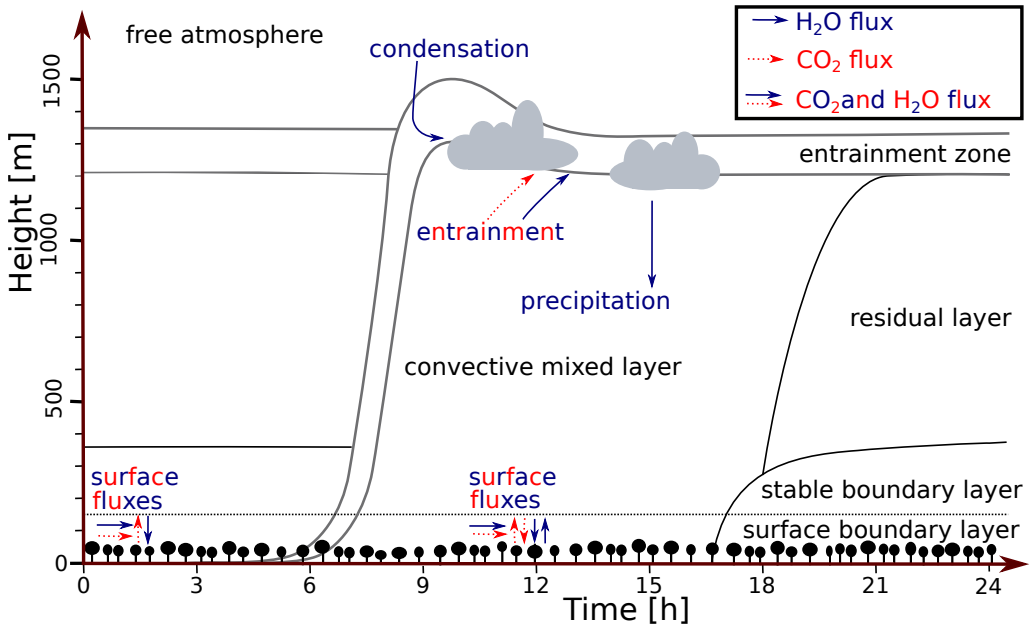

Figure 1.2: CO_2 fluxes (red dashed arrows) and H_2O fluxes (blue dashed arrows) above a forest ecosystem in combination with the evolution of the convective boundary layer throughout the day (top panel). This graph is adapted from (Stull, 1988)[a]

a This graph is an adapted version of a graph provided by the wikimedia commons user 'Lethepku' and underlies the creative commons licence https://creativecommons.org/licenses/by-sa/3.0/deed.en .

1.1.2 Stable isotopes in atmosphere-ecosystem CO_2 and H_2O_v exchange processes

The analysis of stable isotopes[1] in carbon dioxide (CO_2) and water vapor (H_2O_v) provides valuable insights into atmosphere-ecosystem exchange processes (see e.g. Dawson et al., 2002; Griffis, 2013; Yakir et al., 2000). Such insights are particularly relevant, because terrestrial ecosystems play an important role in the variability of atmospheric CO_2 (Conway et al., 1994; Schimel, 1995; Yakir et al., 2000) and H_2O_v (Jasechko et al., 2013; Wang et al., 2000). Isotopic measurements can be used to assess the spatial and temporal dynamics of atmospheric CO_2 and H_2O_v (Lee et al., 2009; Wang et al., 2000). Applications of stable-isotope-based techniques for CO_2 and H_2O_v range from leaf and branch scale measurements (e.g. Dubbert et al., 2014; Gentsch et al., 2014; Wang et al., 2010) to global scale modeling (Ciais et al., 1995; Jasechko et al., 2013).

The biophysical cause of the applicability of stable isotope techniques to study biosphere-atmosphere exchange processes is that different exchange components can have different isotopic compositions due to a) variable isotopic compositions of the source material and b) due to fractionation processes. Fractionation processes can be divided into equilibrium (also: thermodynamic) fractionation and non-equilibrium (also: kinetic) fractionation (Farquhar et al., 1989). Examples for equilibrium fractionation processes are the phase transitions between water (or ice) and water vapor under thermodynamic equilibrium (Ellehoj et al., 2013; Majoube, 1970; Majoube, 1971). In these cases, the different exchange rates of isotopologues (i.e. molecules with different isotopic composition)[2] are related to their different water vapor pressures (see e.g. Ellehoj et al., 2013). Examples for non-equilibrium fractionation processes are diffusion, evaporation and the ^{13}C discrimination of photosynthetic CO_2 uptake. Evaporation (e.g. from the sea surface) is related to the relative humidity above the water body and can be described by the Craig and Gordon model (Craig et al., 1965) in many cases. The ^{13}C discrimination, i.e. the plants preference of the lighter ^{12}C atom during photosynthesis, on the other hand depends on CO_2 supply and demand (Farquhar et al., 1989). Thus, ^{13}C discrimination depends on the multiple meteorological drivers of stomatal conductance and photosynthesis (Farquhar et al., 1989). In many cases, ^{13}C discrimination during photosynthesis can be described by the Farquar model (Farquhar et al., 1989).

Multiple applications make use of fractionation effects and the (resulting) individual isotopic compositions of different ecosystem components to study processes in the CO_2 and H_2O_v cycle. One important application that uses the isotopic composition of different fluxes and flux components is the partitioning of a net flux into its components. In the case of CO_2 flux, stable isotope measurements have been used to partition the net CO_2 flux into photosynthesis and respiration (e.g. Bowling et al., 2001; Knohl et al., 2005a; Ogée

1 Stable isotopes are non-radioactive atoms of the same element with different numbers of neutrons in the core. Isotopic compositions of a certain element can be reported as isotope ratios $R := c_{heavy}/c_{light}$, with the concentrations c_{heavy} and c_{light} of the heavier and lighter isotope. Conventionally, an arbitrarily chosen standard material with an isotopic ratio R_{std} is used to define the δ value as the relative deviation of the isotope ratio R from R_{std} (the ratio of the standard material). Thus, $\delta := (R - R_{std})/R_{std}$.

2 The term isotopologues is used here following the definition by Coplen (2011) as 'molecular species that differ only in isotopic composition'.

et al., 2003; Oikawa et al., 2017; Wehr et al., 2016; Yakir et al., 1996; Zhang et al., 2006). Also for H_2O, stable isotope measurements have been used to partition ET into evaporation and transpiration (e.g. Dubbert et al., 2013; Hu et al., 2014; Lu et al., 2017; Wang et al., 2015; Wei et al., 2015; Wen et al., 2016; Xu et al., 2016). However, besides flux partitioning, there are numerous other applications in which stable isotopes were used to provide additional information about biosphere-atmosphere exchange processes. Examples are the use of stable isotopes in H_2O to study the water uptake depth of plants (Meissner et al., 2014) or the partitioning of understory and overstory vegetation (Yepez et al., 2003). For CO_2, further examples of the potential of stable isotope research are the quantification of the time lag between assimilation and respiration (Bowling et al., 2002; Ekblad et al., 2001; Knohl et al., 2005b) or the measurement of the ratio between above ground and below ground respiration (Fassbinder et al., 2012).

1.2 Methods: Ecosystem scale measurements of isotopic compositions

On an ecosystem scale, three methods are available to evaluate the isotopic composition of a flux: the Keeling plot, the flux gradient, and the eddy covariance method. The different underlying assumptions, advantages, and limitations of these methods are discussed in the following paragraphs.

1.2.1 The Keeling plot method

The Keeling plot method (Keeling, 1958) describes how molecules (e.g. CO_2 or H_2O molecules) from one source mix with a background gas. The basic assumption of this method is the mixing of only one source (with constant isotopic composition δ_s) with a background (with constant isotopic composition δ_{bg}). If this assumption is fulfilled, the following equation can be derived from the conservation of mass for all (relevant) isotopologues (see e.g. Pataki et al., 2003):

$$\delta_{\text{meas}} = (\delta_{bg} - \delta_s)\, C_{bg}\ \frac{1}{C_{\text{meas}}} + \delta_s \tag{1.1}$$

With the measured mole fraction C_{meas}, the isotopic composition δ_{meas}, and the molecule's background mole fraction C_{bg}. Thus, the intercept of a linear regression of δ_{meas} against $1/C_{\text{meas}}$ equals the isotopic composition of the source δ_s. The measured concentrations and isotopic compositions that are used in this linear regression can be based on measurements that are taken at different times at the same position (temporal Keeling plot), at different positions (spatial Keeling plot), or both (spatial-temporal Keeling plot) as described e.g. by Galewsky et al. (2016). A modification of the Keeling plot, the Miller-Tans plot (Miller et al., 2003), has been discussed as an alternative to the Keeling plot method. In brief, for a Miller-Tans plot equation 1.1 is multiplied with C_{meas}. Based on the resulting equation, different authors use different definitions of the Miller-Tans plot that a) use the slope of the resulting linear regression between $(\delta_{\text{meas}} \cdot C_{\text{meas}})$ and C_{meas} without adding additional information about δ_{bg} and C_{bg} (see e.g. Alstad et al., 2007; Zobitz et al., 2006) or b) use the same slope but add measurements or approximations of δ_{bg} and C_{bg} to estimate δ_s (Miller et al., 2003). On an ecosystem scale, Keeling plot or Miller-Tans plot applications have been performed for $\delta^{13}C$ in CO_2 (e.g. Alstad et al., 2007; Barbour

et al., 2011; Bowling et al., 2002; Knohl et al., 2005b; Miller et al., 2003; Pataki et al., 2003; Tuzson et al., 2008), for $\delta^{18}O$ in CO_2 (e.g. Bowling et al., 2003a; Bowling et al., 2003b; Shim et al., 2013) or for $\delta^{18}O$ and δD in H_2O_v (e.g. Good et al., 2012; Moreira et al., 1997; Yepez et al., 2003) in various ecosystems. However, all these applications rely on the assumption of the mixing of only one source (or a source that can be treated as an integrated source) with an isotopic composition δ_s that is constant in space, time or both (depending on the application). For all applications (except for those Miller-Tans plot that additionally measure the background), one additionally assumes that C_{bg} and δ_{bg} are constant in space, time or both (depending on the application). These assumptions have been discussed to be questionable in many situations in particular for H_2O (Lee et al., 2012a; Lee et al., 2006; Noone et al., 2013) but also for CO_2 (Griffis et al., 2007), in particular when the mole fraction footprint largely exceeds the flux footprint. In the present study, a spatial-temporal Keeling plot approach is used to measure the isotopic composition of nighttime respiration in a managed beech forest (see chapter 2). In this chapter, the Keeling plot method is described and discussed more detailed and the measures to assure and test the applicability of the Keeling plot approach are discussed in section 2.11.1.

1.2.2 The flux gradient method

The flux gradient method relates gradient measurements of a molecule's mole fraction C to the eddy flux density F_C of this molecule (Hatfield et al., 2005) and is based on Monin-Obukhov stability theory (Kaimal et al., 1994; Monin et al., 1954). If the mole fraction C only depends on the height z (which means $\frac{\partial C}{\partial z} = \frac{\mathrm{d}C}{\mathrm{d}z}$), the flux gradient method can be described by the following formula:

$$F_C = -k_C \, \rho_a \, \frac{\mathrm{d}C}{\mathrm{d}z} \tag{1.2}$$

With the eddy diffusivity k_C and the molar air density ρ_a. In the case of isotope applications, the fluxes for the different isotopologues are divided by each other and a common eddy diffusivity k_C is assumed for both isotopologues. Thus the isotopic composition of the eddy flux density F_C is directly proportional[1] to the gradient $\frac{\mathrm{d}C^{\mathrm{A}}}{\mathrm{d}C^{\mathrm{B}}}$, with A and B indicating two different isotopologues (see e.g. Griffis et al., 2007). Flux gradient methods have been widely used to measure the isotopic composition of fluxes for both, H_2O_v (Good et al., 2012; Hu et al., 2014; Huang et al., 2014; Lee et al., 2007; Wang et al., 2016; Welp et al., 2008; Wen et al., 2016) and CO_2 (Griffis et al., 2007; Griffis et al., 2008; Griffis et al., 2004; Zhang et al., 2006). However, the Monin-Obukhov similarity theory that underlies the flux gradient method is typically only applicable in the lowest 10 % of the ABL (see e.g. Hatfield et al., 2005). Additionally, flux gradient measurements can be subject to roughness sublayer effects if measurements are carried out too close to tall vegetation (see e.g. Denmead et al., 1985; Hatfield et al., 2005). Thus, flux gradient measurements have limited applicability above forest ecosystems (see also Griffis, 2013).

1 The exact formula for this relation depends on the geometry of the molecule (cf. Eq 3.4).

1.2.3 The eddy covariance method

The eddy covariance (EC) method directly relates the turbulent motions in the SBL to the flux of a molecule (or another scalar). This method is based on the assumptions that turbulence is fully developed, the terrain below the flux measurement is homogeneous, the data is stationary, and that density fluctuations are negligible (Foken et al., 1996). Under these assumptions, and when the vertical wind velocity and the molecule's mole fraction C is measured fast enough (typically with a measurement frequency of 10 to 20 Hz), the turbulent flux of the molecule is directly related to the high-frequency time series of C and w (see e.g. Baldocchi, 2003; Stull, 1988).

$$F_C = \bar{\rho_a}\,\overline{w'C'} := \bar{\rho_a}\,\frac{\int_0^T w'(t)C'(t)\mathrm{d}t}{\int_0^T \mathrm{d}t} \tag{1.3}$$

With the molecule's eddy flux density F_C and the mean density of air $\bar{\rho_a}$. Following micrometeorological convention, overbars denote temporal means and primes denote fluctuations from the mean (Reynolds averaging, i.e. $w'{=}w - \bar{w}$). Similar to the flux gradient approach, the isotopic composition of the flux δ_F is linearly related to the ratio of the eddy flux densities $F^{\mathrm{A}}/F^{\mathrm{B}}$, with A and B as indicators for two different isotopologues (see Eq. 3.4 for the case of ET). EC measurements of the isotopic composition of ET have been carried out for δ^{18}O by (Griffis et al., 2010; Griffis et al., 2011) and (based on slow measurements) for both, δD and δ^{18}O (Good et al., 2012). EC measurements of the isotopic composition of an ecosystem's net CO_2 flux have been carried out for both, ^{13}C and ^{18}O (Griffis et al., 2008; Griffis et al., 2011; Sturm et al., 2012; Wehr et al., 2013). Similar to the other methods presented here, the EC technique shows limited applicability when the above mentioned assumptions are violated. This is for example the case when turbulence is not fully developed (particularly during nighttime). However, compared to flux gradient and Keeling plot measurements, the EC method that is based on first principles, relies on fewer assumptions (Griffis, 2013). In chapter 3 of this thesis, the eddy covariance method is used to measure the isotopic composition of evapotranspiration. In this chapter, also a more detailed description of this method is presented.

1.3 Tools: Optical-based instruments to study the stable isotope composition

A widely used and well-established technique to study the stable isotopic composition of a molecule is isotope ratio mass spectrometry (IRMS, see e.g. Sevastyanov, 2015, for details). This technique separates moving ions with different mass-to-charge ratio in an orthogonal magnetic field and is originally based on the work of Thomson (1908). However, in the last decade, progress in optical techniques provides new optical-based analyzers that can complement or even compete with traditional IRMS measurements (Werner et al., 2012). Optical instruments are in particular useful for field applications (Griffis, 2013). In this thesis, I present and characterize two different optical-based instruments to study the isotopic composition of a molecule in air. In order to provide a framework for a better understanding of the used instruments and to enable a comparison of these analyzers to other optical-based instruments, here I present a classification scheme for optical-based analyzers. This scheme is a slightly modified version of a classification scheme

for laser-based measurements at trace gas concentrations proposed by Kerstel et al. (2008): One major classification of optical-based instruments can be done with respect to the light source that is used, between 1. broadband-light-source-based instruments and 2. laser-based instruments. A further distinction can be made, that defines three classes of laser-based spectrometers (a) direct absorption spectrometers in mid infrared, where strong absorption features are available (b) absorption spectrometers in near infrared that compensate the weaker absorption in near infrared by a strongly enhanced effective optical path length and (c) path-length-enhanced absorption spectrometers in mid infrared. Different instruments of these classes are listed in Table 1.1 for analyzers that measure δD and/or δ^{18}O in H_2O_v, together with literature reports of their minimum Allan deviations (if available) as a measure of precision. A similar table is presented for instruments that measure δ^{13}C and/or δ^{18}O in CO_2 in chapter 2 (see Table 2.2). Please note that there is an instrument of class 2(c) in the case of CO_2, but there is no such instrument for H_2O_v. A short description of the fundamental measurement principles and the most commonly used technical implementations for the different categories of optical instruments (including broadband-light-source-based as well as laser-based instruments) is given here.

1. **Broadband-light-source-based instruments**
   In Fourier transform infrared (FTIR) spectrometers the complete infrared spectrum of a black body light source is used. The emitted infrared light is modulated by an interferometer that is (in many cases) based on a Michelson interferometer (Griffiths et al., 2007) and the resulting interferogram is converted into the absorption spectrum mathematically by applying a Fourier transformation (Griffith et al., 2012). Even if the broadband light source used in an FTIR is generally much weaker than a laser light source, similar precision to laser-based instruments and IRMS could be reached with FTIR for averaging times of 10 minutes (cf. Tables 1.1 and 2.2). FTIR analyzers have been used for example to measure δD (and δ^{18}O) in H_2O_v (Cai et al., 2015; Haverd et al., 2011) and to measure δ^{13}C (and δ^{18}O) in CO_2 (Griffith et al., 2012; Vardag et al., 2015).

2. **Laser-based instruments**
   In laser absorption spectrometers a laser beam with tunable wavelength is sent through a (multi-path or resonant) absorption cell, usually operating at low pressure and the light intensity of the emerging laser beam is measured by a suitable detector (Werle, 2004).

   a) **Laser-based direct absorption spectrometers in mid infrared** directly capture a molecule's rotational-vibrational absorption spectrum in mid infrared (Kerstel et al., 2008). As the absorption features (especially in the case of CO_2) are stronger in mid infrared (wavelength between 3 and 50 μm) than in near infrared (wavelength between 0.8 and 3 μm), instruments of this kind typically achieve signal-to-noise ratios that are suitable for trace gas concentrations. Different implementations of this type of spectrometers use different kinds of lasers. For CO_2, quantum cascade laser spectrometers (QCLAS, *Aerodyne Research Inc., Boston, USA*), were used e.g. by Sturm et al. (2012) or Wehr

et al. (2016). Likewise for CO_2, a non-linear crystal is used to produce a mid infrared laser in the isotope ratio infrared spectrometer (IRIS „Delta Ray Analyzer“, *Thermo Scientific, Bremen, Germany*) used e.g. by Geldern et al. (2014) and Rizzo et al. (2014). Further, a lead-salt diode laser spectrometer (TGA100A/200, *Campbell Scientific Inc., Logan, USA*), was used for CO_2 by Bowling et al. (2005) and Bowling et al. (2003c) and for H_2O_v by Wen et al. (2008). The TGA100A/200 requires cryogenic cooling and is no longer manufactured (Griffis, 2013).

b) **Laser-based path-length-enhanced-absorption spectrometers in near infrared** measure the rotational-vibrational absorption spectra for the isotopologues in near infrared, where absorption features are typically weaker than in mid infrared. To increase the number of absorbed photons while the laser beam passes through the absorption cell, the optical path length is increased by using high finesse optical cavities (Kerstel et al., 2008). There are two mayor technical implementations of this approach that are both related to the decay of light intensity after the laser is switched of (Griffis, 2013): cavity ringdown spectroscopy (CRDS), e.g. the G1101-i and G1101-i+ *Picarro Inc.,Santa Clara, USA* see e.g. (Aemisegger et al., 2012; Vogel et al., 2013), and off-axis integrated cavity output spectroscopy (OA-ICOS), e.g. the different models of water vapor isotope analyzers (WVIA and WVIA-EP) *Los Gatos Research Inc., San Jose, USA* see e.g. (Aemisegger et al., 2012; Guillon et al., 2012; Sturm et al., 2009). CRDS measures the exponential decay time after the laser is switched off, and relates this decay time to the absorption of laser light. For OA-ICOS, the measured quantity that is linked to the absorption of laser light is the time-integrated radiation intensity that is leaking out of the cavity (Aemisegger et al., 2012).

c) **Laser-based path-length-enhanced absorption spectrometers in mid infrared** combine the wavelength range in mid infrared that is also used by instruments of type 2.a) with an enhanced optical path length that is used by instruments of type 2.b). An example for an instrument of category 2.c) is the CCIA-48 *Los Gatos Research. Inc, San Jose, San Jose, USA* that combines a mid-infrared quantum cascade laser with off-axis integrated cavity output spectroscopy (Oikawa et al., 2017).

For the research presented in this thesis, we used two laser-based instruments, the isotope ratio infrared spectrometer (IRIS „Delta Ray Analyzer“, *Thermo Scientific, Bremen, Germany*) and the high flow and high-frequency enabled water vapor isotope analyzer (2 Hz-HF-WVIA, *Los Gatos Research Inc., San Jose, USA*). The IRIS Delta Ray belongs to category 2.(a), i.e. it is a direct laser-based absorption spectrometer in mid infrared. This analyzer uses a nonlinear crystal in combination with two tunable near infrared diode lasers to produce a laser beam in mid infrared by difference frequency generation (DFG) (Thermo Fisher Scientific, 2014). The used laser scans a wavelength around 4.33 μm (Geldern et al., 2014) and has an optical path length around 5 m (Thermo Fisher

Scientific, 2014). The 2 Hz-HF-WVIA on the other hand belongs to the category 2.b), i.e. it is a laser-based path-length-enhanced absorption spectrometers in near infrared. This analyzer is an off-axis integrated cavity output spectrometer in the near infrared that scans a region around 1.39 μm (Aemisegger et al., 2012) and has an enhanced optical path length of up to 2500 m (Los Gatos Research Inc., 2013).

Table 1.1: Examples for different optical instruments that measure the isotopic composition of H_2O and reported values for minimal Allan deviations σ_A and the corresponding averaging times $\tau_{\min}$ (if not available, another definition of precision is used), see also Table 2 of the review by Griffis (2013). The indicees a) to d) refer to different definitions of precision: a) one standard deviation of the calibrated values for repeated measurements; b) the standard error of prediction from the regressions used for calibration; c) one standard deviation of the difference between the measured value from that calculated with the Rayleigh distillation model; d) no definition found.

1. Broadband light source based instruments	
Instrument:	Fourier transform infrared spectrometer:
	Bruker IRcube *Bruker Optics, Germany*
Precision[b] for δD :	$\sigma(\tau$=120 $s) \approx$1-3 ‰ for C_{H2O} between 5000 and 15000 ppm (Haverd et al., 2011)
Instrument:	Fourier transform infrared spectrometer: , *no name, no manufacturer*
Precision[d] (δD) :	$\sigma(\tau$=600 $s) \approx$1 ‰ for C_{H2O} between 5000 and 30000 ppm (Cai et al., 2015)
Precision[d] (δ^{18}O) :	$\sigma(\tau$=600 $s) \approx$0.4 ‰ for C_{H2O} between 5000 and 30000 ppm (Cai et al., 2015)
2. a) laser-based direct absorption spectrometers in mid infrared	
Instrument:	Lead-salt tunable diode laser absorption spectrometer: TGA100A/200,
	Campbell Scientific Inc., USA
Precision[c] (δ^{18}O)	$\sigma(\tau$=60 min)$\approx$ 0.07 at C_{H2O} app. 16000 ppm (Wen et al., 2008)
Precision[c] (δD)	$\sigma(\tau$=60 min)$\approx$ 1.1 at C_{H2O} app. 16000 ppm (Wen et al., 2008)
2. b) laser-based path-length-enhanced absorption spectrometers in near infrared	
Instrument:	Cavity ringdown spectrometer: L1115-i, *Picarro Inc., USA*
Minimal Allan deviation (δD) :	$\sigma_A(\tau_{\min}\approx$15 min) = 0.06 ‰at C_{H2O} app. 16000 ppm (Aemisegger et al., 2012)
Minimal Allan deviation (δ^{18}O) :	$\sigma_A(\tau_{\min}\approx$50 min) = 0.01 ‰at C_{H2O} app. 16000 ppm (Aemisegger et al., 2012)
Instrument:	Cavity ringdown spectrometer: L2130-i, *Picarro Inc., USA*
Minimal Allan deviation (δD) :	$\sigma_A(\tau_{\min}\approx$170 min) = 0.02 ‰at C_{H2O} app. 16000 ppm (Aemisegger et al., 2012)
Minimal Allan deviation (δ^{18}O) :	$\sigma_A(\tau_{\min}\approx$100 min) =0.006 ‰at C_{H2O} app. 16000 ppm (Aemisegger et al., 2012)
Instrument:	Off-axis integrated cavity output spectrometer:
	WVIA, *Los Gatos Research Inc., USA*
Minimal Allan deviation (δD) :	$\sigma_A(\tau_{\min}\approx$10 min) = 0.07 ‰at C_{H2O} app. 16000 ppm (Aemisegger et al., 2012)
	$\sigma_A(\tau_{\min}\approx$15 min) = 0.04 at C_{H2O} app. 14000 ppm(Sturm et al., 2009)
Minimal Allan deviation (δ^{18}O) :	$\sigma_A(\tau_{\min}\approx$170 min) = 0.07 at C_{H2O} app. 16000 ppm (Aemisegger et al., 2012)
	$\sigma_A(\tau_{\min}\approx$15 min) = 0.03 at C_{H2O} app. 14000 ppm (Sturm et al., 2009)
Instrument:	Off-axis integrated cavity output spectrometer:
	WVIA-EP, *Los Gatos Research Inc., USA*
Minimal Allan deviation for δD :	$\sigma_A(\tau_{\min}\approx$7 min) = 0.02 ‰at C_{H2O} app. 16000 ppm (Aemisegger et al., 2012)
Minimal Allan deviation for δ^{18}O :	$\sigma_A(\tau_{\min}\approx$30 min) = 0.01 ‰at C_{H2O} app. 16000 ppm (Aemisegger et al., 2012)

1.4 Structure of the thesis

The PhD thesis 'The isotopic composition of CO_2 and H_2O_v fluxes in a managed beech forest' presents research to investigate CO_2 and H_2O_v exchange processes between the atmosphere and a forest in central Germany. The background of this thesis are the underlying physical and meteorological processes i.e. the relevant fluxes and isotope selective fractionation processes are described in chapter 1.1. The three main methods that are commonly used to study isotopic compositions on an ecosystem scale (Keeling plot method, flux gradient method and eddy covariance) are briefly discussed in section 1.2. In this section, I also discuss their main assumptions and major limitations. Further, the available tools for stable isotope analysis (i.e. IRMS and optical-based spectrometers) are explained in section 1.3. Further, the setup, the measured flux, the method and the used instrument (tool) of the experiments presented in this theses are summarized in Figure 1.3 in the context of the characteristics of the SBL.

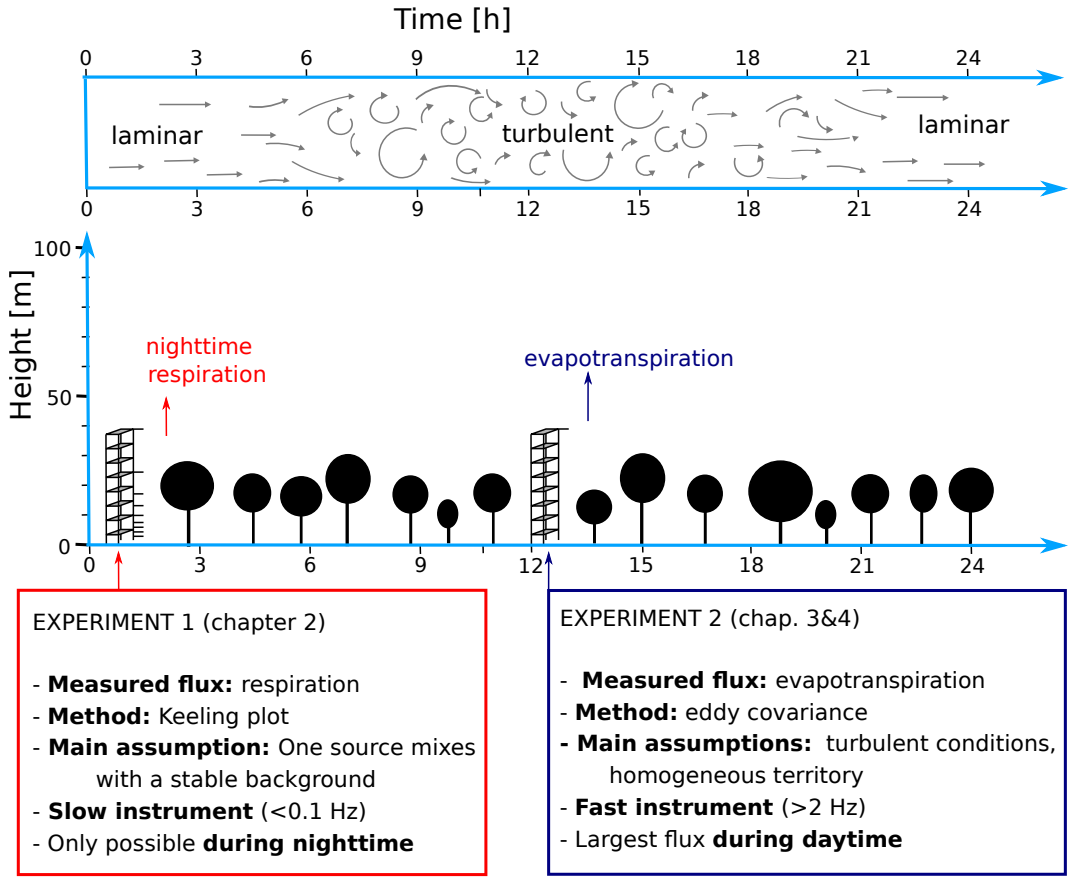

Figure 1.3: Short profile of the two experiments that are carried out in this thesis in the context of boundary layer flow.

The introduction of the background, the available methods on an ecosystem scale, and the available tools is followed by the three main chapters of this thesis (chapter 2 to 4). Each of these main chapters presents a scientific contribution based on stable isotope analysis in CO_2 and H_2O_v fluxes in a managed beech forest on an ecosystem scale. The three scientific contributions are the following:

- **A new instrument for stable isotope measurements of ^{13}C and ^{18}O in CO_2 - Instrument performance and ecological application of the Delta Ray IRIS analyzer**

  Jelka Braden-Behrens, Yuan Yan and Alexander Knohl, published in *Atmospheric Measurement Techniques* (Braden-Behrens et al., 2017a); chapter 2 of this thesis

  In this publication, we use a laser-based direct absorption spectrometer in mid infrared (Delta Ray, *Thermo Scientific Inc.*, Waltham, USA) to measure the isotopic composition of respiration with a Keeling plot approach. This analyzer measures the CO_2 mole fraction C_{CO2} and isotopic composition of $\delta^{13}C$ and $\delta^{18}O$ in CO_2 with an effective measurement frequency below 0.1 Hz. The analyzer used in this study is a newly developed commercially available analyzer and thus, we needed to rigorously test and characterize the analyzer. With instrument tests, we quantify instrument characteristics such as the dependency of the measured (raw) δ values from the respective CO_2 mole fraction, as well as the analyzers' precision and potential accuracy. In the field application, we chose a Keeling plot approach to measure the isotopic composition of nighttime respiration in a managed beech forest. For this purpose, the more direct EC method would suffer from the prevalent absence of turbulence during nighttime and also the flux gradient method has limited applicability above the tall vegetation at this site. We discuss the observed seasonal variability and further focus on the influence of an early snow event on the measured isotopic composition of nighttime CO_2 flux. Additionally, we focus on the question in which extend the measured ^{13}C composition of respiration can be explained by the Farquar model of photosynthesis.

- **Eddy covariance measurements of the dual-isotope composition of evapotranspiration**

  Jelka Braden-Behrens, Christian Markwitz and Alexander Knohl, Manuscript to be submitted to *Agricultural and Forest Meteorology* (Braden-Behrens et al., 2018b); chapter 3 of this thesis

  In this manuscript, we use a laser-based path-length-enhanced absorption spectrometer in mid-infrared (2 Hz-HF-WVIA, *Los Gatos Research. Inc.*, San Jose, CA, USA) for EC measurements of the isotopic composition of H_2O_v. This instrument is a modified version of an often-used commercially available instrument (EP-WVIA, *Los Gatos Research. Inc.*, San Jose, CA, USA), that is optimized for fast (> 2 Hz) measurements of the water vapor mole fraction C_{H2O} and its isotopic composition in δD and $\delta^{18}O$. As this analyzer was highly modified and e.g. was used at a different flow rate than the standard instrument, we first tested and characterized the analyzer in this manuscript. For example, we measured the mole fraction range dependency of

the measured δ values and evaluate the analyzer's precision and accuracy. We used this analyzer to measure the isotopic composition of evapotranspiration (ET) in a managed beech forest with the EC technique. The EC technique is used here as it is the most direct technique and both, the flux gradient technique and the Keeling plot technique are expected to have limited applicability in this setup (e.g. due to roughness effects and temporal changes in the background mole fraction and isotopic composition).

- **Does local evapotranspiration drive seasonal and diurnal variations in the isotopic composition of water vapor above a managed beech forest?**

  Jelka Braden-Behrens and Alexander Knohl, Manuscript to be submitted to *Biogeosciences*; chapter 4 of this thesis

  In this manuscript, we use the time series of the isotopic composition of water vapor and evapotranspiration obtained in chapter 3 to answer the question : 'What drives the observed seasonal and diurnal variations in the isotopic composition of water vapor (δ_v) above a managed beech forest?' We present different possible drivers of the isotopic composition of H_2O_v such as entrainment, local ET and Rayleigh distillation and discuss their influence on δ_v. On diurnal timescale this discussion is based on the observed mean diurnal cycles and on seasonal scale this discussion is based on correlations with (meteorological) quantities that are related to different processes that potentially drive of δ_v, such as fractionation, ET, Rayleigh distillation, or turbulent mixing.

The last chapter of this thesis contains a summary of the main results and conclusions, followed by a broader discussion of dual isotope approaches. The two different laser spectrometers that were used in this thesis are capable of dual isotope analysis and in the synopsis, I further discuss the use of dual isotope (or even dual species approaches) in this thesis and in related work as well as the large potential of dual isotope approaches for future research.

1.5 Related publications

- **Measuring the isotopic composition of ecosystem respiration in a temperate beech forest**

  Jelka Braden-Behrens, Alexander Knohl, Hans-Jürg Jost and Magda Mandic, Non-peer reviewed publication *Thermo Scientific White Paper* (Braden-Behrens et al., 2017b)

  In this short technical publication, we present the setup of the experiment to measure the isotopic composition of respiration in a managed beech forest (chapter 2). Additionally we show some first results of the instrument tests (described in more detail in chapter 2 of this thesis) and discuss some obtained diurnal cycles of the isotopic composition of net CO_2 exchange.

1.6 Objectives

In brief, the objectives of this theses are

- **to characterize and test two different laser-based absorption spectrometers for measurements of the stable isotope composition in CO_2 and H_2O_v;**
  This objective is addressed for the isotope ratio infrared analyzer for CO_2 (Delta Ray, *Thermo Scientific Inc.*, Waltham, USA) in chapter 2 and for the high-frequency and high-flow-rate-optimized water vapor isotope analyzer (2 Hz-HF-WVIA, *Los Gatos Research. Inc.*, San Jose, CA, USA) in chapter 3.
- **to use these analyzers in combination with ecosystem scale methods to assess different parts of the coupled CO_2 and H_2O cycle in a managed beech forest in central Germany;**
  This refers to the measurement of the isotopic composition of nighttime respiration (chapter 2) and to the measurement of the isotopic composition of evapotranspiration (chapter 3).
- **and to use the obtained datasets to provide insights into the underlying processes.**
  In particular, we use the observed isotopic compositions of respiration and evapotranspiration to answer the following questions:
  - In how far can we explain the variability of the ^{13}C isotopic composition of respiration by the isotopic composition of recent assimilates which is in turn controlled by meteorological drivers during photosynthesis? (Chapter 2)
  - Does local evapotranspiration drive the diurnal and seasonal variability of the isotopic composition of water vapor δ_v in the SBL? (Chapter 4)

CHAPTER 2

A new instrument for stable isotope measurements of ^{13}C and ^{18}O in CO_2 - Instrument performance and ecological application of the Delta Ray IRIS analyzer

published in 'Atmospheric measurement techniques' (Braden-Behrens et al., 2017a)

2.1 Abstract

We used the recently developed commercially available Delta Ray isotope ratio infrared spectrometer (IRIS) to continuously measure the CO_2 mole fraction C_{CO2} and its isotopic composition $\delta^{13}C$ and $\delta^{18}O$ in a managed beech forest in central Germany. Our objectives are (a) to characterize the Delta Ray IRIS and evaluate its internal calibration procedure and (b) to quantify the seasonal variability of c, $\delta^{13}C$, $\delta^{18}O$ and the isotopic composition of nighttime net ecosystem CO_2 exchange (respiration) $R^{13}_{eco}C$ and $R^{18}_{eco}O$ derived from Keeling plot intercepts. The analyzer's minimal Allan deviation (as a measure of precision) was below 0.01 ppm for the CO_2 mole fraction and below 0.03 ‰ for both δ values. The potential accuracy (defined as the 1σ deviation from the respective linear regression that was used for calibration) was approximately 0.45 ppm for c, 0.24 ‰ for ^{13}C and 0.3 ‰ for ^{18}O. For repeated measurements of a target gas in the field, the long-term standard deviation from the mean was 0.3 ppm for C_{CO2} and below 0.3 ‰ for both δ values. We used measurements of nine different inlet heights to evaluate the isotopic compositions of nighttime net ecosystem CO_2 exchange $R^{13}_{eco}C$ and $R^{18}_{eco}O$ in a 3 month measurement campaign in a beech forest in autumn 2015. During this period, an early snow and frost event occurred, coinciding with a change in the observed characteristics of both $R^{13}_{eco}C$ and $R^{18}_{eco}O$. Before the first snow, $R^{13}_{eco}C$ correlated significantly ($p< 10^{-4}$) with time-lagged net radiation R_n, a driver of photosynthesis and photosynthetic discrimination against ^{13}C . This correlation became insignificant ($p> 0.1$) for the period after the first snow, indicating a decoupling of $\delta^{13}C$ of respiration from recent assimilates. For ^{18}O, we measured a decrease of 30 ‰ within 10 days in $R^{18}_{eco}O$ after the snow event, potentially reflecting the influence of ^{18}O depleted snow on soil moisture. This decrease was 10 times larger than the corresponding decrease in $\delta^{18}O$ in ambient CO_2 (below 3 ‰) and took 3 times longer to recover (3 weeks vs. 1 week). In summary, we conclude that 1) the new Delta Ray IRIS with its internal calibration procedure provides an opportunity to precisely and accurately measure c, $\delta^{13}C$ and $\delta^{18}O$ at field sites and 2) even short snow or frost events might have strong effects on the isotopic composition (in particular ^{18}O) of CO_2 exchange on an ecosystem scale.

2.2 Introduction

The stable isotopic compositions of CO_2 and water vapor have been intensely used to study ecosystem gas exchange (Yakir et al., 2000). In particular, measurements of the $\delta^{13}C$ and $\delta^{18}O$ isotopic composition of CO_2 have provided important insights into the carbon cycle over a large variety of spatial and temporal scales (Affek et al., 2014; Flanagan et al., 1998). There are many examples for the utility of the stable isotopic composition of CO_2 to study biosphere-atmosphere exchange processes on an ecosystem scale, such as the partitioning of net ecosystem CO_2 exchange into respiration and photosynthesis. Different partitioning methods include the combination of gradient approaches with stable isotope measurements (Yakir et al., 1996), direct isotope gradient approaches (Zhang et al., 2006), the combination of eddy covariance measurements with isotope flask measurements (Bowling et al., 2001; Knohl et al., 2005a; Ogée et al., 2003), and direct isotope eddy covariance measurements (Oikawa et al., 2017; Wehr et al., 2016). Other field

applications of stable CO_2 isotopes measurements investigate the temporal variability of the isotopic composition of a particular flux component. The temporal variability of the isotopic composition of respiration for example has been studied on timescales ranging from sub-diurnal (Barbour et al., 2011) to seasonal (Bowling et al., 2002; Ekblad et al., 2001; Knohl et al., 2005b). Further, the isotopic composition in CO_2 profiles has been studied on several sites over multiple years for ^{13}C (e.g. Bowling et al., 2002; Wehr et al., 2016) as well as for ^{18}O (e.g. Bowling et al., 2003a; Shim et al., 2013). The ^{13}C composition of ecosystem respiration $R^{13}_{eco}C$, on the one hand, has been used to assess the time lag between assimilation and respiration (Bowling et al., 2002; Ekblad et al., 2001; Knohl et al., 2005b) and to evaluate biosphere models on a global scale (Ballantyne et al., 2011). The ^{18}O composition of ecosystem CO_2 exchange $R^{18}_{eco}O$, on the other hand, is particularly interesting for studying the coupled CO_2 and water cycle (see e.g. Yakir et al., 1996).

A long-established and broadly used technique to measure stable isotopic compositions is isotope ratio mass spectrometry (IRMS) (Griffis, 2013), a technique that is based on the fact that moving ions with different mass-to-charge ratios can be separated by (orthogonal) magnetic fields (Thomson, 1908). For measurements of the isotopic composition of CO_2, IRMS has typical precisions of approximately 0.02 to 0.1 ‰ for ^{13}C and 0.05 to 0.2 ‰ for ^{18}O. IRMS has been widely used for isotope studies in environmental sciences, though it shows limited applicability for *in situ* measurements (Griffis, 2013) , but see also the field-applicable continuous flow IRMS described by Schnyder et al. (2004). Disadvantages of flask-sampling-based IRMS techniques include high sample preparation effort and costs (Griffis, 2013), low temporal resolution and discontinuous measurements. Additionally, there are potential problems during sample storage and transport, see Knohl et al. (2004) for minimizing such storage effects in the case of ^{13}C. For ^{18}O, storage effects can be related to oxygen exchange between water and CO_2 (Gemery et al., 1996; Tuzson et al., 2008). Optical-based techniques can compete with or complement IRMS measurements, and progress in optical-based techniques over the last decade has enhanced the potential of measurements of isotopic compositions (Werner et al., 2012). These developments have a particular impact on micrometeorological studies, as they increased the accessibility of field-deployable optical instruments and thus enabled a number of micrometeorological applications of stable isotope techniques, as reviewed by Griffis (2013). Optical instruments to study the isotopic composition of trace gases use the absorption of infrared photons by exciting a molecule's rotational and vibrational energy states. These rotational and vibrational transitions are characteristically different for isotopologues, defined for example by Coplen (2011) as 'molecular species that differ only in isotopic composition', (see e.g. Esler et al., 2000; Kerstel et al., 2008)[1]. The isotopologue-specific absorption lines are related to the mole fraction of the respective isotopologue via Beer's law and thus the isotopic composition of a certain molecule (Werle,

1 In general this is also true for isotopomers, defined for example by Coplen (2011) as 'molecular species having the same number of each isotopic atom [...] but differing in their positions.' (e.g. Mohn et al., 2008).

2004). Available optical instruments that are capable of measuring isotopic compositions at trace gas mole fractions show different implementations of this principle by using different light sources (broadband light sources, mid- or near-infrared lasers) (see e.g. Griffis, 2013; Kerstel et al., 2008) and/or different absorption cells (multipath or resonant) (Werle, 2004). Minimal Allan deviations σ_A and the corresponding averaging times $\tau_{\min}$ for different optical instruments are shown in Table 2.2, but see also Table 2 in the review of Griffis (2013) for more detailed information, including instrument stability and an overview of applications, for most of these instruments.

Table 2.1: Nomenclature and abbreviations used in this publication, numbers for reference standards R_{std} from International Atomic Energy Agency (1995)

Stable isotope specific nomenclature	
R_{std}	Isotope ratio $c_{\text{heavy}}/c_{\text{light}}$ of an (arbitrary) reference standard
δ value	Relative deviation of the measured isotope ratio from R_{std}
VPDB	Vienna Pee Dee Belemnite - standard for ^{13}C (R_{VPDB}≈0.01124)
VPDB-CO_2	Vienna Pee Dee Belemnite - standard for ^{18}O ($R_{\text{VPDB-CO2}}$≈0.0020883)
Nomenclature	
σ_A	Allan deviation
R_n	Net radiation
RH	Relative humidity
VPD	Vapor pressure deficit
δ_{KP}	Keeling plot intercept
R_{eco}	Isotopic composition of nighttime CO_2 exchange (respiration) integrated over the ecosystem
Technical abbreviations	
IRIS	Isotope ratio infrared spectrometer
IRMS	Isotope ratio mass spectrometer
OA-ICOS	Off-axis integrated cavity output spectroscopy
CRDS	Cavity ring down spectroscopy

Here we present a new laser-based direct absorption spectrometer in mid infrared, the isotope ratio infrared spectrometer (IRIS) Delta Ray *Thermo Scientific Inc., Waltham, USA*. This spectrometer uses two tunable near-infrared diode lasers in combination with a nonlinear crystal to produce a laser beam in the mid-infrared (Thermo Fisher Scientific, 2014). The instrument scans a spectral region from 4.3293 μm to 4.3275 μm, containing four CO_2 absorption lines: at 4.3277 μm and 4.3280 μm (both for $^{16}O^{12}C^{16}O$), 4.3283 μm (for $^{16}O^{13}C^{16}O$) and 4.3286 μm (for $^{16}O^{12}C^{18}O$) (Geldern et al., 2014). A measured and a fitted spectrum is shown in Fig. 2.1. The fitting procedure is based on a Voigt profile fit, that relates the isotopologue-specific absorption lines to their respective mole fractions (information from the manufacturer, Thermo Fisher Scientific). The instrument has a flow rate of 0.08 slpm, a cell pressure of approximately 100 mbar, an optical path length of approximately 5 m and an internal calibration procedure that automatically includes two point calibrations for mole fraction C_{CO2} and both δ values as well as corrections for the mole fraction dependency of the measured δ values (Thermo Fisher Scientific, 2014). The objectives of our study are (a) to characterize the Delta Ray IRIS and its performance under field conditions as well as (b) to quantify the seasonal variability of $\delta^{13}C$, $\delta^{18}O$ and the isotopic composition of CO_2 exchange for both $\delta^{13}C$ and $\delta^{18}O$ derived from Keeling plot intercepts.

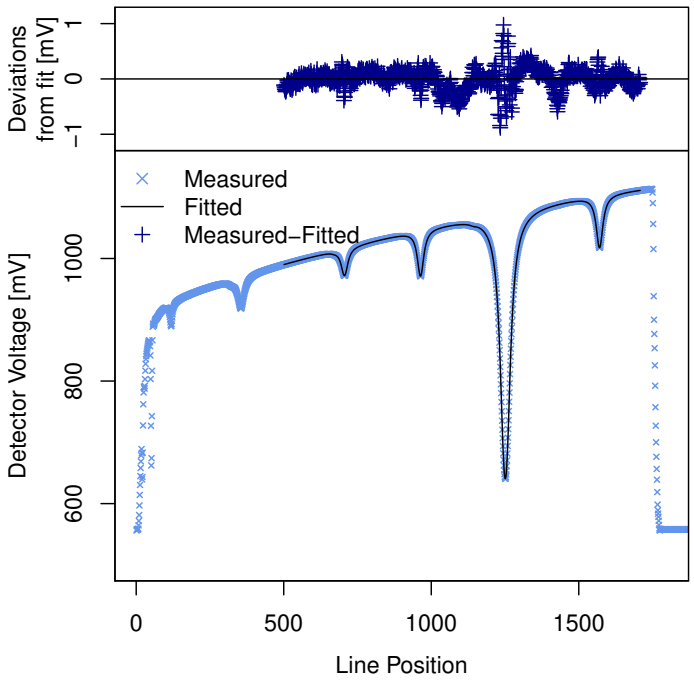

Figure 2.1: Measured and fitted spectrum, as exported from the instrument's operational software Qtegra.

Table 2.2: Examples for different optical instruments that measure the isotopic composition of CO_2 and reported values for minimal Allan deviations σ_A and the corresponding averaging times $\tau_{\min}$ (if available), see also Table 2 of the review of Griffis (2013).

Broadband-light-source-based instruments	
Instrument:	Fourier transform infrared spectrometer:
	Spectronus analyzer, *Ecotech Pty Ltd., Australia*
Minimal Allan deviation for $\delta^{13}C$:	$\sigma_A(\tau_{\min}\approx 6000\,s)=0.01\,‰$ (Griffith et al., 2012)
Minimal Allan deviation for $\delta^{18}O$:	$\sigma_A(\tau_{\min}\approx 7200\,s)=0.1\,‰$ (Vardag et al., 2015)
Instrument:	Fourier transform infrared spectrometer:
	Nicolet Avatar, *Thermo Electron, USA*
Minimal Allan deviation for $\delta^{13}C$:	$\sigma_A(\tau_{\min}\approx 960\,s)=0.15\,‰$ (Mohn et al., 2007)
Laser-based direct absorption spectrometers in mid infrared	
Instrument:	Quantum cascade laser absorption spectrometer:
	QCLAS *Aerodyne Research Inc., USA*
Minimal Allan deviation for $\delta^{13}C$:	$\sigma_A(\tau_{\min}\approx 100\,s)=0.01\,‰$ (Wehr et al., 2013)
	$\sigma_A(\tau_{\min}\approx 100\,s)=0.06\,‰$ (Sturm et al., 2012)
Minimal Allan deviation for $\delta^{18}O$:	$\sigma_A(\tau_{\min}\approx 100\,s)=0.06\,‰$ (Sturm et al., 2012)
Instrument:	Lead-salt tunable diode laser absorption spectrometer:
	TGA100A/200,
	Campbell Scientific Inc., USA
Minimal Allan deviation:	no data for uncalibrated minimal σ_A,
	ideal averaging time $\tau_{\min}\approx 30\,s$ (Bowling et al., 2003c)
High-frequency Allan deviation:	$\sigma_A(\tau=0.1\,s)=1.5\,‰$ for $\delta^{13}C$ and $2.2\,‰$ for $\delta^{18}O$ (Bowling et al., 2003c)
Instrument:	Isotope ratio infrared spectrometer:
	Delta Ray, *Thermo Scientific Inc., USA*
Minimal Allan deviation for $\delta^{13}C$:	$\sigma_A(\tau_{\min}\approx 500\,s)=0.04\,‰$ (Geldern et al., 2014);
	$\sigma_A(\tau_{\min}\approx 300\,s)=0.02\ ‰$ (this study, table 2.5)
Minimal Allan deviation for $\delta^{18}O$:	$\sigma_A(\tau_{\min}\approx 300\,s)=0.04\,‰$ (this study, table 2.5)
Laser-based path-length-enhanced absorption spectrometers in near infrared	
Instrument:	Cavity ringdown spectrometer:
	G1101-i+, *Picarro Inc., USA*
Minimal Allan deviation for $\delta^{13}C$:	$\sigma_A(\tau_{\min}\approx 3600\,s)\leq 0.1\,‰$ (Vogel et al., 2013)
Instrument:	Off-axis integrated cavity output spectrometer:
	CCIA DLT-100, *Los Gatos Research Inc., USA*
Minimal Allan deviation for $\delta^{13}C$:	$\sigma_A(\tau_{\min}\approx 200\,s)=0.04\,‰$ (at approximately 20 000 ppm CO_2) (Guillon et al., 2012);
	$\sigma_A(\tau_{\min}\approx 200\,s)=0.6\,‰$ (at approximately 2 000 ppm CO_2) (Guillon et al., 2012)
Laser-based path-length-enhanced absorption spectrometers in mid infrared	
Instrument:	Quantum cascade laser absorption spectrometer:
	CCIA-48, *Los Gatos Research Inc., USA*
Minimal Allan deviation for $\delta^{13}C$:	$\sigma_A(\tau_{\min}\approx 300\,s)=0.06\,‰$ (Oikawa et al., 2017)
Minimal Allan deviation for $\delta^{18}O$:	$\sigma_A(\tau_{\min}\approx 300\,s)=0.04\,‰$ (Oikawa et al., 2017)

2.3 Material and methods

2.3.1 Field site

This study was conducted at a meteorological tower in a managed beech forest (*Fagus sylvatica L.*) in Thuringia (central Germany) at 51°19'41,58" N; 10°22'04,08" E at 450 meters above sea level. The forest in the dominant wind direction of the tower has an average canopy height of approximately 34 m with approximately 120-year-old trees, a top-weighted canopy and a homogeneous stand structure, surrounded by trees of three age classes (approximately 30–40, 80 and 160 years), (Anthoni et al., 2004). The field site is described in detail by Anthoni et al. (2004), and soil characteristics of this site were analyzed by Mund (2004).

2.3.2 Campaign design

We measured the CO_2 mole fraction C_{CO2} and its isotopic composition $\delta^{13}C$ and $\delta^{18}O$ in ambient air from 21^{st} August 2015 to 16^{th} November 2015. We measured these quantities with the field deployable isotope ratio infrared spectrometer Delta Ray (*Thermo Scientific, Waltham, USA*) at nine inlet heights ranging from 0.1 to 45 m in an automatic measurement setup. After the tubing was purged for 60 s, each inlet was measured for 80 s, (consisting of four measurements each averaged for 20 s - thus the averaging time is longer than the instrument internal cell response time $\tau_{10\%}$ cf. section 2.4.1.4). A full measurement cycle took 30 minutes and consisted of measurements of all nine inlet heights and a target standard with known CO_2 mole fraction and isotopic composition (CO_2 in synthetic air, tank 'SA-CO_2-5 in Table 2.3), supplemented by an internal calibration measurement, called 'referencing' (cf. Sect. 2.3.8). In less detail, the experimental setup is also described in Braden-Behrens et al. (2017b).

We used the nighttime measurements of c, $\delta^{13}C$ and $\delta^{18}O$ of the different inlet heights in a Keeling plot approach (Keeling, 1958) to calculate the nighttime Keeling plot intercept that can be used to estimate the isotopic composition of nighttime net ecosystem CO_2 exchange (respiration) δR_{eco} for both measured δ values: ^{13}C and ^{18}O. Additionally, we used the half-hourly measurements of the target standard to track the repeatability of the Delta Ray analyzer and performed additional (manual) measurements to characterize the analyzer.

2.3.3 Spectrometer setup

We set up the spectrometer to use the absorption lines at 4.3277 μm (for $^{16}O^{12}C^{16}O$), 4.3283 μm (for $^{16}O^{13}C^{16}O$) and 4.3286 μm (for $^{18}O^{12}C^{16}O$). Thus, only three of the four absorption lines in the instrument's measured spectra (Fig. 2.1), were used for the spectral fit. In particular, for $^{16}O^{12}C^{16}O$, we did not use the strong absorption line at 4.3280 μm. The corresponding mode of operation is called 'high-mole fraction mode' in the instrument's operational software Qtegra. Additionally, the sample was dried before it entered the measurement cell with the (instrument's internal) Nafion drier.

2.3.4 Application of the Keeling plot approach

The Keeling plot approach (Keeling, 1958) is based on a simple two-component mixing model that describes how air from a source with effectively constant isotopic composition δ_s

Table 2.3: Known CO_2 mole fractions C_{CO2} and δ values for gas tanks used for calibration and instrument performance measurements. All measured mole fractions and δ values refer to measurements that were performed at the Max-Planck Institute for Biogeochemistry in Jena and the $\delta^{13}C$ values of the two pure CO_2 tanks. The pure CO_2 tanks 'bio' and 'ambient' were additionally measured with IRMS at the Geoscience Center in Göttingen (Isotope Geology Division, Göttingen University) for their ^{13}C composition. Abbreviations for the purpose of the tanks: cCAL=mole fraction calibration; dCAL=δ-calibration; REF=referencing; EC=evaluating calibration ; pcCAL=post mole fraction calibration; REP=repeatability measurement

Gas tank	Used for	C_{CO2} [ppm]	$\delta^{13}C$ [‰VPDB]	$\delta^{18}O$ [‰VPDB-CO_2]
Pure CO_2 (ambient)	dCAL, REF, EC	-	-9.94 ± 0.01	-17.5 ± 0.3
Pure CO_2 (bio)	dCAL, EC	-	-28.25 ± 0.01	-27.2 ± 0.3
Pure CO_2 (bio-2)	EC	-	-26.1 ± 0.3	-24.3 ± 0.3
Pressurized air 'PA-tank'	pcCAL, EC	413.7 ± 0.2	-9.7 ± 0.2	-5.3 ± 0.4
Synthetic air with CO_2 (SA-CO_2-1)	cCAL, pcCAL, EC	349.5 ± 0.1	-37.01 ± 0.02	-34.1 ± 0.4
Synthetic air with CO_2 (SA-CO_2-2)	cCAL, pcCAL	453.9 ± 0.1	-36.98 ± 0.02	-34.2 ± 0.6
Synthetic air with CO_2 (SA-CO_2-3)	pcCAL	349.6 ± 0.1	-37.02 ± 0.01	-34.3 ± 0.4
Synthetic air with CO_2 (SA-CO_2-4)	pcCAL, EC	453.2 ± 0.1	-37.02 ± 0.02	-34.8 ± 0.4
Synthetic air with CO_2 (SA-CO_2-5)	pcCAL, REP	396.5 ± 0.1	-37.02 ± 0.02	-34.7 ± 0.2
Synthetic air with CO_2 (SA-CO_2-6)	EC	496.0 ± 0.1	-37.02 ± 0.02	-34.8 ± 0.1

mixes with a background (with constant c_{bg} and δ_{bg}). For this simple two-component mixing model, one can derive a linear relationship between the measured isotopic composition δ_{meas} and the reciprocal mole fraction $1/c_{\text{meas}}$ by applying conservation of mass for the total mole fraction as well as for each isotopologue separately (for derivation see e.g. Pataki et al., 2003).

$$\delta_{\text{meas}} = \underbrace{(\delta_{bg} - \delta_s)\ c_{bg}}_{m_{\text{KP}}} \quad \frac{1}{c_{\text{meas}}} + \underbrace{\delta_s}_{\delta_{\text{KP}}} \tag{2.1}$$

This linear relationship with slope m_{KP} and intercept δ_{KP} can be derived for each isotopic species independently, so in our case for both $\delta^{13}C$ or $\delta^{18}O$. The applicability of the Keeling plot approach to a certain experimental setup essentially depends on the question of whether c_{bg}, δ_{bg} and δ_s are constant over the spatial and temporal distribution of all measurements that are taken into account for the linear regression. In this study we apply a Keeling plot approach to a forest ecosystem, aiming at measuring the isotopic composition of ecosystem-integrated CO_2 exchange. The source of CO_2 is thus composed of different individual source components i (e.g. stem, leaf and soil respiration), with each accounting

for the individual components with their isotopic compositions $\delta_{s,i}$. The corresponding isotopic composition of the integrated source δ_s can be expressed by defining α_i as the relative contributions of the individual source components to the integrated source.

$$\delta_s = \sum_i \delta_{s,i}\ \alpha_i \qquad \text{with} \qquad \sum_i \alpha_i = 1 \tag{2.2}$$

If the relative distributions among the different source components α_i produce significant changes in δ_s over the spatial and temporal distribution of measurements, the basic two-component assumption of stable δ_s is violated. During daytime the application of a Keeling plot approach on an ecosystem scale in a forest is in general problematic, as photosynthesis and respiration are two separately controlled and spatially separated processes - so we generally cannot assume spatiotemporally constant α_i. However, for nighttime, when there is only respiration, the nighttime Keeling plot intercept δ_{KP} can be interpreted as the isotopic composition of nighttime net ecosystem CO_2 exchange (respiration) $\delta^{13}\mathrm{C}\,R_{\mathrm{eco}}$ or $\delta^{18}\mathrm{O}\,R_{\mathrm{eco}}$. Measures to assure and test the applicability of this two-component approach and to improve the quality of the calculated Keeling plot intercepts are discussed and evaluated in appendix 2.11.1. In brief, they include the minimization of the sampling time for each Keeling plot, an inclusion of all inlet heights into each Keeling plot analysis to increase the CO_2 mole fraction range, data filtering and weighted averaging of Keeling plots on smaller timescales.

2.3.5 Material and technical specifications

Technical specifications of the setup including plumbing and the automatic switching unit are shown schematically in Fig. 2.2. The automatic switching unit consisted of 10 electromagnetic 3/2 directional control valves (Fig. 2.2) and was operated by a PC using software for measuring technology (ProfiLab Expert 4.0, Abacom, Germany). The operating software controlled the valve positions using two USB relay boards (Abacom, Germany). When switching the valves to a new position, the operating software additionally sent a 1 s long rectangular trigger pulse with 5 V DC to one of the Delta Ray analyzer's two different analogue input channels. One of these channels was used when a target gas measurement had to be started, while a trigger pulse at the other input channel initialized the height measurements. After the Delta Ray analyzer received one of the trigger pulses, the tubes and the measurement cell were purged for 60 s before the analyzer took measurements for 80 s. This purging time was used to ensure that the first measurement after switching contained less than 0.1% of the previously measured sample (cf. Sect. 2.4.1.4).

We used polyethylene (PE) tubes with 6 mm outer diameter and 4 mm inner diameter (Landefeld GmbH, Kassel, Germany) for the plumbing in the switching unit as well as for the nine height inlets. These inlets were additionally equipped with biweekly replaced 1.2 μm polytetrafluoroethylene PTFE membrane filters (Rettberg GmbH, Göttingen, Germany). The tubes for the 9 height inlets (cf. Fig. 2.2) were all equally long (50 m) - except for the highest inlet that had to be extended to 52 m for practical reasons. The equal (or similar) length of the inlet tubes lead to similar flow rates in the tubing system and similar inlet pressures for the analyzer regardless of the valve position. This decreased pressure

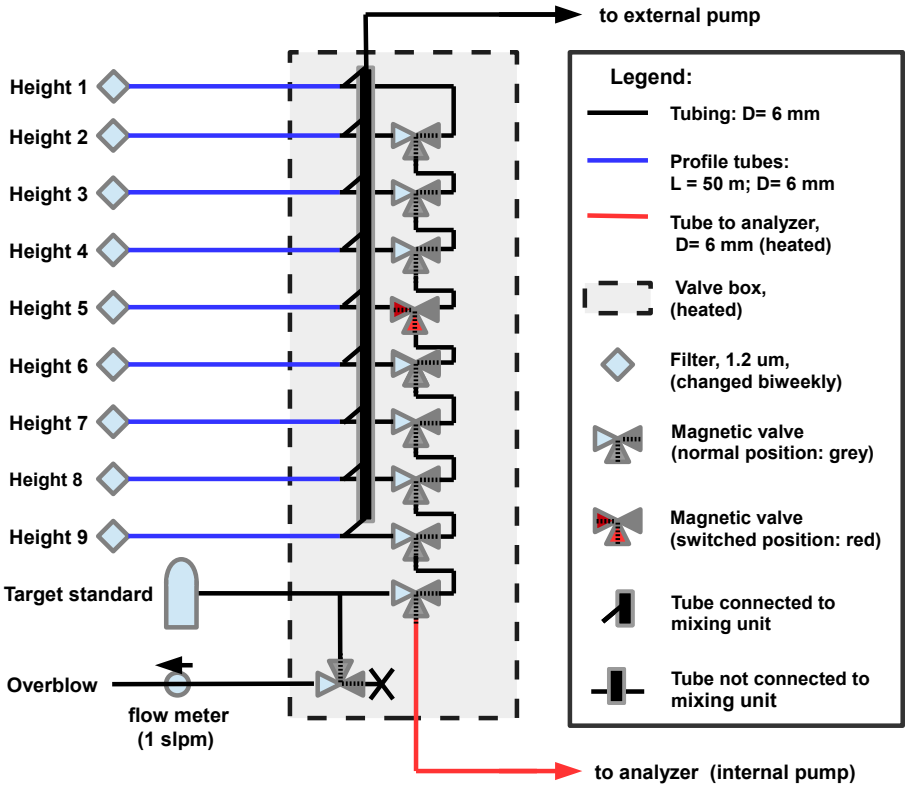

Figure 2.2: Plumbing scheme for the measurements of nine heights and a target standards, the example shows the valve positions when height 5 is sampled.

jumps when switching from one height position to another. We purged the main tube to reduce the time the air masses spend in the tubing. To avoid condensation, we heated the valve box (at which we expected a pressure drop) and the adjacent tubing. For heating we used self-regulating heating wires (Horst GmbH, Lorsch, Germany) which produce a constant temperature of 65°C. The flow rate in the height inlet tubes was approximately 1.5 slpm for all heights all the time and the major part of the gas flow was directed into the purging pump. In the case of the target standard, the tubing was only purged when the target standard was measured. In this case, an overblow opened to enable gas release at approximately 1 slpm (Fig. 2.2). For the target measurements as well as for the height measurements the analyzer took a subsample of the corresponding inlet line with a flow rate of approximately 0.08 slpm. The flow in all the tubing was laminar with Reynolds numbers below 100.

For measurements as well as calibration, we used gas tanks in 50 l steel containers at 150 to 200 bar pressure containing synthetic air, synthetic air with different CO_2 mole fractions and pressurized air (Westfalen AG, Gleichen, Germany). Additionally, we used three 1 l gas tanks at 10 bar pressure with pure CO_2 at different (known) δ values that were shipped with the Delta Ray analyzer (Air Liquide, Düsseldorf, Germany). All used CO_2-containing gas tanks were measured high precisely for their CO_2 mole fraction and

isotopic composition in ^{13}C and ^{18}O at the Max Planck Institute (MPI) for Biogeochemistry in Jena. There, the CO_2 mole fractions were measured with a Picarro CRDS G1301 and the isotopic composition was measured with IRMS linked to VPDB (VPDP-CO_2) by using the multipoint scale anchor JRA-S06 (Wendeberg et al., 2013). The pure CO_2 tanks that were used for δ calibration were additionally measured for their ^{13}C composition with IRMS at Geoscience Center in Göttingen (Isotope Geology Division, Göttingen University). All known δ values and mole fractions for the gas tanks used in this application can be found in Table 2.3 with their corresponding uncertainties.

2.3.6 Instrument characterization measurements

We carried out additional measurement in the field and in the lab to quantify precision, evaluate the calibration strategy and quantify the instrument's response time and repeatability. These measurements involved changes in the analyzers plumbing. For all measurements that required connecting different gas tanks to the analyzer, they were either connected directly to the analyzer's internal ports (Ref1, Ref2, CRef1 and CRef2) or the plumbing was equivalent to the plumbing of the target gas (Fig.2.2).

1. Lab measurements to quantify precision and evaluate the calibration strategy
    - We measured the Allan deviation by connecting pressurized air at atmospheric δ values to the analyzer and took measurements at the analyzer's maximum data acquisition rate of 1 Hz for two hours.
    - We diluted pure CO_2 with synthetic air over a CO_2 mole fraction range of 200 to 1500 ppm to measure the mole fraction dependency of the measured (raw) δ values. This dilution experiment was carried out for three different tanks with pure CO_2 at different δ values. Each gas tank was measured twice. (Used gas tanks: ambient, bio1 and bio2, cf. Table 2.3).
    - We measured the mole fraction C_{CO2} and the isotopic compositions $\delta^{13}C$ and $\delta^{18}O$ of gases with mole fractions ranging from (350 to 500 ppm) and isotopic compositions ranging from -37 to -9.7 ‰ for $\delta^{13}C$ and from -35 to -5 ‰ for $\delta^{18}O$. Each of these measurements was performed three times. (Used gas tanks: ambient, bio1, bio2, PA-tank, SA-CO_2-1,SA-CO_2-4, SA-CO_2-6; cf. Table 2.3).
    - We carried out repeated measurements of two pure CO_2 gas tanks at different δ values (diluted to different mole fractions between 200 and 3000 ppm) as well as measurements of two gas tanks at different CO_2 mole fractions (350 and 500 ppm). These measurements were repeated every 6 h for a period of 9 days. (Used gas tanks: ambient, bio, SA-CO_2-1 and SA-CO_2-6, cf. Table 2.3.)
2. Field measurements to quantify the setup's response time and repeatability.
    - The response time of the tubing and the analyzer was measured by using the automatic switching unit (Fig. 2.2) to switch from ambient air (height9) to the target standard. We superimposed the measurements of four switching events to observe the adjacent temporal response processes.
    - The analyzer's repeatability under field conditions was quantified by the half-hourly target measurements described in Sect. 2.3.5

2.3.7 Meteorological measurements

Supplementary to the measurements with the Delta Ray analyzer, the meteorological tower at the field site is equipped with an eddy covariance system to measure CO_2 and H_2O_v fluxes as well as latent and sensible heat fluxes. Additional standard meteorological measurements include continuous measurements of shortwave and longwave radiation, wind speed and direction, precipitation, air and soil temperature and air and soil humidity (Anthoni et al., 2004).

2.3.8 Calibration

2.3.8.1 Instrument internal calibration

The Delta Ray analyzer is equipped with three different internal calibration routines (Thermo Fisher Scientific, 2014). We performed these routines at the field site (*in situ*) each time the analyzer had to be restarted e.g. after power supply failures, instrument issues or when we manually turned off the analyzer for other reasons. All three instrument internal calibration procedures were usually done one day after restarting the analyzer, thus the instrument was in thermal equilibrium during calibration. The three different instrument internal calibration procedures are described below:

- *Correction of mole fraction dependency.* This correction is called 'linearity calibration' in the instrument's documentation and operational software)
  The calibration routine evaluates the mole fraction dependency of δ value measurements (Thermo Fisher Scientific, 2014). Mathematically, an experimentally derived correction factor $f_{\text{correct}}(c_{\text{raw}})$ is multiplied with the raw isotopic ratio R (information from the manufacturer, Thermo Fisher Scientific):

  $$R_{\text{c-corrected}} = f_{\text{correct}}(c_{\text{raw}}) \times R_{\text{raw}} \tag{2.3}$$

  This factor as a function of mole fraction is determined via a natural spline fit of measurements of a gas tank with constant δ value at different mole fractions (information from the manufacturer, Thermo Fisher Scientific). This is implemented by mixing pure CO_2 with CO_2-free air, yielding mole fractions between 200 and 3500 ppm. In our setup we used the pure CO_2 with near-to-ambient δ values (ambient tank , cf. Table 2.3) and synthetic air for this calibration.
- *Delta scale calibration.* This calibration routine is based on a two-point calibration of δ values using two tanks of pure CO_2 with different δ values that are diluted with synthetic air. For this calibration, we used the pure CO_2 tanks ambient and bio (cf. Table 2.3).
- *Mole fraction calibration.* This calibration routine performs a two-point calibration for CO_2 mole fraction using two gas tanks with different CO_2 mole fractions. We performed this measurement simultaneously to the other two calibration routines in the field, but for one particular calibration on 15^{th} of October, we had to replace it by a post-calibration, which is described in Sect. 2.3.8.2.

The instrument's internal calibration procedure is based on the measurement of these

calibration curves after the instrument is started in combination with repeated measurements of a known gas, so-called 'referencing' (see below). As the different calibrations are only performed once after the instrument is restarted, the accuracy and repeatability of measurements is further based on the assumption that, these relationships remain sufficiently constant, and temporal changes are corrected by 'referencing'.

- *Referencing.*
  This procedure applies an offset correction of the calibrated δ values using a gas with known δ values that is measured at a freely selectable mole fraction at regular intervals (information from the manufacturer, Thermo Fisher Scientific). In our experimental setup, referencing is carried out every 30 minutes for 80 s after the tubes have been purged for 60 s using the pure CO_2 standard ('ambient', cf. Table 2.3) diluted with synthetic air. We chose the reference mole fraction to be the same as the mole fraction at the highest inlet in the adjacent measurement cycle, because most of the measurement inlets had mole fractions close to those at the highest inlet and the temporal variability of the measured mole fractions generally decreased with height. Thus, we performed the 'referencing' as close as possible to as many height measurements as possible by using these settings.

Thus, the calibration procedure for δ values can be expressed with the following formula with the correction factor $f_{\mathrm{correct}}(c_{\mathrm{raw}})$ as determined from the mole fraction-dependency correction, and the slope $m_{\delta\mathrm{scale}}$ derived from the δ scale calibration (information from the manufacturer, Thermo Fisher Scientific).

$$\delta_{\mathrm{calibrated}}(R_{\mathrm{raw}}; c_{\mathrm{raw}}; t) = m_{\delta\mathrm{scale}} \times \underbrace{\left(\frac{f_{\mathrm{correct}}(c_{\mathrm{raw}}) R_{\mathrm{raw}}}{R_{\mathrm{std}}} - 1 \right)}_{\delta_{\mathrm{c-corrected}}(c_{\mathrm{raw}})} + \delta_{\mathrm{Offset}}(t) \tag{2.4}$$

2.3.8.2 Post-processing for mole fraction calibration

For the time period from the 15^{th} of October to 15^{th} of November, we replaced the instrument's internal mole fraction calibration by a manual linear calibration, based on manual measurements with six different gas tanks in the field. This was necessary, because measurements with these different gas tanks (including the target standard) showed a consistent linear relationship between raw and known mole fractions, that deviated from the linear relationship that was used in the instrument's internal calibration. Thus, we conclude that during this period there was a problem with the instrument's internal mole fraction calibration which might be related to gas flow or a leak during this particular mole fraction calibration.

2.3.9 Multilayer modeling

To test if the measured variability of the ^{13}C composition of respiration can be partly explained by the variability of the ^{13}C composition of recent assimilates, we used the multilayer model CANVEG to simulate the isotopic composition of assimilated material during our measurement campaign. In particular, we analyzed the correlation of modeled $^{13}C_{\mathrm{Ass}}$ with net radiation R_n, a driver of photosynthesis and photosynthetic discrimination,

during our measurement period in autumn 2015. We further compared the resulting relationship between R_n and $^{13}C_{Ass}$ to the observed (time lagged) relationship between R_n and the ^{13}C composition of ecosystem respiration $R^{13}_{eco}C$, derived from the measured Keeling plots cf. section 2.4.2.2. This analysis was performed to test the hypotheses of a link between δ values in assimilated material and respiration. We used the multilayer model CANVEG to calculate the isotopic composition of assimilated material $\delta^{13}C_{Ass}$. CANVEG is a biophysical one-dimensional multilayer canopy model, (see e.g. Baldocchi, 1997; Baldocchi et al., 2001). This multilayer model uses hourly meteorological inputs (among others, temperature, radiation, vapor pressure deficit[VPD], wind velocity and CO_2 mole fraction) as main drivers, as well as site-specific parameters (leaf area index, leaf clumping status, canopy height et. al.). Based on these input variables, CANVEG iteratively computes the biosphere-atmosphere exchange of water, carbon dioxide and energy as well as the microclimate within and above the canopy at hourly time steps. The carbon, water and energy modules have been validated for various environmental conditions and forest types (see e.g. Baldocchi et al., 2002; Baldocchi et al., 1999; Baldocchi et al., 1997). In particular, the model has also been applied to an unmanaged beech-dominated forest field site in approximately 30 km air-line distance to the measurement site of this study (Knohl et al., 2008a). The isotope-enabled version of this model additionally calculates $\delta^{13}C_{ij}$, the ^{13}C composition of CO_2 for each canopy layer i and each hourly time step j and the corresponding ^{13}C composition of assimilated material $\delta^{13}C_{Ass,ij}$ (Baldocchi et al., 2003). In our application, we set up the model to use 40 equally thick layers i and we used our meteorological measurements at the field site, described in Sect. 2.3.7, as input variables. We validated the model with eddy covariance measurements (Table 2.4) and used the model to calculate the isotopic composition of assimilated material $\delta^{13}C_{Ass,ij}$ for each of the 40 canopy layers i and for each hourly time step j. The ^{13}C composition of assimilated material $\delta^{13}C_{Ass}$ on daily timescale was calculated as an assimilation-weighted sum over all layers and time steps, with the modeled assimilation rate A_{ij} as a weighting factor:

$$\delta^{13}C_{Ass} = \frac{\sum_{i=1}^{40}\sum_{j=1}^{24} A_{ij} \cdot \delta^{13}C_{Ass,ij}}{\sum_{i=1}^{40}\sum_{j=1}^{24} A_{ij}} \tag{2.5}$$

We included only hours j and layers i during photosynthesis (with positive assimilation rates).

	SLOPE	R^2	NSEE
GPP	0.92	0.90	0.26
NEE	0.97	0.92	0.28
LE	1.03	0.78	0.16
H	0.96	0.87	0.37

Table 2.4: Validation of the multilayer model CANVEG using eddy covariance measurements of gross primary productivity (GPP), net ecosystem exchange (NEE), latent and sensible heat flux (LE and H). Slopes, R^2 values and normalized standard error estimates (NSEE) of linear regressions between modeled and measured values are comparable to the numbers given by Knohl et al. (2008a).

2.4 Results and discussion

2.4.1 Instrument characteristics

2.4.1.1 Precision

We use the Allan deviation σ_A at different averaging times τ (Table 2.5) to characterize the Delta Ray IRIS analyzer's precision. Starting at an averaging time of 1 s, that corresponds to the analyzer's maximum data acquisition frequency, the Allan deviation σ_A decreased with $\tau^{-1/2}$ (Fig. 2.3). This matches the expected behavior of a system that is dominated by white frequency noise. The measured Allan deviation σ_A followed this slope up to averaging times for approximately 300 s for δ value measurements and approximately 200 s for mole fraction measurements. At these timescales the analyzer showed its maximum precision of 0.02 ‰ VPDB for δ^{13}C, 0.03 ‰ VPDB-CO_2 for δ^{18}O and 0.007 ppm for CO_2 mole fraction. For averaging times above 200-300 s other error sources (such as instrument drift) became significant. For δ^{13}C, the precision of an earlier version of the instrument has also been measured by Geldern et al. (2014), reporting a minimum of σ_A at around 0.04 ‰ for an averaging time of $\tau \approx 550$ s. At this averaging time, we measured a comparable (slightly better) Allan deviation below 0.03 ‰ (cf. Table 2.5). Two other averaging times are particularly interesting for our application: Firstly, the averaging period of 20 s yields Allan variances below 0.1 ‰ for both δ values and 0.02 ppm for CO_2 mole fraction. Secondly, we set the IRIS analyzer's internal referencing procedure (described in Sect. 2.3.8) to 1800 s, which corresponds to an Allan variance of 0.03 ‰ for δ^{13}C and 0.08 ‰ for δ^{18}O values and 0.01 ppm for CO_2 mole fraction.

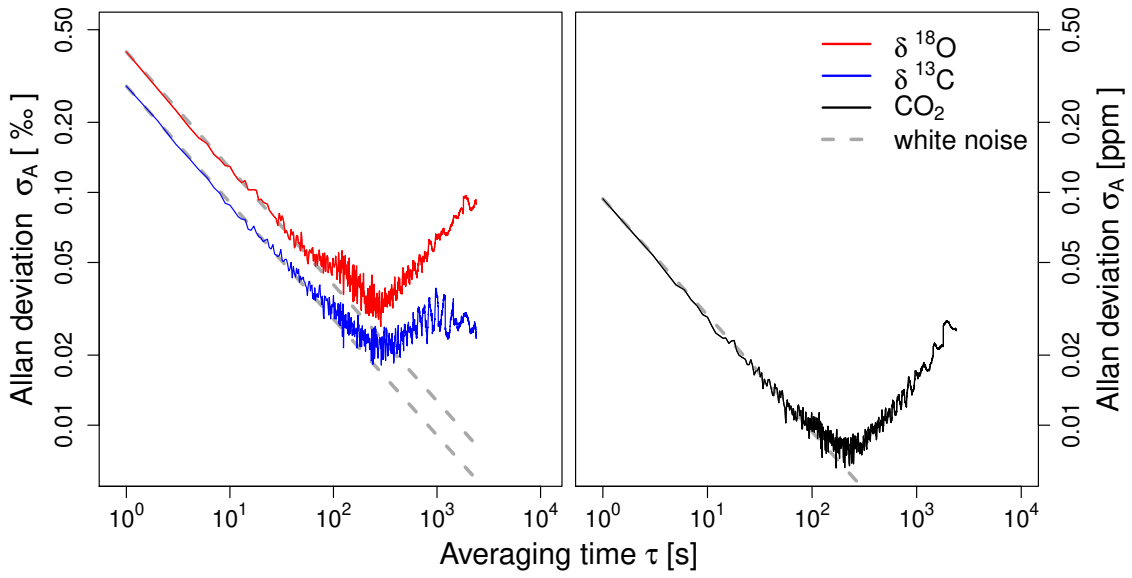

Figure 2.3: Allan deviation σ_A in ‰ VPDB for ^{13}C, in ‰ VPDB-CO_2 for ^{18}O and in ppm for CO_2 mole fraction; solid lines show the calculated Allan deviation and dashed lines show the typical white frequency noise error scaling.

τ [s]	$\delta^{13}C$ [‰]	$\delta^{18}O$ [‰]	c [ppm]
1	0.29	0.40	0.09
20	0.06	0.09	0.02
80	0.03	0.05	0.02
τ_{min}	0.02	0.03	0.007
500	0.03	0.04	0.01
1800	0.03	0.08	0.01

Table 2.5: Allan deviation σ_A for different averaging times τ, with the minimum Allan deviation for $\tau_{min} \approx 290\,s$ for both δ values and 170 s for CO_2 mole fraction c

2.4.1.2 Evaluation of the calibration strategy

The instrument's internal calibration strategy (described in section 2.3.8) is based on the following:

- A nonlinear relationship between raw δ values and mole fractions (Fig. 2.4).
- A linear relationship between the calibrated δ value (measured with IRMS) and the mole fraction-corrected δ value - $\delta_{c-\text{corrected}}$ in Eq. 2.4 (Fig. 2.5, middle and right panel).
- A linear relationship between measured (raw) and real mole fractions (Fig. 2.5, left panel).
- The repeatability of the calibration curves – for δ values modulo the offset correction that is applied by the instrument's internal 'referencing' (Fig.2.6 and Table 2.6).

Raw δ values show a nonlinear dependency from raw mole fractions (Fig. 2.4). This nonlinear relationship deviates from the mole fraction-dependency correction applied by the instrument, $\delta_{c-\text{corrected}}(c_{\text{raw}})$ in Eq. 2.4, as shown in Fig. 2.4. Here, the instrument internal mole fraction-dependency correction is shown for the used gas tank 'ambient' after an offset correction at a mole fraction of 400 ppm, which is similar to the instrument's internal 'referencing'. Thus, the mean deviations of the measured δ values from the mole fraction-dependency correction (top panel of Fig.2.4) give an estimate of the uncertainty of measurements that is related to the deviation from the reference mole fraction. For referencing at 400 ppm, these deviations were approximately below 0.2 ‰ for ^{13}C and 0.4 ‰ for ^{18}O.

The measured linear relationships for mole fraction and δ scale calibration (Fig. 2.5) have R^2 values of above 0.9999 for mole fractions, above 0.999 for $\delta\ ^{13}C$ and above 0.998 for $\delta\ ^{18}O$. The linearity and potential accuracy, as defined by Tuzson et al. (2008), can be quantified as the $1\,\sigma$ standard deviation from the linear fits. The so defined potential accuracy of the instrument internal linear calibrations is 0.45 ppm for CO_2 mole fraction, 0.24 ‰ for $\delta^{13}C$ and 0.3 ‰ for $\delta^{18}O$. For both δ values, this is comparable to the uncertainty related to the nonlinear mole fraction calibration that varies with δ and C_{CO2} as discussed above.

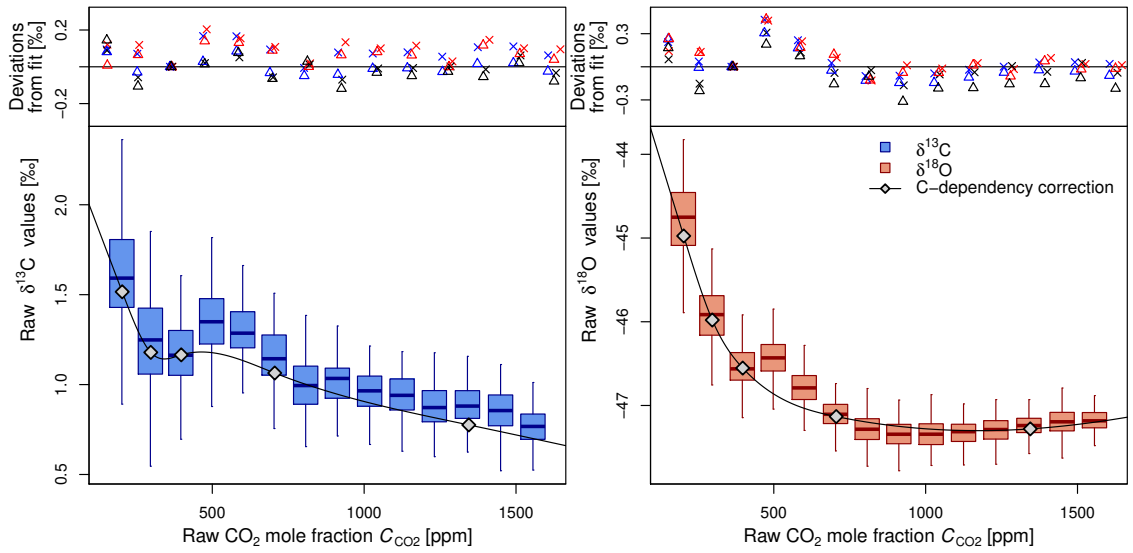

Figure 2.4: Box-and-whisker plot showing the nonlinear mole fraction dependency (*c*-dependency) of raw δ values for ^{13}C and ^{18}O respectively, here as an example for the CO_2 tank 'ambient'. The measured *c*-dependency is compared to the respective *c*-dependency correction (black line, with grey symbols marking the data points used during the corresponding calibration measurement). The *c*-dependency correction is offset corrected to match the raw δ values at 400 ppm, and the mean deviation from the offset-corrected fit is shown in the top panel for two measurements (different symbols) with three different gas tanks ('ambient' in blue, 'bio' in black and 'bio2' in red).

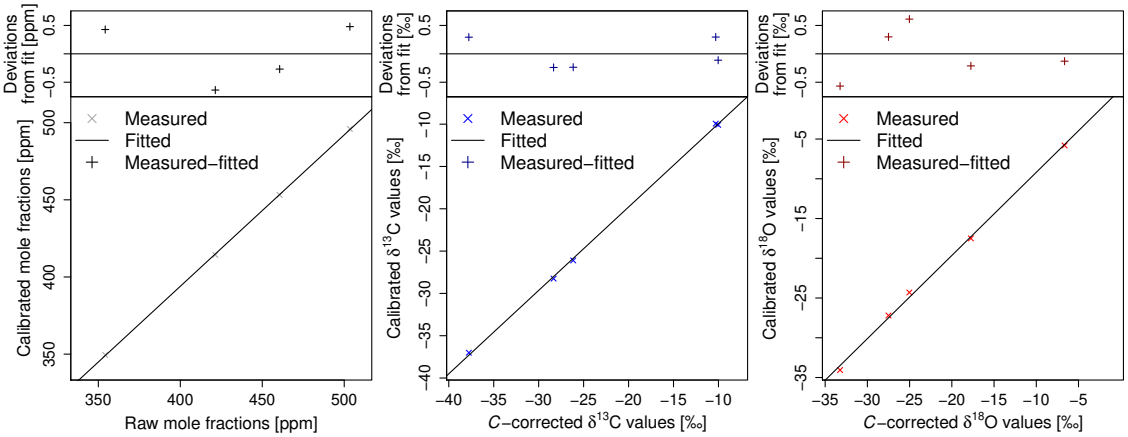

Figure 2.5: Linear calibrations for mole fraction (left panel) and mole fraction-corrected δ^{13}C and δ^{18}O (middle and right panel) respectively.

Table 2.6: Standard deviations σ of the measured (calibrated) δ values over a large mole fraction range based on 6-hourly lab measurements over a period of 9 days.

mole fraction	$\sigma(\delta_{\text{meas}} - \delta_{\text{tank}})$			
ppm	‰			
	tank: ambient		tank: bio	
	^{13}C	^{18}O	^{13}C	^{18}O
202	0.07	0.14	0.09	0.13
396	0.04	0.05	0.08	0.08
600	0.09	0.08	0.12	0.12
807	0.08	0.08	0.11	0.11
1018	0.10	0.08	0.13	0.11
1232	0.12	0.09	0.13	0.11
1450	0.14	0.11	0.15	0.12
1664	0.14	0.11	0.14	0.12
3145	0.17	0.15	0.17	0.15

The repeatability of the calibration curves is discussed here based on measurements of the nonlinear mole fraction dependency (Fig. 2.4) and repeated measurements of gas tanks with two different C_{CO2} and δ values to evaluate temporal changes in the respective linear relationships (Fig. 2.5). These measurements were taken every six hours for a period of nine days. For these repeated measurements the standard deviation of the calibrated values was below 0.2 ppm for mole fractions and (if delta values were measured at 400 ppm and referenced at 380 ppm) below 0.05 and 0.1 ‰ for ^{13}C and ^{18}O respectively. Thus, the uncertainty related to the repeatability of the linear calibrations is smaller than the potential accuracy discussed above. For δ values, these values are comparable to the repeatability measured with other laser spectrometers, as reported by several authors, (e.g. Sturm et al., 2012; Sturm et al., 2013; Vogel et al., 2013). For mole fractions on the other hand, Sturm et al. (2013) reported a much smaller value of 0.03 ppm, based on more frequent calibration. In our setup, the mole fraction calibration is only performed once after the instrument is restarted; thus there might be a potential for better repeatability in mole fraction measurements with more frequent mole fraction calibration. For δ values measured at mole fractions that deviate further from the reference mole fraction (here 380 ppm), the repeatability also depends on mole fraction (Table 2.6). Repeated measurements of these deviations have standard deviations below 0.15 ‰ for both δ values for mole fractions between 200 and 1600 ppm.

For mole fraction measurements, the uncertainty related to the linear calibration dominates the overall uncertainty, whereas the uncertainty of δ value measurements depends on the setup, in particular on the 'referencing'. If measurements were carried out at the mole fraction used during 'referencing', the accuracy would be limited by the linear calibrations and the corresponding repeatability (c.f Table 2.7). If measurements were carried out

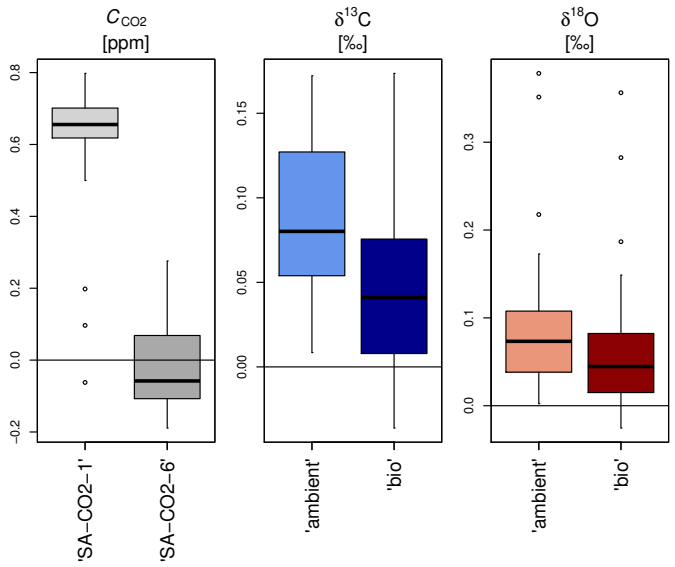

Figure 2.6: Box-and-whisker plots for the deviations of calibrated mole fractions and δ values from laboratory measurements (at MPI in Jena) for repeated measurements of different calibration tanks (cf. Table 2.3 for C_{CO2} and δ values of the gas tanks) over a period of 9 days (N=36). Delta values were measured at 400 ppm and 'referencing' was done approximately every 30 minutes at 380 ppm to simulate conditions during a measurement campaign.

at mole fractions that deviate from the 'referencing' mole fraction, the accuracy would be limited by the actual mole fraction dependency that deviates from the instrument internal correction of mole fraction dependency (cf. Fig. 2.4 and Table 2.7). In this case, the accuracy could be further improved by applying a correction of the mole fraction dependency based on more points.

Table 2.7: Uncertainties related to the different calibration steps and their repeatability defined as 1σ standard deviation of the respective calibration step.

Calibration	$\delta^{13}C$ [‰]	$\delta^{18}O$ [‰]	c [ppm]
Linear calibrations	0.24	0.3	0.45
Corresponding repeatability	0.05	0.1	0.2
Correction of c-dependency	0.2	0.4	-
Corresponding repeatability	0.15	0.15	-

2.4.1.3 Repeatability during the field campaign

We analyzed the repeatability of the Delta Ray analyzer under field conditions by evaluating half-hourly measurements of the same gas tank (SA-CO_2-5) during the whole measurement period. We use the standard deviations of measured mole fractions and delta values to quantify the repeatability of our setup in the field including our calibration strategy. The standard deviations of these long-term measurements were below 0.3 ppm for CO_2 mole fraction, below 0.2 ‰ for $\delta^{13}C$ and below 0.25 ‰ for $\delta^{18}O$ (frequency distributions and time series of the long term measurements are shown with color-coded metadata in Fig.

2.7.[1] For mole fractions, the measured repeatability of approximately 0.3 ppm is slightly larger than the repeatability of the mole fraction calibration discussed above, but still below the potential accuracy discussed in section 2.4.1.2. In the case of δ values, the obtained repeatability of approximately 0.2 ‰ for ^{13}C and 0.25 ‰ for ^{18}O is larger than the repeatability of the linear calibration parameters obtained during lab measurements (0.05 ‰ for ^{13}C and 0.1 ‰ for ^{18}O). The measured repeatability during the field campaign also exceeds the repeatability of the measurements of the mole fraction dependency (below 0.15 ‰ for both δ values over a large mole fraction range; cf. section 2.4.1.2). This could be related to the fact, that the δ values of our target standard were out of the calibration range, leading to an enhancement of fluctuations in the calibration parameters.

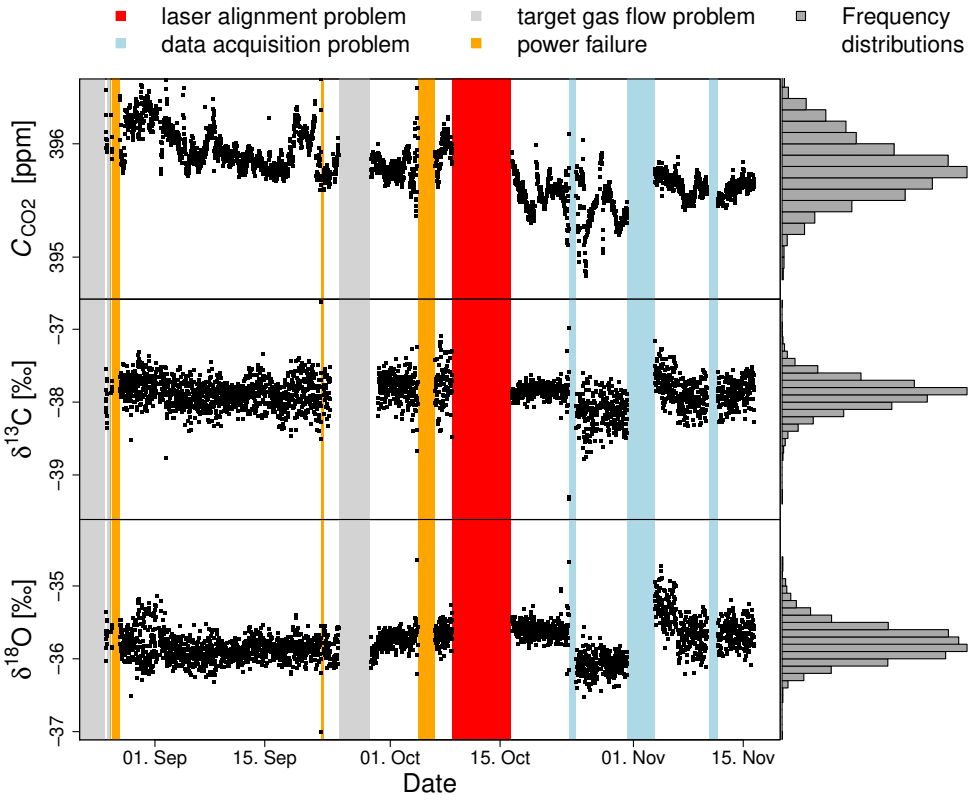

Figure 2.7: Time series and frequency distributions of half-hourly measurements of the mole fraction (top panel) and δ values (middle and bottom panel) for target gas 'SA-CO_2-5' (cf. Table 2.3) for the whole measurement period excluding periods that show problems with target gas flow, calibration and laser alignment. The major reasons for data gaps are marked with different colors.

1 In the case of ^{13}C , we excluded the target measurements between 23^{rd} of September and 29^{th} of September, because we obtained a problem with the ^{13}C calibration that led to a large jump in the δ ^{13}C value of the (very depleted) target standard. This jump did not occur in the height measurements, probably because they were much closer to the reference δ value.

2.4.1.4 Response time

We measured the response time of our system (tubing and measurement cell of the Delta Ray analyzer) by using the valve system shown in Fig. 2.2 to switch from ambient air with δ^{13}C≈-9 ‰ and δ^{18}O≈1 ‰ to tank air with δ^{13}C≈-38 ‰ and δ^{18}O≈-36 ‰. The time series of the measured δ values after the change of the valve position (Fig. 2.8) consisted of three different phases that can be related to different physical processes: For the first phase, the measured δ values remained constant for τ_1 ≈14 s. This is the setup-specific time it took for the gas to flush the tubes and valves before entering the cell. For the second phase, we observed a quadratic decay of the measured δ values, which we relate to mixing of gas within the tubes (before it enters the cell). This phase dominated the temporal response of our system for τ_2 ≈4.5 s. The third phase of temporal response is the exponential decay with a characteristic decay time (defined here using the 10 % threshold) $\tau_{10\%} \approx 10$ s for δ^{13}C and $\tau_{10\%} \approx 11$ s for δ^{18}O. This exponential behavior can be derived for an idealized situation that includes perfect mixing in a volume V_{mix} yielding

$$\tau_{10\%} = \frac{log(10) \cdot p_{\mathrm{cell}} \cdot V_{\mathrm{mix}}}{\Phi}$$

with flow rate Φ, cell pressure p_{cell} and effective mixing volume V_{mix}. Using the volume of the measurement cell as an upper threshold for the effective mixing volume within the cell, $\max(V_{\mathrm{mix}}) = V_{\mathrm{cell}} = 80$ ml, we can calculate an upper threshold for $\tau_{10\%}$. With the

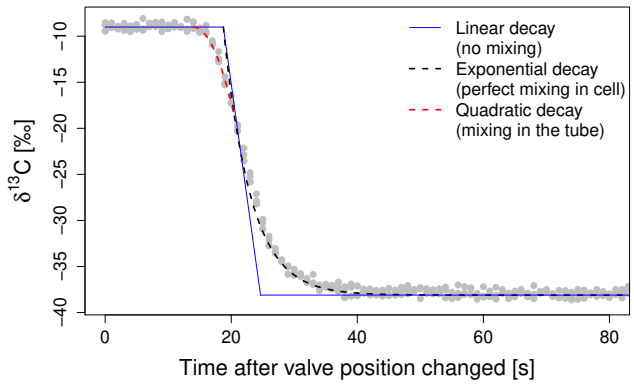

Figure 2.8: The response time of our experimental setup can be divided into three phases with different dominant mechanisms: Directly after switching it took approximately 14 s to flush the tubing, the adjacent 4 s were dominated by the mixing processes in the tubes before the gas entered the measuring cell (quadratic fit) and finally we observed a response behavior that is dominated by mixing processes within the measuring cell (exponential fit) with a characteristic decay time of $\tau_{10\%} = 10$ s for δ^{13}C. These response times were similar for δ^{18}O (not shown). The linear fit shown here describes a first order approximation of the theoretical cell response for the (unrealistic) assumption that there is no mixing in the measurement cell. From this assumption, it can be derived that the δ values would show a dominantly linear decay with the slope $m = (\delta_{\mathrm{new}} - \delta_{\mathrm{old}})/\tau_{\mathrm{theoretical}}$ and the theoretical instrument cell response time $\tau_{\mathrm{theoretical}} = p * V/\Phi$, with pressure p, Volume $V$and flow rate Φ. In our case $\delta_{\mathrm{new}} - \delta_{\mathrm{old}}$= -29 ‰ and thus $\tau_{\mathrm{theoretical}}$= 5.9 s.

instruments flow rate of $\Phi = 0.08\,\mathrm{slpm}$ and the cell pressure of $p_{\mathrm{cell}} \approx 100\,\mathrm{mbar}$, we get $\tau_{10\%,\mathrm{max}} \approx 13.6\,\mathrm{s}$. Thus, the measured value of $\tau_{10\%}$ is slightly below this value, indicating $V_{\mathrm{mix}} < V_{\mathrm{cell}}$. We define the total response time τ_{tot} as the time span it took until the step change between the two inlets reached 0.1 % of the corresponding difference in δ values, with $\tau_3 = \tau_{0.1\%} = 3 \cdot \tau_{10\%}$. The three different phases of instrument response (tube transport τ_1, tube-mixing-dominated change τ_2 and cell-mixing-dominated change τ_3) summed up to a net response time $\tau_{\mathrm{tot}} = \tau_1 + \tau_2 + \tau_3 < 60\,\mathrm{s}$. Thus, the cell flushing time of our application (60 s) is appropriate to produce independent measurements of two different inlets.

2.4.1.5 Utilization rate, power consumption and maintenance effort

We define the utilization rate as the number of successfully recorded measurement cycles divided by the number of measurement cycles that were theoretically possible during the field campaign (approximately 4200). This can be calculated separately for a) profile measurements and b) target gas measurements, because some data gaps were specific for target measurements. The utilization rate was approximately 80 % for measurements of the height profile and approximately 70 % for target gas measurements. Two major reasons for data gaps reduced the utilization rate for both, profile and target measurement by 8.6 % (a laser alignment problem that was resolved after 7 days) and 6 % (three data acquisition problems, the longest lasting 3 days). Additionally, four external power supply problems at the field site lead to a further reduction of the utilization rate by 3.3 %. These data gaps, as well as smaller data gaps, that reduced the utilization rate are listed in Table 2.8. In the case of target measurements, the main reason for data gaps (accounting for a reduction of the utilization rate of more than 9 %) was plumbing issues that led to a contamination of the target gas by ambient air. Thus, a more stable target plumbing would be a promising approach to increase the utilization rate, as well as a more stable power supply and more frequent field trips.

Table 2.8: Percentage of total measurement time for major data gaps. The latter two data gaps concerned only target gas measurements.

Reason for data gap	Percentage
Data acquisition problems	6.0 %
Laser alignment problem	8.6 %
Calibration	1.5 %
Power failures	3.3 %
Additional measurements	1.6 %
Plumbing issues (only target)	9.5 %
Switching unit failure (only target)	0.7 %

Maintenance effort and power consumption of the whole setup were moderate: The analyzer's power consumption of approximately 220 W was slightly smaller than the power consumption of the basic infrastructure of the setup that included the pump to purge the nine inlet tubes and the heated valve box (330 W). To maintain and to control the setup, we went to the field site weekly or every two weeks and used remote access to the instrument via a satellite connection.

2.4.2 Ecological application

2.4.2.1 Time series of measured quantities

The measured CO_2 mole fractions at 45 m height at our field site in a managed beech forest in central Germany ranged from 385 to 450 ppm, with corresponding δ values between -11 and -7 ‰ for ^{13}C and between -6 and 2 ‰ for ^{18}O over a 3-month period in autumn 2015 (Fig. 2.9). As the lower heights commonly contain larger amounts of respired CO_2 with a typically lighter carbon and oxygen composition, the lower inlets show larger CO_2 mole fractions C_{CO2} with smaller δ values. We calculated a 3-month time series of nighttime Keeling plot intercepts $\delta^{13}C_{KP}$ and $\delta^{18}O_{KP}$ that can be interpreted as the respective isotopic composition of nighttime net ecosystem CO_2 exchange (respiration) $R^{13}_{eco}C$ and $R^{18}_{eco}O$ (shown with temperature and precipitation data in Fig. 2.10). A particular feature of the measurement period is an early snow and frost event with negative temperatures during four nights between 11. and 15. October 2015 (Fig. 2.10). The corresponding snow event on 13^{th} of October was visible on a canopy picture, taken at midday on 13. October 2015. The time of the snow and frost event coincided with changes in the characteristics of $\delta^{18}O$, $R^{18}_{eco}O$ and $R^{13}_{eco}C$: For $\delta^{18}O$ and $R^{18}_{eco}O$ a strong decrease was obtained after the snow event. This decrease was the largest signal in the respective time series. For $R^{13}_{eco}C$, the analysis of its potential meteorological drivers yielded different results for the time periods before and after the first snow. Additionally, according to eddy covariance measurements, the forest was a net CO_2 sink with negative diurnal net ecosystem exchange (NEE) before 12 October (with only one exception), whereas it was a net CO_2 source with positive diurnal NEE after the snow event on 13. October (also with only one exception).

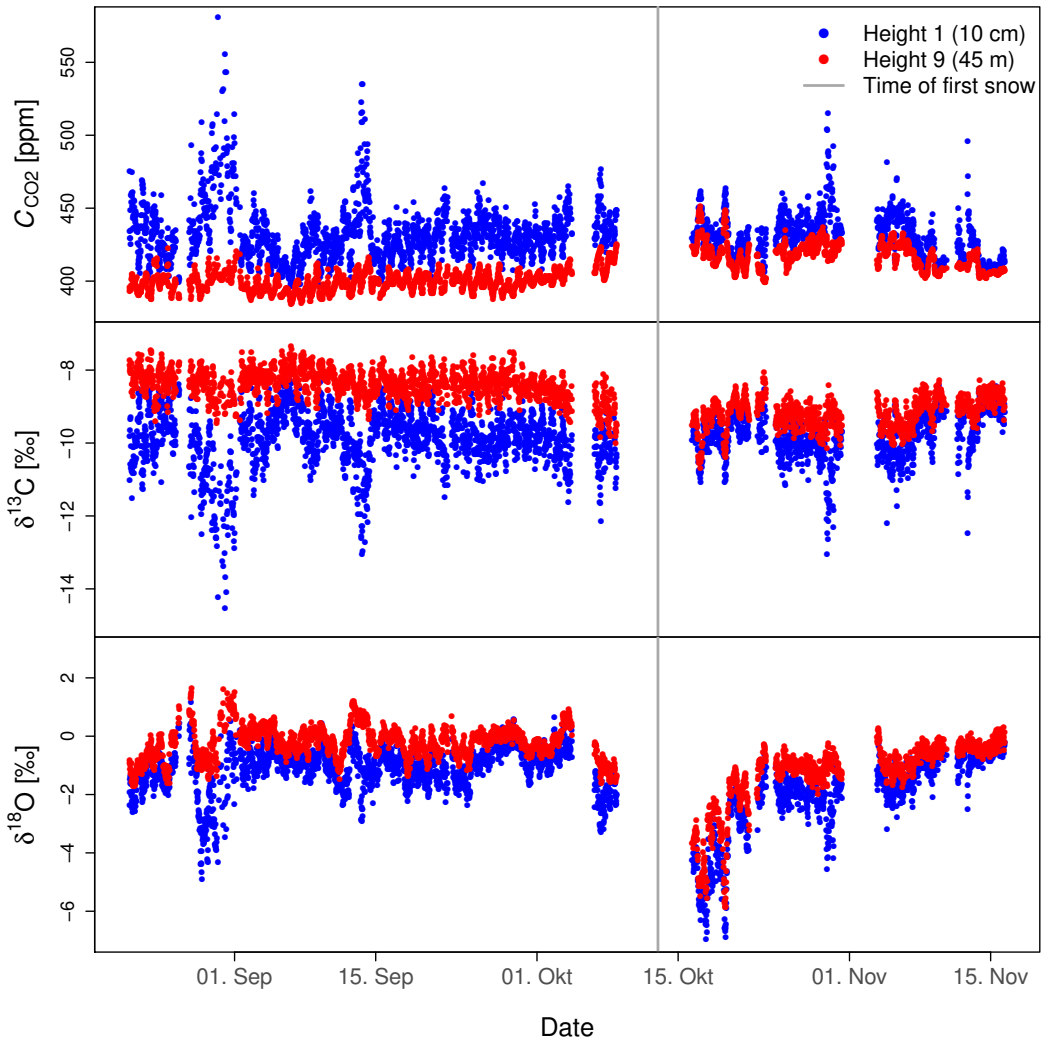

Figure 2.9: Time series of all measured mole fractions C_{CO2} and both δ values at the lowest (blue points) and highest (red points) inlet at 0.1 and 45 m height respectively.

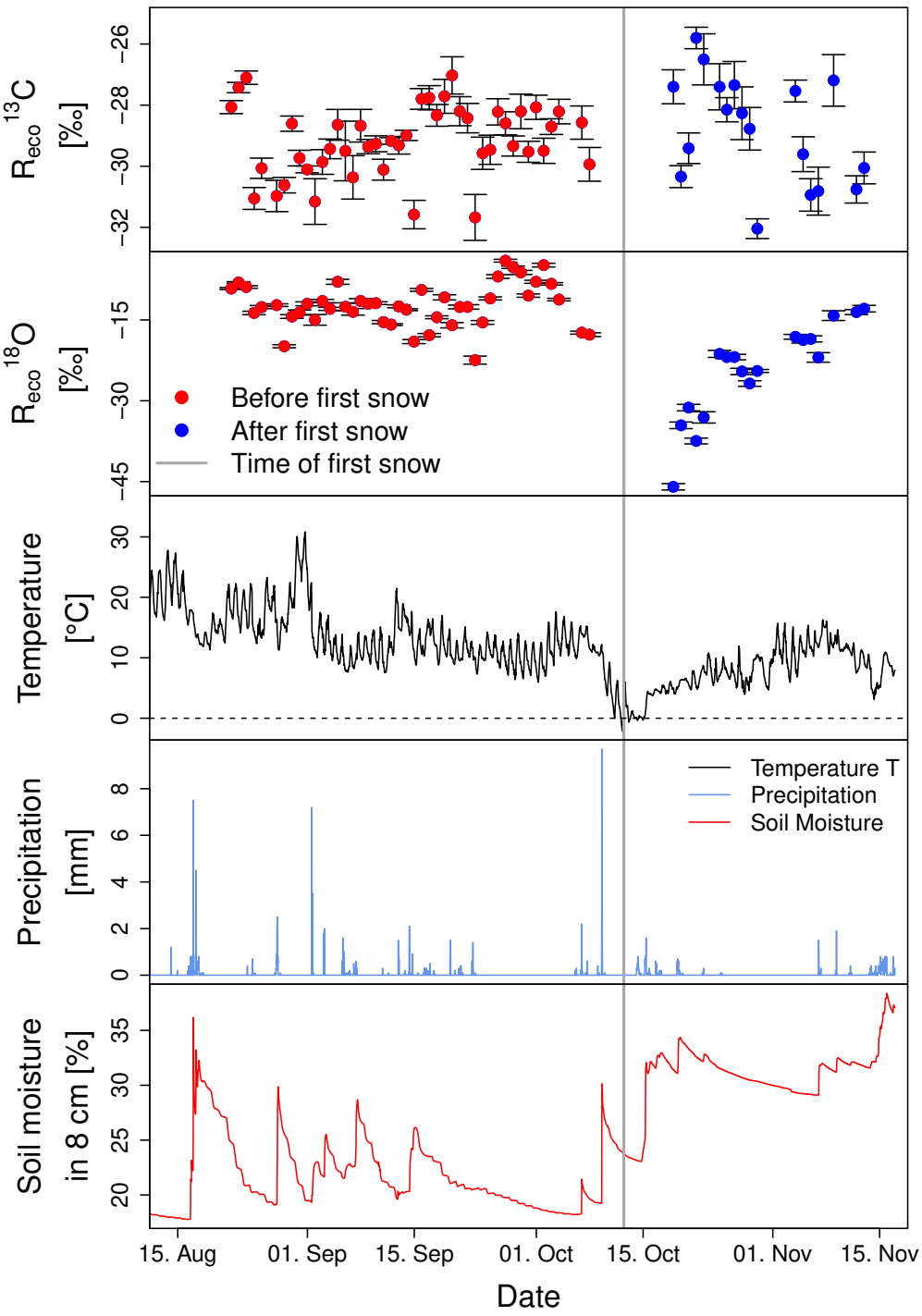

Figure 2.10: Time series of the measured isotopic composition of nighttime CO_2 exchange (respiration) $R^{13}_{eco}C$ and $R^{18}_{eco}O$ based on Keeling plot intercepts in combination with temperature, precipitation and soil moisture in 8 cm depth. Error bars denote the standard error of the Keeling plot intercept (based on the linear regression of δ vs. $1/c$). A particular feature of this time series is a first snow and frost event on 13. October 2015, marked in gray.

2.4.2.2 Potential drivers for $R^{13}_{eco}C$

Previous studies linked the temporal variability of the ^{13}C composition of ecosystem respiration $R^{13}_{eco}C$ partially to changes in the meteorological conditions during photosynthesis, namely relative humidity (RH), vapor pressure deficit (VPD), photosynthetically active radiation (PAR) and the ratio VPD/PAR (Bowling et al., 2002; Ekblad et al., 2001; Knohl et al., 2005b). These links occurred with time lags that correspond to the time lag between assimilation and respiration, which is approximately 4 to 5 days for mature trees (Kuzyakov et al., 2010). The observed time-lagged links between meteorological variables and $R^{13}_{eco}C$ were interpreted by the respective authors as an indication for a link between the isotopic composition of respiration $R^{13}_{eco}C$ and the isotopic composition of recent assimilates $\delta^{13}C_{Ass}$, which is controlled by photosynthetic discrimination of the heavier ^{13}C according to the Farquhar model (Farquhar et al., 1989). Thus, in accordance with previous studies, we hypothesize the following:

Hypothesis A: The variability of $R^{13}_{eco}C$ can be partly explained by the isotopic composition of recent assimilates $\delta^{13}C_{Ass}$, which is controlled by meteorological drivers during photosynthesis according to the Farquhar model. Thus, the variability of $R^{13}_{eco}C$ is linked to the variability of meteorological drivers of photosynthesis and photosynthetic discrimination with a time lag that is consistent with the time lag between respiration and assimilation.

To test this hypothesis, we calculated the Pearson correlation coefficient r_{pear} between $R^{13}_{eco}C$ and the n-day sum (with n from 1 to 6) of the meteorological quantities that we expect to control ^{13}C discrimination for different time shifts τ. For the time period before the first snow (when the ecosystem was a CO_2 sink), the strongest correlation we found was a moderate negative correlation between $R^{13}_{eco}C$ and the 2-day sum of net radiation R_n with a time shift τ of 2 days (Fig. 2.11). This correlation is significant with a Pearson correlation coefficient r_{pear} of approximately -0.56, which is clearly beyond the

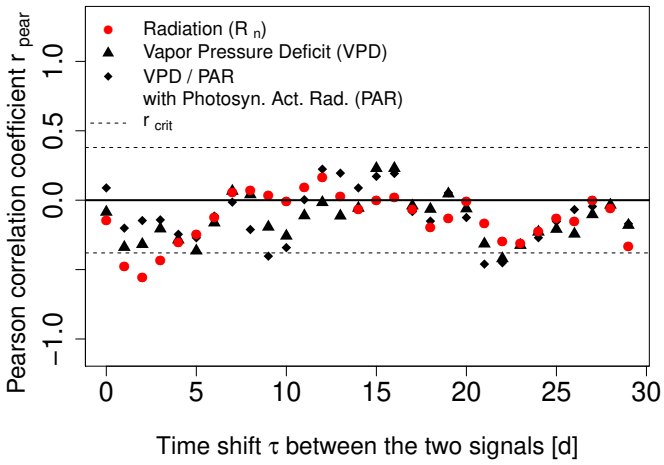

Figure 2.11: Pearson correlation coefficient of the isotopic composition of ecosystem respiration $R^{13}_{eco}C$ and the 2-day sum of different meteorological variables (shifted by different times τ) before the first snow event in autumn 2015.

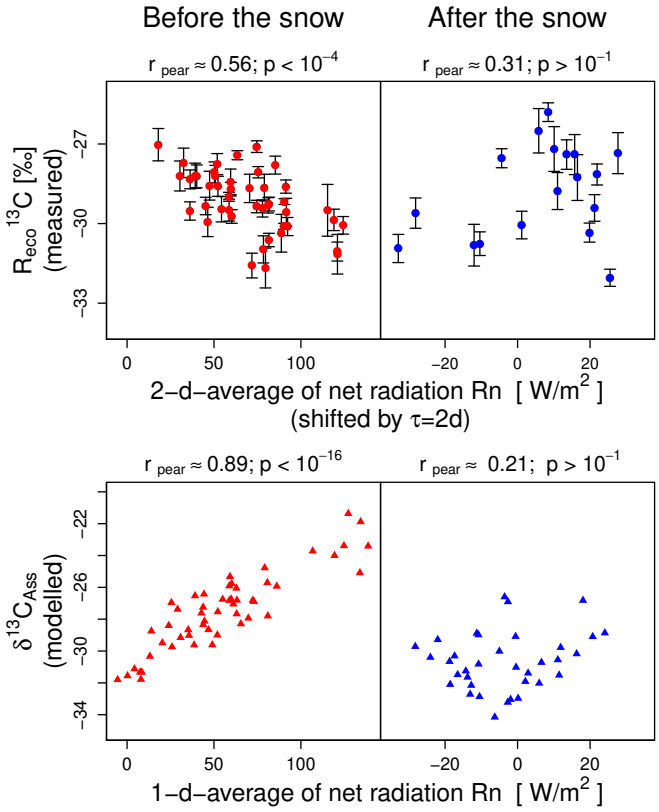

Figure 2.12: Observed relationships between net radiation R_n, the measured isotopic composition of ecosystem respiration $R^{13}_{\text{eco}}\text{C}$ (top panels) and the modeled ^{13}C composition of assimilated material $\delta^{13}\text{C}_{\text{Ass}}$ (bottom panels). Significant correlations were observed before the first snow (left) but became insignificant after the snow (right). r_{pear} and p values are derived from the respective linear regressions.

corresponding critical value of approximately $\pm$ 0.38 for N=45 and $\alpha = 0.005$. The time lag of this correlation is in accordance with the expected time lag between assimilation and respiration of 2 to 5 days for mature trees (Kuzyakov et al., 2010). However, the correlation itself cannot be directly explained by the Farquhar model of discrimination as radiation influences both, the CO_2 supply (by influencing stomatal conductance) and the CO_2 demand (by influencing assimilation) in the leaf (Farquhar et al., 1982). In particular we did not find a significant time-lagged positive correlation between $R^{13}_{\text{eco}}\text{C}$ and VPD, RH or the ratio VPD/PAR (Fig. 2.11), which could be directly associated with the Farquhar model and has been found by the above-mentioned studies. To test if it might still be reasonable to interpret the observed negative correlation of $R^{13}_{\text{eco}}\text{C}$ with R_n as a time-lagged link between $R^{13}_{\text{eco}}\text{C}$ and the isotopic composition of recently assimilated material $\delta^{13}\text{C}_{\text{Ass}}$ on an ecosystem scale, we performed a more complex calculation of $\delta^{13}\text{C}_{\text{Ass}}$ by using the multilayer model CANVEG (cf. Sect. 2.3.9). The advantage of CANVEG is that it accounts for the nonlinear interactions between air temperature, air humidity, radiation, stomatal conductance and photosynthesis. Before the first snow event

during our measurement period, the modeled $\delta^{13}C_{Ass}$ correlated significantly with the diurnal sum of net radiation R_n with an r_{pear} of 0.89 (Fig. 2.12) - corresponding r_{crit} ≈0.33 for N=63. However, in contrast to the time-lagged correlation, which we found in our Keeling plot data, this correlation is positive (Fig. 2.12). As the multilayer model does not support the interpretation of the observed negative correlation between R_n and $R^{13}_{eco}C$ through the variability of the isotopic composition of recent assimilates $\delta^{13}C_{Ass}$, it does not support hypothesis A.

An alternative interpretation of the observed correlation between the isotopic composition of respiration $R^{13}_{eco}C$ and net radiation R_n would be a link between $R^{13}_{eco}C$ and the amount of recent assimilates (alternatively to the isotopic composition of recent assimilates). Because soil respiration has been measured to account for around 80% of ecosystem respiration in an old beech forest at less than a 30 km distance to our field site (Knohl et al., 2008b), we assume that soil respiration dominates ecosystem respiration and thus we further focus on soil respiration and discuss the following hypothesis:

Hypothesis B: The observed time-lagged correlation between $R^{13}_{eco}C$ and net radiation R_n is related to the temporal variability of the ratio of autotrophic to total soil respiration[1].

A link between photosynthesis and autotrophic soil respiration has been shown in many studies throughout different ecosystems, including a beech-dominated forest at less than a 30 km air-line distance to our field site in a managed beech forest (Moyano et al., 2008). In this study, the authors found that 73 % of the variability in rhizosphere respiration (the major part of autotrophic soil respiration) correlated with photosynthesis (GPP) and the ratio between autotrophic and total soil respiration was approximately 50 %. Additionally, evidences for a large temporal variability on diurnal and seasonal scales of the contribution of autotrophic to total soil respiration have been reported for a temperate hardwood forest (Savage et al., 2013) and for a mature temperate boreal forest (Carbone et al., 2016). In our field experiment, the observed correlation between $R^{13}_{eco}C$ and R_n with an r_{pear} of 0.56 (and thus $r^2_{pear} = 0.3$) links 30 % of the variability of $R^{13}_{eco}C$ to R_n with a time lag of 2-4 days. As the measured isotopic composition of ecosystem respiration $R^{13}_{eco}C$ spanned a range of 6 ‰, this corresponds to a range of 1.8 %. Hypothesis B would further imply that this variability over a range of 1.8 ‰ corresponds to that proportion of the variability of autotrophic respiration that is linked to photosynthesis. If we were to estimate this proportion to represent 73 % of the total variability of autotrophic respiration (following Moyano et al., 2008), the corresponding total variability of autotrophic respiration would correspond to a range of approximately 2.5 ‰ . If in autumn the ratio of autotrophic to total respiration would approximate 0 %, this value of 2.5 ‰ would be equal to the difference $\Delta_{tot-aut} = \delta_{tot} - \delta_{aut}$ between the isotopic composition of total respiration δ_{tot} and the isotopic composition of autotrophic respiration δ_{aut}. In general, a value of $\Delta_{tot-aut} = +2.5$ ‰ is within the range of differences, that have been reviewed to be on average about +4 ‰ (Bowling et al., 2008) for different ecosystems. A positive value of

1 The term 'autotrophic' is not consistently defined among different authors. Here we use this term equivalent to 'root-derived respiration', including respiration from the living root tissue, from microorganisms in the rhizosphere and mycorrhizal symbiotic fungi (cf. Moyano et al., 2009).

$\Delta_{\mathrm{tot-aut}}$ with a lighter δ^{13}C composition of autotrophic respiration would be consistent with hypothesis B. As a note of caution, however, none of the studies that analyze autotrophic soil respiration in the above-mentioned review, were performed in a forest ecosystem. For C3 woody species, including forests, more enriched δ^{13}C values of autotrophic soil respiration, and thus negative values for $\Delta_{\mathrm{tot-aut}}$, have been reported (Ghashghaie et al., 2014). In a beech forest in southern Germany, the sign of some involved fractionation effects varied temporally (Paya et al., 2016). Thus, the comparison with literature data about the temporal variability of the ratio between autotrophic and total soil respiration and the respective isotopic compositions gives the possibility that hypothesis B is true, but we cannot, however, prove it without additional independent measurements. To test this hypothesis, we would need to measure the amount and the isotopic composition of autotrophic respiration, total soil respiration and ecosystem respiration (e.g. by a trenching experiment) at our field site with an appropriate time resolution to capture the day-to-day variability during the field campaign. Lab measurements using incubations could also give an idea of the isotopic composition of autotrophic and total soil respiration, but would not fully reflect field site conditions.

2.4.2.3 Characteristics of R^{18}_{eco}O and δ^{18}O

The seasonal variability of δ^{18}O and R^{18}_{eco}O (shown in Fig. 2.9 and Fig. 2.10) is influenced by oxygen exchange when CO_2 gets dissolved in different water pools (e.g. leaf and soil water) with variable isotopic compositions. These isotopic compositions in turn are controlled by multiple physical and biological factors such as temperature, precipitation, vapor pressure deficit (VPD) or the activity of the enzyme carbonic anhydrase that accelerates the oxygen exchange between water and CO_2 (Bowling et al., 2003b; Farquhar et al., 1993; Gillon et al., 2000; Miller et al., 1999; Wingate et al., 2009). The strongest feature of the measured time series of R^{18}_{eco}O is an approximately 30 ‰ large decrease within 10 days from approximately -18 ‰ on 7. October to approximately -46 ‰ on 18. October (Fig. 2.10). During the same time period, the δ^{18}O value of nighttime ambient CO_2 at 45 m height decreased from approximately -1 ‰ down to -3.5 ‰ at nighttime and down to -6 ‰ during daytime (Fig. 2.9). As for R^{18}_{eco}O, this decrease is the strongest signal in the measured time series of δ^{18}O. The time of these decreases in R^{18}_{eco}O and δ^{18}O coincided with the time of the first snow and frost event in autumn 2015. This indicates that the snow event has a noticeable effect on both δ^{18}O and R^{18}_{eco}O, but as the change in (nighttime) R^{18}_{eco}O is more than 10 times larger than the corresponding change in δ^{18}O of nighttime CO_2, this effect is particularly enhanced for R^{18}_{eco}O. For comparison, similar strong peaks in R^{18}_{eco}O have been observed in a semiarid woodland after precipitation in New Mexico (Shim et al., 2013), but this study refers to a monsoon-dominated ecosystem with comparably large variability in the ^{18}O and does not focus on the difference of these pulses of snow and rain events.

Possible explanations for the observed large decreases in both δ^{18}O and R^{18}_{eco}O after the snow would involve the ^{18}O exchange of CO_2 with water pools that are fed by the recent snow event and the response to changes in many of the above-mentioned physical and biological factors that influence the oxygen exchange between CO_2 and water. One of the factors that can cause a depletion in ^{18}O due to the exchange of oxygen between CO_2 and snow-fed water pools is the fact that snow has in general a lighter ^{18}O composition

than rain. The isotopic composition of rain can often be related to Rayleigh fractionation processes (Gat, 1996) and is thus related to isotopic exchange between the raindrops and air masses in clouds when rain is falling (Gat, 1996, citing Bolin, 1959 and Friedman et al., 1962). As a result of the continuous isotopic exchange with air masses in the cloud, raindrops do not carry the very depleted isotopic composition within the cloud whereas for snow, the isotopic exchange between the falling snowflakes and the air masses in the cloud does not take place, resulting in a more depleted precipitation (Gat, 1996). For example, Orlowski et al. (2016) reported a maximal difference of approximately 15.5 ‰ between the $\delta^{18}O$ values of rain and snow over a 2-year measurement period at a field site at an approximately 160 km air-line distance from our field site. A smaller maximal difference of approximately 9 ‰ between the $\delta^{18}O$ of snow and the corresponding monthly means for rain was reported by Wenninger et al. (2011), based on 2 years of measurements at two catchments in the German black forest at a 414 km air-line distance from our field site. Thus, the ^{18}O-depleted isotopic composition of snow compared to rain may explain some of the observed 30 ‰ decrease in $R^{18}_{eco}O$. One possible additional effect could be the fact that soil-respired CO_2 is typically in equilibrium not with rain but with soil water in the top soil layers (0 to 20 cm) (Miller et al., 1999; Wingate et al., 2009). Evaporative effects can shift the isotopic composition in the upper soil layers towards more ^{18}O-enriched values (Miller et al., 1999; Wingate et al., 2009) potentially increasing the $\delta^{18}O$ difference before and after the snow event.

We tested the correlation between $R^{18}_{eco}O$ and different meteorological variables that potentially control the isotopic composition of different water pools within the ecosystem over the whole measurement period as well as the sub-periods before and after the first snow (Table 2.9). As the underlying multiple interaction processes between oxygen in CO_2 and different water pools , as well as the respective isotopic compositions of these pools are complex, this analysis was not performed to causally link the measured $R^{18}_{eco}O$ to a single meteorological driver but rather to look for changes of these correlations that could be interpreted as changes in the processes that drive $R^{18}_{eco}O$ before and after the snow event. For the whole measurement period, the strongest of the analyzed correlations was a correlation between $R^{18}_{eco}O$ and soil moisture at a depth of 8 cm with an R^2 of 0.49 and $p<10^{-9}$. As this correlation becomes insignificant when it is calculated for the periods before and after the snow separately, it can be related to the strong decrease in $R^{18}_{eco}O$ after the snow event that correlates to a rise in soil moisture when the snow melts (Fig. 2.10). This would be consistent with a heavier ^{18}O composition in the top soil layers (due to evaporation) before the snow, yielding also higher $\delta^{18}O$ values of $R^{18}_{eco}O$. Additionally, other variables that correlated significantly with $R^{18}_{eco}O$ during the whole measurement period such as soil and air temperatures or shortwave radiation (Table 2.9) are related to soil evaporation. For the sub-periods before and after the first snow, we found multiple significant correlations with meteorological drivers such as soil and air temperatures, pressure or actual vapor pressure (Table 2.9). The significant correlations before the first snow become insignificant (or less significant) after the snow and vice versa. This behavior indicates a difference in the processes that drive the ^{18}O isotopic composition of nighttime net ecosystem CO_2 exchange $R^{18}_{eco}O$ before and after the snow event.

Table 2.9: R^2 values for correlations between the ^{18}O composition of nighttime CO_2 exchange $R^{18}_{eco}O$ and different meteorological variables. Significance thresholds are given by *** for $p<10^{-4}$, ** for $p<10^{-3}$ and * for $p<10^{-2}$. For some parameters the height above the ground (with negative values indicating the depth below the ground) is given in brackets; the parameters without such indication are measured 42 m above the ground.

	All periods		Before the snow		After the snow	
Soil moisture (-8 cm)	0.49	***	0.04		0.00	
Upwards shortwave radiation	0.40	***	0.28	*	0.04	
VPD	0.18	**	0.09		0.22	
Soil temperature (-8 to -64 cm)	0.36	***	0.06		0.70	***
Air temperature	0.22	**	0.02		0.61	**
Air temperature (2 m)	0.21	**	0.05		0.60	**
Upwards longwave radiation	0.20	**	0.02		0.61	**
Incoming longwave radiation	0.05		0.49	***	0.03	
Ambient pressure	0.05		0.39	***	0.36	*
Incoming shortwave radiation	0.39	***	0.23	**	0.13	
Dew point temperature	0.02		0.38	***	0.14	
Specific humidity	0.02		0.34	***	0.17	
H_2O mole fraction	0.02		0.34	***	0.17	
Actual vapor pressure	0.02		0.33	***	0.18	
Relative humidity	0.28	***	0.31	***	0.15	
Rain	0.01		0.28	**	0.05	

2.5 Conclusions

Field-applicable instruments to analyze the isotopic composition of CO_2 have a large potential to be useful for long-term measurement setups on meteorological towers and networks such as ICOS (https://www.icos-ri.eu/) or NEON (http://www.neonscience.org/) to deliver new insights into the carbon cycle. The new isotope ratio infrared spectrometer (IRIS) Delta Ray used in this study provides an opportunity to measure the CO_2 mole fraction C_{CO2} and its isotopic compositions $\delta^{13}C$ and $\delta^{18}O$ with limited maintenance effort at remote sites. Here, we evaluate the instrument internal calibration and demonstrate the field applicability of the Delta Ray IRIS, which we used to measure c, $\delta^{13}C$ and $\delta^{18}O$ in a managed beech forest for 3 months in autumn 2015. The Delta Ray IRIS implemented here with the instrument's internal calibration, showed adequate precision, accuracy and repeatability to perform robust measurements of c, $\delta^{13}C$ and $\delta^{18}O$ in air in our continuous setup. For measurements of δ values at mole fractions that deviate from the 'referencing' mole fraction, the uncertainty is dominated by the instrument internal correction of mole

fraction dependency and improvements in the accuracy could potentially be achieved by more detailed analysis of this mole fraction dependency. The easy operation of the automatically calibrated Delta Ray IRIS allowed us to measure seasonal variability of the isotopic composition of nighttime CO_2 exchange based on Keeling plots. The strong effect of the first frost and snow event on both the $\delta^{13}C$ and $\delta^{18}O$ of nighttime CO_2 exchange indicates that singular events, even if short, may strongly influence the isotopic imprint of terrestrial ecosystems on atmospheric CO_2.

2.6 Code availability

An earlier version of the multilayer model CANVEG can be found here:
https://nature.berkeley.edu/biometlab/BiometWeb/canoak_V2.c

2.7 Data availability

All data used for the figures presented here is provided in the supplementary of the published paper Braden-Behrens et al., 2017a.

2.8 Author contributions

The authors contributed to this paper in the following ways: The experimental setup and data processing were carried out, discussed and interpreted by Jelka Braden-Behrens and Alexander Knohl. The validation of and simulations with the multilayer model CANVEG (Sect. 2.3.9) were performed, discussed and interpreted by Yuan Yan, Jelka Braden-Behrens and Alexander Knohl. All authors proof-read and commented on the paper.

2.9 Competing interests

We declare that we have no conflict of interest. However, we borrowed the instrument at no cost from *Thermo Scientific*, Waltham, USA, to perform instrument tests and to use the instrument under field conditions. Additionally we could do lab measurements to evaluate the calibration strategy at the facility of Thermo Scientific in Bremen at no cost. Jelka Braden-Behrens and Alexander Knohl published a short (not peer reviewed) technical paper (Braden-Behrens et al., 2017b) together with Hans-Jürg Jost and Magda Mandic, who were both working for *Thermo Scientific*, when we borrowed the instrument. This not peer reviewed technical paper also briefly describes our experimental setup and discusses instrument performance.

2.10 Acknowledgements

This project was partly funded by the Dorothea-Schlözer-Fellowship and by the German Research Foundation (DFG, project ISOFLUXES KN 582/7-1). The work was partially supported by the European Research Council under the European Union's Horizon 2020 research and innovation programme (grant agreement no. 682512 – OXYFLUX). We thank *Thermo Scientific*, Waltham, USA, for lending us the instrument for free and for making it possible for us to perform additional measurements in the lab. We particularly thank Hans-Jürg Jost, Magda Mandic and Danijela Smajgl for their advice and support, especially concerning how to set up, calibrate and operate the Delta Ray analyzer. The technicians of the bioclimatology group of the University of Göttingen, especially Dietmar Fellert Frank

Tiedemann and Edgar Tunsch as well as the student assistant Elke Schäpermeier, helped substantially with the experimental setup and maintenance. We thank Yakov Kuzyakov, Lydia Gentsch and Mattia Bonazza for their remarks on data interpretation. Additionally, we thank the forest manager Ulrich Breitenstein for allowing the experimental setup at this site.

2.11 Appendix

2.11.1 Measures to improve data quality

To reduce the uncertainty of the calculated isotopic composition of nighttime CO_2 exchange (respiration) $R^{13}_{\text{eco}}\text{C}$ and $R^{18}_{\text{eco}}\text{O}$, we used the following approaches concerning setup and post-processing.

- **Minimizing the sampling time**
  One of the key assumptions of the Keeling plot approach in Eq. (2.1) is the mixing of a constant background with one (integrated) source. This assumption is justified if there is no significant change in the background mole fraction c_{bg}, its isotopic composition δ_{bg}, and the isotopic composition of the (integrated) source δ_s for all data points that are taken into account for a single Keeling plot. For the case of an integrated source, a constant δ_s can be ensured when the isotopic composition of the individual source components $\delta_{s,i}$ and the relative contribution of the individual source components α_i in Eq. (2.2) are constant. As all these quantities ($\delta_{s,i}$, α_i, c_{bg} and δ_{bg}) can vary with time, this assumption tends to be violated more often for longer measurement times. Thus, the uncertainty of calculated Keeling plot intercepts can be reduced by minimizing the measurement time, as discussed for example by Bowling et al. (2003a), who recommend the use of measurements that took less than five hours for analyzing Keeling plot intercepts for $\delta^{18}O$. As our setup measured all of the nine heights within 30 minutes, we were able to calculate Keeling plots for shorter periods. During data analysis we calculated Keeling plots on timescales between 30 min and 5 h.
- **Increasing the CO_2 mole fraction range**
  The linear regression that underlies the Keeling plot, can be improved significantly by increasing the CO_2 mole fraction (Zobitz et al., 2006). In our setup, we increase the CO_2 mole fraction range by using data from all nine inlet heights within one Keeling plot, but this, on the other hand, could violate the assumption of constant relative contributions of the individual source components α_i in Eq. (2.2) to the integrated source. To analyze whether there is any bias (which may have several contributions) due to the inclusion of the different inlet positions, we evaluated the Keeling plots for the lower inlets (heights 1-4) and for all inlets (heights 1-9) separately. The difference Δ between the these Keeling plot intercepts based on different data sets showed a symmetric frequency distribution around 0 (Fig. 2.13 in the supplementary material). By including all heights into the data analysis, we reduced the error of the intercept σ from a mean value of $\overline{\sigma_{low}} \approx 1.5\,‰$ to $\overline{\sigma_{all}} \approx 0.8\,‰$ for both isotopic species. These numbers refer to Keeling plots that include data from three consecutive measurement

cycles, yielding a temporal resolution of 90 min. Reasons for the choice of this time resolution are given below.

- **Performing an ordinary Model I regression instead of a Model II regression**
  We used an ordinary Model I regression instead of a Model II regression. According to Zobitz et al. (2006), this approach takes into account that the error of the measured δ values dominates over the error of the measured mole fractions and yields unbiased estimates of the Keeling plot intercept. In our setup, the application of a Model I regression can be justified by the fact that the relative precision of δ measurements is more than an order of magnitude larger than the relative precision of the CO_2 mole fraction measurements: To estimate the relative precision of the three measured quantities, we calculated the ratio of the Allan deviation at our measurement time of 20 s over the typical range of c, $\delta^{13}C$ and $\delta^{18}O$. We further define the typical range as the median of the ranges that were obtained during the 30 minutes measurement cycles. Thus, with the Allan deviations in Table 2.5 and with typical ranges of 26 ppm, 1.5‰ and 1.1 ‰ for c, $\delta^{13}C$ and $\delta^{18}O$, the relative precision for the obtained variability in CO_2, $\delta^{13}C$ and $\delta^{18}O$ is on the order of 10^{-3}, 10^{-2} and 10^{-1}, respectively. Thus, the relative precision of the mole fraction measurement is at least an order of magnitude better than the relative precision of δ measurements.

- **Filtering data to get only high quality linear regressions**
  Data filtering to remove bad quality and biased (Model II) linear regressions has been often done by excluding data with a to low CO_2 mole fraction range (Bowling et al., 2005; Pataki et al., 2003). Whereas Pataki et al. (2003) recommend the exclusion of all data from the analysis that spans a CO_2 range below 75 ppm, Bowling et al. (2005) chose this threshold to be 40 ppm. This data filtering approach, based on CO_2 mole fraction range, does not seem necessary when applying a Model I regression: Zobitz et al. (2006) analyzed consequences of small CO_2 mole fraction ranges numerically as well as analytically and concluded that for Keeling plot intercepts based on Model I regressions 1) a bias at low CO_2 mole fraction ranges is not expected at current analytical error levels and 2) that errors in the intercept can be small, even for small CO_2 mole fraction ranges, if the δ values are measured accurately enough. Figure 2.14 in the supplementary material shows the relationship between the CO_2 mole fraction range and the standard error of the intercept σ for a measurement period of 30 minutes. This figure also shows two comparable approaches for data filtering that accept 85 % of the data: One approach would be to directly remove data with large intercept errors and the other approach, as mentioned above, would be to remove data with too-low CO_2 range. As is visible in Fig. 2.14 in the supplementary material, this approach would remove considerable amounts of data with a very small standard error of the intercept σ, which might be good quality data. For this reason (and as we do not expect a bias occurring for small CO_2 mole fraction ranges for our Model I-type regression), "we decide for a direct filtering based on a σ threshold. We filtered out data with σ values larger than the 85^{th} percentile of all σ's. The filtered nighttime Keeling plot intercepts based on 90 minutes of data acquisition had R^2

values with a median of 0.87 and 0.81 for ^{13}C and ^{18}O, with mean values of 0.85 and 0.77 and standard deviations σ of 0.1 and 0.16 respectively. Example Keeling plots with R^2 values spanning the range of mean $\pm 1\,\sigma$ are provided in the supplementary material (in Fig. 2.17 in the supplementary material).

- **Removing outliers**
  Our setup, based on the measurement of $\delta^{13}C$, $\delta^{18}O$ and CO_2 mole fraction c, enabled us to calculate individual Keeling plots based on all inlet heights (heights 1-9) with a temporal resolution of 30 min. We calculated Keeling plots on different timescales ranging from 30 min to 5 h by using 1 to 10 measurement cycles and evaluated how the Keeling plot intercepts $\delta^{13}C_{KP}$ and the corresponding standard errors of the linear regression σ changed (Fig. 2.15 in the supplementary material). Additionally, the calculation of Keeling plot intercepts based on longer timescales increased the number of Keeling plot intercepts within reasonable ranges. For Keeling plots that were averaged over 2h (5h), a fraction of 97% (99%) of the Keeling Plot intercepts was between -33 and -25 ‰. Because the range of the Keeling plot intercepts should not depend on the chosen timescale, we considered the Keeling plot intercepts that were outside of this range as outliers and removed them from further analysis (also for Keeling plot intercepts that were based on shorter timescales).

- **Choosing a time resolution for individual Keeling plots**
  To decide on a suitable time resolution to analyze the temporal variability of the Keeling plot intercepts, we had to solve the trade-off between 1) more accurate data on longer timescales and 2) a larger number of data points that were available (after the above-mentioned filtering procedures). We decided to fit the individual Keeling Plots on 90 min resolution, which yields a maximal number of $N_{filtered} \approx 2300$ accepted data points and a median of 0.76 ‰ for the standard errors σ (Fig. 2.16 in the supplementary material).

- **Calculation of weighted means for nighttime data**
  For analyzing variations in the nighttime CO_2 exchange (respiration) R_{eco} on seasonal timescales we used the (filtered) individual Keeling plots, each based on 90 minutes of input data, and calculated the mean over all Keeling plots that were collected between 21h30 and 2h30 local winter time (GMT+1), using the weight w based on the standard error σ of the Keeling plot intercept: $w = 1/\sigma^2$.

2.12 Supplementary figures

In the supplementary material of this paper, we present the following figures:

- Figure 2.13:
  Difference between Keeling-Plot intercepts based on all inlets and based on only the lower inlets
- Figure 2.14:
  Example relationship between the standard error of the Keeling-Plot intercept and the CO_2 concentration range

- Figure 2.15:
  Distributions of the Keeling-Plot intercepts and their standard errors based on differently long measurement periods
- Figure 2.16:
  Number of accepted data points after filtering and boxplots of standard errors for differently long measurement periods
- Figure 2.17:
  Example nighttime Keeling-Plots with typical R^2 values

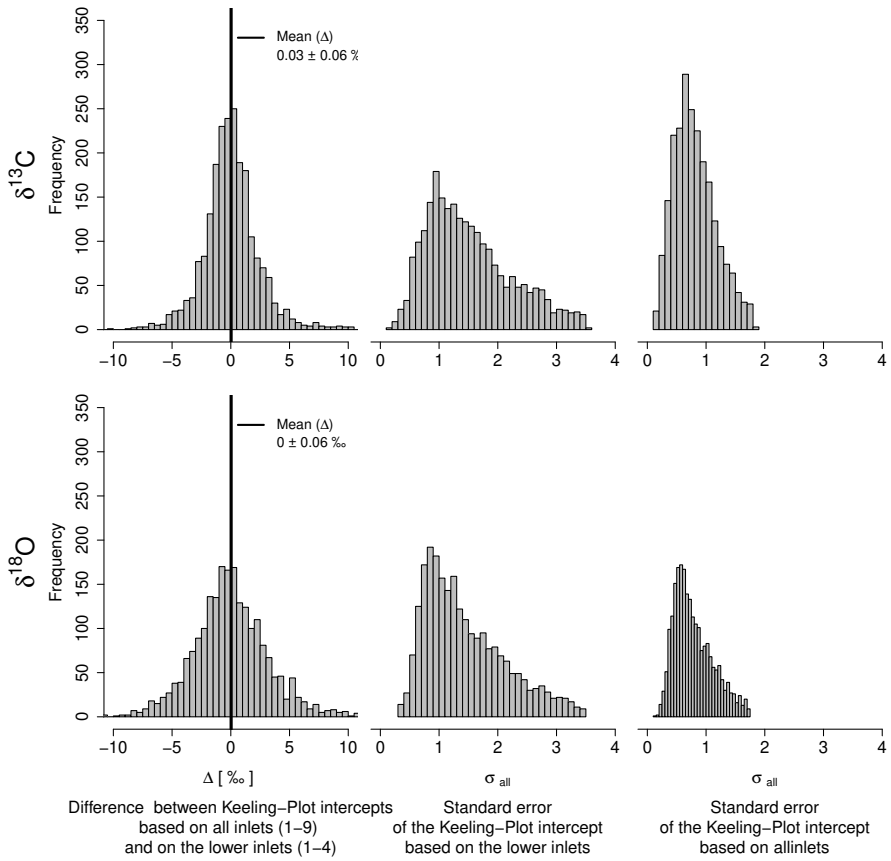

Figure 2.13: Left panels: Frequency distributions (grey bars) and mean value (black lines) of the difference $\Delta[‰]$ between the Keeling-Plot intercepts based on all inlets (*all*, heights 1-9) and based on only the lower inlets (*low*, heights 1-4). Middle and right panel: Frequency distributions for the corresponding standard errors of the Keeling-Plot intercepts σ_{low} and σ_{all}. First column: δ^{13}C; Second column: δ^{18}O. For both isotopic species, Δ shows a symmetric distribution around 0 and the large range of Δ can be explained by the comparatively large standard errors σ of the Keeling plot intercepts σ_{low} and σ_{all}. All data shown here refers to a measurement time of 90 min, thus including 3 measurement cycles into a single Keeling Plot.

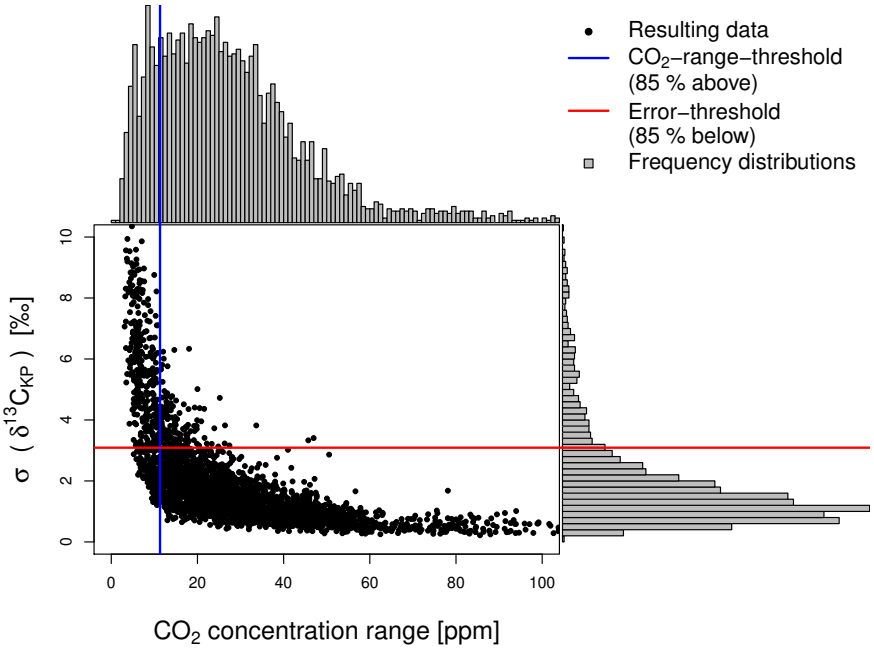

Figure 2.14: An example for the relationship between the standard error σ of the Keeling-Plot intercept $\delta^{13}C_{\mathrm{KP}}$ and the CO_2 concentration range. Each individual Keeling-Plot included here is based on a 30 min measurement period. The gray shaded areas are frequency distributions for both variables. The blue and the red line illustrate different approaches to exclude bad quality data based on 1) to low CO_2 range (blue) and 2) to large intercept standard error σ (red). This plot illustrates how a CO_2 concentration range based filtering would negatively effect data quality. The equivalent plot for ^{18}O (not presented here) shows similar behavior.

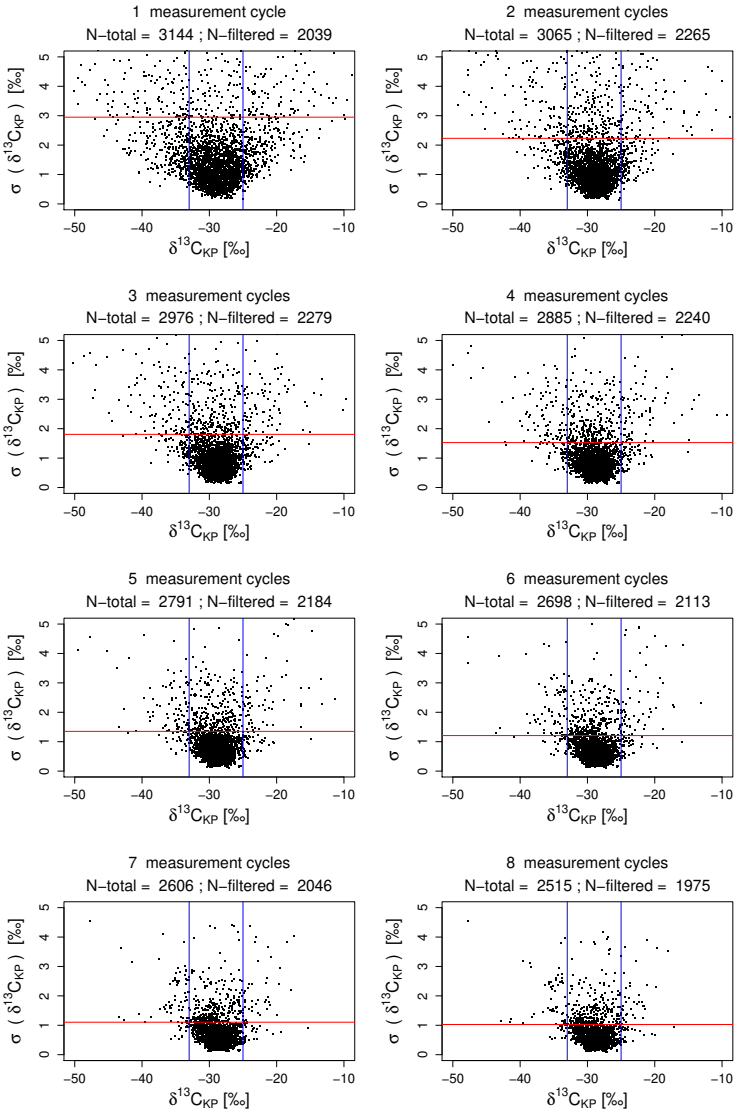

Figure 2.15: The distribution of the Keeling-Plot intercepts $\delta^{13}C_{KP}$ and its standard errors σ changes when more measurement cycles are included into a single Keeling-Plot. The red lines show the 85-percentile of standard errors. We used this 85-percentile threshold to filter out data with bad quality linear regressions. The blue lines mark the absolute values of -33 ‰ and -25 ‰. The more measurement cycles are included into a Keeling Plot, the fewer data points are out of this range, which should not depend on the number of measurement cycles that are used. These values are chosen as absolute thresholds to detect and exclude outliers.

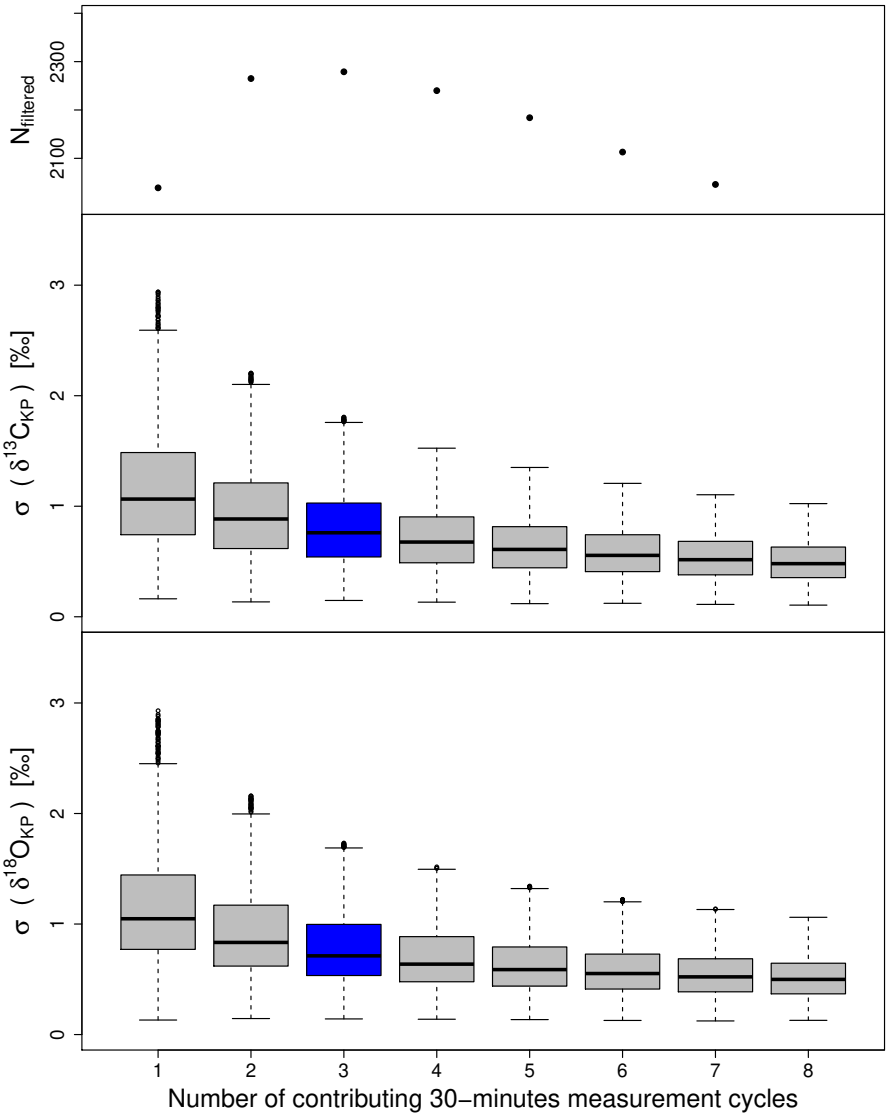

Figure 2.16: Top panel: The number of accepted data points $N_{filtered}$ (after filtering and outlier removal) depends on the number of measurement cycles that are included into each Keeling plot. Middle and bottom panel: Illustration of the distribution and the range of the standard error σ of the Keeling-Plot intercepts using Box-Whiskers-Plots (whiskers following the definition of a Tukey boxplot), we choose to use three measurement cycles in each Keeling-Plot, the corresponding Box-Whiskers-plot is marked in blue.

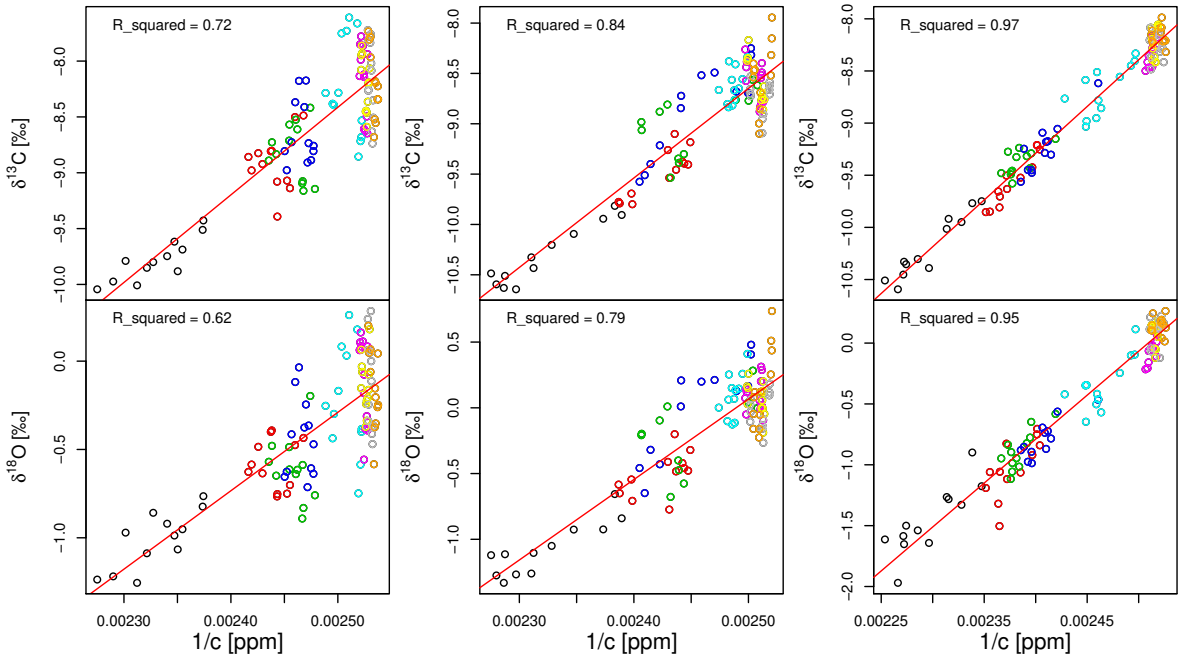

Figure 2.17: Example nighttime Keeling-Plots with typical R^2-values (spanning the range of the mean $\pm\sigma$. Each Keeling-Plot is based on 90 min input data. Different colors represent different inlet heights

CHAPTER 3

Eddy covariance measurements of the dual isotope composition of evapotranspiration

Manuscript to be submitted to 'Agricultural and Forest Meteorology' (Braden-Behrens et al., 2018b)

3.1 Abstract

Measurements of the isotopic composition of water vapor (H_2O_v) provide valuable insights into the hydrological cycle, whereas eddy covariance (EC) measurements are widely used to quantify biosphere-atmosphere exchange processes. Yet, the direct combination of water isotope approaches and the EC method remains challenging. Here, we present the first time series of EC measurements of the isotopic composition of evapotranspiration (ET) for both $\delta^{18}O$ and δD based on fast (2 Hz) measurements. The measurements were performed over the full growing season of a forest ecosystem in central Germany and showed a seasonal variability from −19 to 0 ‰ for $\delta^{18}O_{ET}$ and from −140 to −25 ‰ for δD_{ET}. Our isotope EC setup is based on 2 Hz measurements of the mole fraction and isotopic composition of water vapor ($C_{H2O,v}$, δD and $\delta^{18}O$) in 44 m height. For these measurements we used a high flow and high-frequency-customized version of a commercially available water vapor isotope analyzer. We quantified the precision of this analyzer by measuring the Allan deviation, which is below 0.5 ‰ for $\delta^{18}O$ and below 1.4 ‰ for δD for averaging times between 0.5 and 1000 s. The potential accuracy of this analyzer is approximately 0.16 ‰ and 0.5 ‰ for $\delta^{18}O$ and δD, respectively. The setup-specific limitations of our measurements, e.g. the measurement frequency of 2 Hz, yield a mean bias of 0.03 mmol $m^{-2}s^{-1}$ of the measured net water flux. Spectral and cospectral analysis showed, that high-frequency dampening was less pronounced for our EC setup (which was equipped with heated tubing) than for the standard EC setup at this site. Further, the similarity between the obtained spectra and cospectra among the different isotopologues of water vapor indicates that there are no isotope selective tubing effects. Thus, we conclude that direct EC measurements of the isotopic composition of ET are feasible for both, $\delta^{18}O_{ET}$ and δD_{ET}. We propose that EC measurements of the isotopic composition of ET could further be used to partition ET and thus improve our understanding of the hydrological cycle, in particular in situations when flux gradient methods show limited applicability. Our simultaneous measurement of δD_{ET} and $\delta^{18}O_{ET}$ enables us to evaluate the seasonal variability of the isotopic composition in the $\delta^{18}O$-δD-plane. This evaluation reveals the difference between transpiration-dominated and evaporation-dominated times and highlights the potential of simultaneous measurements of $\delta^{18}O_{ET}$ and δD_{ET}.

3.2 Introduction

Stable isotopes are a promising tool to enhance our understanding of ecosystem gas exchange on various scales (e.g. Dawson et al., 2002; Yakir et al., 2000). In particular, studying $\delta^{18}O$ and δD in water vapor can provide insights into the hydrological cycle (see e.g. Gat, 1996; Griffis, 2013; Wang et al., 2000). Measurements of stable isotopes in water vapor (H_2O_v) have been used for example to partition, constrain and estimate evapotranspiration (ET) (Wang et al., 2000). Particularly on an ecosystem scale, measurements of the isotopic composition of ET have been carried out mainly based on Keeling plot[1] (Wang et al., 2010;

1 Here we define the Keeling plot approach by the calculation of the intercept of δ values against the reciprocal mole fractions that can be derived from the conservation of mass in a two component mixing model. In particular, we use the term Keeling plot independently of the temporal or spatial separation of the measurement points.

Table 3.1: Nomenclature and abbreviations used in this publication.

	General nomenclature
c	Atom and isotope mole fractions (e.g c_{heavy})
C	Molecule mole fractions (e.g. $C_{\mathrm{H2O,v}}$)
σ_A	Allan deviation
$S_{\alpha\alpha}(f)$	Energy spectrum of $\alpha(t)$; $S_{\alpha\alpha}(f) = \ldots = \lvert\mathcal{F}[\alpha(t)]\rvert^2$
$\mathrm{cosp}_{\alpha\beta}(f)$	Cospectrum between $\alpha(t)$ and $\beta(t)$; $\mathrm{cosp}_{\alpha\beta}(f) = \ldots = \mathcal{F}[\alpha(t)]^* \cdot \mathcal{F}[\beta(t)]$
Re	Reynolds number
	Stable isotope specific notations
C^{klm}	Isotopologue mole fraction (in AFGL notation)
	with k, l and m as the isotopes mass numbers modulo 10
R	Isotope ratio defined as $R := c_{\mathrm{heavy}}/c_{\mathrm{light}}$
R_{std}	Isotopic ratio of a standard material
δ	Relative deviation of the measured isotope ratio from R_{std}
δ_a	Atmospheric delta values
	Isotope Flux quantities
$F_{C^{klm}}$	Isotopologue flux; $F_{C^{klm}} = \bar{\rho}_a \, \overline{w' C^{klm\,\prime}}$
IF_δ	Isoforcing; $\mathrm{IF} = \overline{w'\delta'}$
I_C	Isoflux; $I_C := \overline{w'(\delta \cdot C)'}$
	Abbreviations
EC	Eddy covariance
ET	Evapotranspiration
WVIA	Water vapor isotope analyzer
EP-WVIA	Enhanced performance water vapor isotope analyzer (*Los Gatos*)
2 Hz-HF-WVIA	WVIA for 2 Hz measurements (with high flow plumbing)
WVISS	Water vapor isotope standard source (*Los Gatos*)
DPG	Dew point generator
HF-WVISS	WVISS optimized for high flow
VSMOW	Vienna standard mean ocean water
HITRAN	High-resolution transmission molecular absorption
AFGL	Air force geophysics laboratory
IRMS	Isotope ratio mass spectrometry
IRGA	Infrared gas analyzer
LMWL	Local meteoric water line

Wei et al., 2015; Williams et al., 2004; Yakir et al., 1996) and flux gradient approaches (Hu et al., 2014; Lee et al., 2007; Welp et al., 2008; Wen et al., 2016). Keeling plot approaches (Keeling, 1958) assume the mixing of only two components (see e.g. Pataki et al., 2003) whereas the flux gradient method is based on Monin and Obukhov similarity theory (Kaimal et al., 1994; Monin et al., 1954) and assumes a common eddy diffusivity for different isotopologues[1] (Griffis, 2013). Both methods have their limitations: For the Keeling plot method, the underlying two-component-assumption has been shown to be violated in numerous studies (reviewed by Griffis, 2013). Flux gradient methods on the other hand show generally limited reliability in some applications (in particular above tall vegetation) (Griffis, 2013). Thus, the more direct EC method, that has comparably few theoretical assumptions (Griffis et al., 2010) and can be derived from first principles, could provide an alternative or supplement to flux gradient and Keeling plot methods (Griffis, 2013). However, for the application of the EC method, high-frequency measurements are needed (e.g. Werner et al., 2012).

Over the last decades, the potential of measurements of the isotopic composition with high temporal resolution increased due to progress in optical-based measurement techniques (e.g. Werner et al., 2012). In particular, isotope ratio infrared spectroscopy (IRIS) facilitated near continuous and high-frequency measurements of isotopic compositions (Wen et al., 2016). Thus, with recent developments in laser spectroscopy, also direct EC measurements for stable isotopologue fluxes became feasible. In the last years, a number of studies showed applications of direct EC measurements of the isotopic composition of CO_2 fluxes (Griffis et al., 2008; Sturm et al., 2012; Wehr et al., 2013) and use these measurements to partition net CO_2 fluxes into respiration and photosynthesis (Oikawa et al., 2017; Wehr et al., 2016). For water vapor, there is only one study that directly measured the $\delta^{18}O$ composition of ET using the EC technique with a fast (>2 Hz) lead-salt tunable diode laser spectroscopy system (TGA200, *Campbell Scientific Inc.*, Logan, UT, USA) (Griffis et al., 2010). In this study, carried out above a corn/soybean canopy, ET acted to enrich the atmosphere in ^{18}O and the diurnal cycle of $\delta^{18}O_{ET}$ showed a progressive enrichment throughout the day. Further, at the same field site, Griffis et al. (2011) carried out simultaneous EC measurements of $\delta^{18}O$ in CO_2 and H_2O_v and used the obtained data to study the oxygen exchange between CO_2 and H_2O on an ecosystem scale. Another implementation of the EC technique used the slower standard version of the off-axis integrated cavity output spectrometer (WVIA, *Los Gatos Research Inc.*, San Jose, CA, USA) to measure the isotopic composition of both $\delta^{18}O_{ET}$ and δD_{ET} (Good et al., 2012). This instrument is capable of 1 Hz data acquisition but has an internal cell residence time of 5.7 s (Good et al., 2012), dampening the measurement frequency below 0.2 Hz.

Reasons for the sparse availability of EC measurements of the isotopic composition of ET can be found in the limited availability of fast laser spectrometers as well as complications related to condensation and dampening effects in tubes. If these problems can be overcome,

1 Isotopologues are defined e.g. by Coplen (2011) as 'Molecular species that differ only in isotopic composition (number of isotopic substitutions) and relative molecular mass'.

direct EC measurements of the isotopic composition of ET can provide an alternative or a supplement to flux gradient and Keeling plot methods. In particular, the simultaneous measurement of δ_{ET} for both, $\delta^{18}O$ and δD could be a promising tool for the analysis of the hydrological cycle on an ecosystem scale. In other contexts, dual isotope approaches have been proven to provide valuable insights into the isotopic composition of precipitation (Dansgaard, 1964), the isotopic composition of water vapor in the surface layer (Welp et al., 2012) and in the planetary boundary layer (Griffis et al., 2016), or to analyze the water uptake by plants (Bowling et al., 2017; Meissner et al., 2014).

The objective of this study is to demonstrate the capability of the high-flow and high-frequency optimized water vapor isotope analyzer (2 Hz-HF-WVIA, *Los Gatos Research Inc.*, San Jose, CA, USA) to perform continuous 2 Hz measurements of H_2O_v. We evaluate the analyzer's precision and potential accuracy and discuss the capability and limits of our setup to perform EC measurements based on the measured spectra and cospectra. Moreover, we present the diurnal and seasonal variability of the isotopic composition of ET in a managed beech forest as measured with EC.

3.3 Methods

3.3.1 Field site

We carried out this study at a 44 m high meteorological measurement tower in a managed beech forest (*Fagus sylvatica L.*) in Thuringia (central Germany) located at 51°19'41,58" N; 10°22'04,08" E; 450 meters above sea level. The forest in the surrounding of the meteorological tower is composed of four relatively homogeneous stands (with an age of 30-40, 80, 125 and 180 years respectively) with the 125 years old stand in the dominant wind direction in the southwest of the tower (Anthoni et al., 2004). The height of this stand, defined as the average height of the 20 % largest trees was 37 m in 2004, and the maximum effective leaf area was approximately 4 m^2m^{-2} (Anthoni et al., 2004). The mean annual air temperature between 2002 and 2016 was approximately 8.3 °C with a standard deviation of 0.7 °C, and the mean annual precipitation was approximately 600 mm with a standard deviation of 150 mm (personal communication: Rijan Tamrakar,University of Goettingen, Bioclimatology, Faculty of Forest Sciences and Forest Ecology, Goettingen, Germany). In 2016, when our measurements took place, the mean annual temperature was 8.73 °C and annual precipitation was approximately 660 mm (personal communication: Rijan Tamrakar,University of Goettingen, Bioclimatology, Faculty of Forest Sciences and Forest Ecology, Goettingen, Germany).

3.3.2 Theory

3.3.2.1 Stable isotopes - definitions and constants

To quantify isotopic compositions, we use the standard δ notation that gives the relative deviation of the isotopic ratio R from the corresponding ratio of a standard material R_{std} (cf. Coplen, 2011).

$$\delta := \frac{R - R_{std}}{R_{std}} \qquad \text{with} \qquad R := \frac{c_{heavy}}{c_{light}} \tag{3.1}$$

With the mole fractions c_{heavy} and c_{light} of the respective heavier and lighter isotopes. All δ values given in this paper are referring to Vienna Standard Mean Ocean Water (VSMOW) with $R^{D/H}_{\text{VSMOW}}$=155.76 × 10^{-6} and $R^{18/16}_{\text{VSMOW}}$ = 2005.2 × 10^{-6} (NIST, 2005). As large parts of our data analysis are based on isotopologue mole fractions instead of isotope ratios, we additionally use the so-called Air Force Geophysics Laboratory (AFGL) notation (Rothman et al., 2003). This notation directly refers to the mole fractions of the different isotopologues using a three-digit-notation C^{klm}, where k, l and m are the mass numbers of the respective isotopes modulo 10. In AFGL notation, the four most prevalent isotopologues of water (with their relative natural abundances in parenthesis) are C^{161} (0.997), C^{181} (2.2×10^{-3}), C^{171} (3.7×10^{-4}) and C^{261} (3.1×10^{-4}). The natural abundances given here are taken from the HITRAN database (Rothman et al. 2013, derived from De Biévre et al. 1984). A set of formulae to switch from the common δ notation to the AFGL notation are given by Wehr et al. (2013) for the case of CO_2. To convert from one notation to the other, we followed this procedure in an analogous manner for H_2O, with the exception of the correction for ^{17}O. Here, we assume a fixed ratio of $R^{17/16} = 3.7 \times 10^{-4}$.

3.3.2.2 The eddy covariance (EC) method

The EC method relates the net fluxes through the canopy-atmosphere interface directly to turbulent motions in the atmosphere (Baldocchi, 2003). This method is based on fast (normally 10 to 20 Hz) measurements of the vertical wind velocity w in combination with a molecule's mole fraction C (for molecule fluxes), potential temperature θ (for heat flux) or horizontal velocity u (for momentum flux) (e.g. Stull, 1988). The EC technique relates F_C, the temporally averaged vertical flux of a molecule through a plane at a certain height above the canopy (from here: eddy flux density or eddy flux) to the measured time series $C(t)$ and $w(t)$ (Baldocchi, 2003). Using Reynolds averaging (C=$\bar{C} + C'$ and w=$\bar{w} + w'$) the eddy flux density F_C can be expressed as the covariance between C and w (see e.g. Baldocchi, 2003).

$$F_C = \bar{\rho_a} \underbrace{\overline{w'(t)C'(t)}}_{\text{cov}(w,C)} = \bar{\rho_a} \int_0^\infty \text{cosp}_{w',C'}(f)\, \mathrm{d}f \tag{3.2}$$

The bar denotes the temporal average over the chosen period - e.g. 30 min, $\bar{\rho_a}$ is the mean molar density of air, and cosp(f) is the one-sided cospectrum[1]. The underlying assumptions of this method are fully developed turbulence, a homogeneous terrain, stationarity of the data, and negligible density fluctuations (Foken et al., 1996). Further, the total flux of a molecule from/into an ecosystem is split into the flux into the air layers below the measurement height (the storage term) and the corresponding eddy flux density. In case of water vapor flux, this means evapotranspiration ET is composed of the water vapor eddy

1 Here we use the definition of $\text{cosp}_{w',C'}$ that is given e.g. by Kaimal et al. (1994) as $\text{cosp}_{w',C'}(f)$=Ree[$\mathcal{F}(R_{w'C'})$] with the cross covariance $R_{w',C'}$:=$\int w'(\tau)C'(\tau + t)\,\mathrm{d}\tau$. Using the cross correlation theorem, this can be transformed into $\text{cosp}_{w',C'}(f)$=$\mathcal{F}[w'(t)]^* \cdot \mathcal{F}[C'(t)]$, a formula given e.g. by Stull (1988).

flux $F_{C_{H2O}}$ and the storage S of water vapor: $ET = F_{C_{H2O}} + S$ (cf. Griffis et al., 2010).

3.3.2.3 Isotope EC measurements

The EC method can also be applied to the different isotopologues of a molecule separately. Thus, the eddy flux density (or eddy flux) $F_{C^{klm}}$ of an isotopologue can be calculated from the time series of vertical wind velocity w and the isotopologues mole fraction C^{klm} (e.g. Wehr et al., 2013).[1]

$$F^{klm} := \bar{\rho_a}\,\overline{w' C^{klm\,\prime}} \tag{3.3}$$

The isotopic composition of a molecule's eddy flux δ_F can be calculated directly from the corresponding isotopologue fluxes (Wehr et al., 2013). In case of water vapor, the isotopic composition of the eddy flux density has been equated with the isotopic composition of ET by various authors for a wide range of different ecosystems such as a semi-arid mixed savanna (Good et al., 2012), a temperate grassland (Hu et al., 2014), an artificial oasis cropland (Huang et al., 2014; Wang et al., 2016; Wen et al., 2016), agricultural sites (Griffis et al., 2010; Griffis et al., 2011; Welp et al., 2008) or a temperate forest (Lee et al., 2007). These studies explicitly or implicitly assume that the storage of water vapor below the measurement height (cf. eg. Aubinet et al., 2003) are negligible when measuring the isotopic composition of δ_{ET} on ecosystem scale. This assumption was tested by Welp et al. (2008), who found no bias between δ_{ET} and the isotopic composition of water vapor storage $\delta_{\mathrm{storage}}$. For the field site of our study we analyzed the contribution of the storage of water vapor to ET using standard EC measurements and profile data for the whole year 2016 (Fig. 3.16 in the supplementary material). This analysis indicates, that the magnitude of ET and the water vapor eddy flux deviate only by approximately 3 %. Thus, we neglect the influence of the storage term and equate the isotopic composition of ET with the isotopic composition of the measured water vapor eddy flux. In general, this equalization could still be violated (even with small storage fluxes), if the isotopic composition of the storage term would largely deviate from the isotopic composition of ET. However, we also use this equalization to be consistent to the above mentioned studies, that measure δ_{ET} on ecosystem scale (Good et al., 2012; Griffis et al., 2010; Griffis et al., 2011; Hu et al., 2014; Huang et al., 2014; Lee et al., 2007; Wang et al., 2016; Welp et al., 2008; Wen et al., 2016). Thus, we estimate the isotopic composition of ET on ecosystem scale by:

$$\delta^{18}\mathrm{O}_{\mathrm{ET}} = \frac{F^{181}/F^{161} - R^{18/16}_{\mathrm{VSMOW}}}{R^{18/16}_{\mathrm{VSMOW}}} \qquad \delta\mathrm{D}_{\mathrm{ET}} = \frac{F^{261}/(2F^{161}) - R^{D/H}_{\mathrm{VSMOW}}}{R^{D/H}_{\mathrm{VSMOW}}} \tag{3.4}$$

The factor of two in case of deuterium takes into account the two different equivalent positions of the hydrogen/deuterium atom in the water molecule (Kerstel, 2004), as

1 An alternative characterization of isotopic fluxes is the so called isoflux $I_C := \overline{w'(\delta \cdot C)'}$ that can be approximated by the product of δ_F (e.g. $\delta^{18}\mathrm{O}_{\mathrm{ET}}$ in equation 3.4) and F_C (Wehr et al., 2013).

described for oxygen in CO_2 by Wehr et al. (2013).

Further, the covariance between w' and δ' can be evaluated directly and is called ecosystem scale isoforcing IFδ. This quantity is related to the corresponding flux F_C and its isotopic composition δ_F in the following way (Lee et al., 2009):

$$\mathrm{IF} := \overline{w'\delta'} = \frac{F_C}{C_a \bar{\rho_a}}(\delta_F - \delta_a) \tag{3.5}$$

With the molecule's mole fraction C_a, the mean molar density of air $\bar{\rho_a}$, and the isotopic composition of the atmosphere δ_a. By setting up an isotopic mass balance (see e.g. Lai et al., 2011) the isoforcing-related change in the atmospheric δ can be related to IF according to Eq. 3.6 (see Sturm et al., 2012). The underlying assumptions are a homogeneous change in δ_a over the whole boundary layer with its height h, and that there is (theoretically) no other flux component.

$$\mathrm{IF} \overset{\text{Eq.3.5}}{=} \frac{F_C}{C_a \rho_a}(\delta_F - \delta_a) = h\frac{\mathrm{d}\delta_a}{\mathrm{d}t} \tag{3.6}$$

3.3.2.4 Random uncertainty estimation

We calculated an estimate for the random uncertainty of the measured (isotopologue) fluxes F_C based on the Mann and Lenschow (ML) model (Lenschow et al., 1993; Lenschow et al., 1994; Mann et al., 1994). This method assumes that the (in theory stationary and infinitely long) time series of w and C have a joint Gaussian probability density and the existence of an integral timescale $\mathfrak{T}_F$ (Lenschow et al., 1993). In general, $\mathfrak{T}_F$ is defined as $\mathfrak{T}_F := \int_0^\infty \rho(\tau)\,\mathrm{d}\tau$ with the autocorrelation function $\rho(\tau)$ of the flux F (see e.g. Saleska et al., 2012). The ML uncertainty estimate relates the variance $\sigma(F_C)$ of the measured flux F_C to this integral timescale $\mathfrak{T}_F$, the flux averaging period T, and the correlation coefficient[1] $r_{w,C}$ between the vertical wind velocity w and the mole fraction C:

$$\sigma_{\mathrm{ML}}(F_C) = F_C \sqrt{\frac{2\mathfrak{T}_F}{T}\,\frac{1 + r_{w,C}^2}{r_{w,C}^2}} \tag{3.7}$$

For our calculations, we estimate the integral timescale as $\mathfrak{T}_F = \int_0^{\tau_{\max}} \frac{R_{w,C}}{\overline{w'C'}}\,\mathrm{d}\tau$ as described by (LiCor Biosciences, 2016).[2]. Here, we set $\tau_{\max}$ to the integration time at which $R_{w,C}/\overline{w'C'}$ reaches $1/e$ to obtain an estimate for $\mathfrak{T}_f$ that is most consistent among different runs (LiCor Biosciences, 2016). We evaluate the ML uncertainties for the measured isotopic compositions of ET (equation 3.4) by propagating the uncertainties of the measured isotopologue fluxes, see appendix 3.9.1 for details.

1 The correlation coefficient between w and C is defined as $r_{w,C} = \overline{w'C'}\,/[\sigma(w)\,\sigma(C)]$.
2 With the cross correlation $R_{w,C}(t) := \int w(\tau)C(\tau + t)\,\mathrm{d}\tau$.

3.3.3 Eddy covariance water isotope measurements

3.3.3.1 Instrumentation

Water vapor isotope analyzer

We equipped the anemometer of our EC setup (cf. section 3.3.4.3) with an additional inlet to measure the water vapor mole fraction $C_{H2O,v}$ and its isotopic composition in both, δD and δ^{18}O, with a measurement frequency of 2 Hz. For these measurements we used a customized version of the water vapor isotope analyzer with enhanced performance (EP-WVIA, *Los Gatos Research. Inc.,San Jose, USA*) that was optimized by the manufacturer for high flow (HF) to take 2 Hz measurements (2 Hz-HF-WVIA, *Los Gatos Research. Inc.,San Jose, USA*). The measurement principle and the optical properties of the 2 Hz-HF-WVIA are the same as those of the slower analyzer (EP-WVIA, *Los Gatos Research. Inc.,San Jose, USA*), which is a laser-based cavity-enhanced absorption spectrometer in near infrared (Los Gatos Research Inc., 2013). Instruments of this type measure the isotopologue-specific rotational-vibrational absorption features of a molecule (Kerstel et al., 2008). For the EP-WVIA (and the 2 Hz-HF-WVIA), the wavelength is scanned from approximately 1.3889 μm to 1.3888 μm (Aemisegger et al., 2012) and the optical path length is enhanced up to 2500 m (Los Gatos Research Inc., 2013). This long path length is achieved by off-axis integrated-cavity output spectrometry that quantifies the individual isotopologue-mole fractions by measuring the time-integrated radiation intensity which is leaking out a high-finesse optical cavity (Aemisegger et al., 2012; Los Gatos Research Inc., 2013).

The customization for 2 Hz measurements included an updated version of the analyzers operating software and changes in the analyzers internal plumbing to achieve higher gas flow. In combination with an external dry scroll vacuum pump (XDS35i, *Edwards Vacuum, Crawley, UK*) we achieved a flow rate Φ of up to approximately 7 slpm. By adjusting an external throttle valve between the analyzer and the pump (Fig. 3.1), we regulated the analyzers flow rate Φ down to approximately 4.2 slpm. With a cell pressure of $p_{cell} \approx 40.2$ Torr and a cavity size of approximately 401 ml (Robert Provencal, Los Gatos Research Inc., personal communication by email), this yields a theoretical response time[1] $\tau_{theoretical}=V_{cell} * p_{cell}/\Phi$ of approximately 0.3 s.

Water vapor isotope calibration unit

To calibrate the δ value measurements of the 2 Hz-HF-WVIA, we used a customized version of the Los Gatos Water Vapor Isotope Standard Source (WVISS, *Los Gatos Research. Inc.*,San Jose, USA)[2]. In general, the WVISS produces water vapor with a constant isotopic composition (δD and δ^{18}O) at different water vapor mole fractions $C_{H2O,v}$ (Los Gatos

1 The theoretical response time $\tau_{theoretical} = p * V/\Phi$, can be derived from the (unrealistic) assumption that there is no mixing in the measurement cell.

2 The WVISS used in our experiments had an extended range unit that allows a two step dilution of the calibration gas, but during the measurements we did not make use of this feature. For a further description of specifications of the extended range unit and a technical drawing of the plumbing see also Los Gatos Research Inc. (2012).

Research Inc., 2012). The WVISS compresses and dries ambient air and uses a capillary-based nebulizer to completely evaporate a liquid water standard in a heated chamber at 75 °C, with a gas flow rate of below 1 slpm (see e.g. Aemisegger et al., 2012; Los Gatos Research Inc., 2012, for details). The water vapor mole fraction is regulated by a mass flow controller that adds 0-10 slpm of compressed and dry air to the heated chamber (Los Gatos Research Inc., 2012). For gas flow rates below 1 slpm, the WVISS can produce calibration gas with water vapor mole fractions between 5000 and 30 000 ppm. But, as our application required flow rates of approximately 5 slpm (larger than the analyzer's flow rate of 4.2 slpm), we could not set the dilution flow too low, yielding a maximum water vapor mole fraction of approximately 13 000 ppm. In cooperation with the manufacturer, we customized the WVISS for our measurements that required a large mole fraction range at flow rates of approximately 5 slpm. We further refer to this customized calibration unit as HF-WVISS. The customization of the WVISS included an increase of the mole fraction range even at flow rates of approximately 5 slpm and a reduction of the pressure drop when switching between the calibration unit and the analyzer's inlet. To obtain a higher mole fraction range at the required flow rate, we changed the internal nebulizer of the WVISS from its standard nebulizer (C50 nebulizer, customized for an operating temperature of 80°C, *Savillex, Eden Praire, USA*) to a nebulizer with higher liquid water flow rate (C100 nebulizer, customized for an operating temperature of 80°C, *Savillex, Eden Praire, USA*). This way we changed the mole fraction range of the HF-WVISS at a flow rate of approximately 5 slpm from approximately 5000 to 13 000 ppm (C50) to 10 000 to 26 000 ppm (C100). The mole fraction range was further slightly tuned by regulating the absolute pressure at the nebulizer's gas inlet between approximately 1.6 and 2 bar (the preset value is 2 bar). To achieve a similar flow rate during calibration as during the measurements and to minimize the pressure jump after switching from the analyzer to the HF-WVISS and vice versa, we equipped the HF-WVISS with an additional throttle valve, placed between the mass flow controller and the heated chamber.

3.3.3.2 Plumbing and tubing

The tubing of the isotope analyzer (2 Hz-HF-WVIA) and the calibration unit (HF-WVISS) is shown in Fig. 3.1. The main tube from the anemometer to the calibration unit (HF-WVISS) was a 58 m stainless steel coated Polytetrafluorethylen (PTFE) tube[1] with 6.5 mm inner diameter (TEF1H06, *indunorm, Neukirchen-Vluyn, Germany*). With a flow rate of $\Phi \approx 14$ slpm, the Re number was above 3000 for this part of the tubing. We heated the tube with a heating current of approximately 4 A that directly flowed through the tube's coating, resulting in a heating power of approximately 10 W/m (Gentsch et al., 2014). The heated tubing has been tested, used and described in detail by Gentsch et al. (2014) and proved to be suitable for water isotope measurements. The main tube was equipped with a 2 μm stainless steel filter (SS-4FW-2, *Swagelok*, Solon, USA). The filter was placed in a styrofoam-isolated box that was heated with a 12 W heating plate (*Thermo GmbH*, Ingolstadt, Germany) to avoid condensation at the pressure drop after the filter. The

1 The tubing material PTFE (teflon) was chosen due to its smaller retention times if compared to Synflex tubing (Sturm et al., 2009).

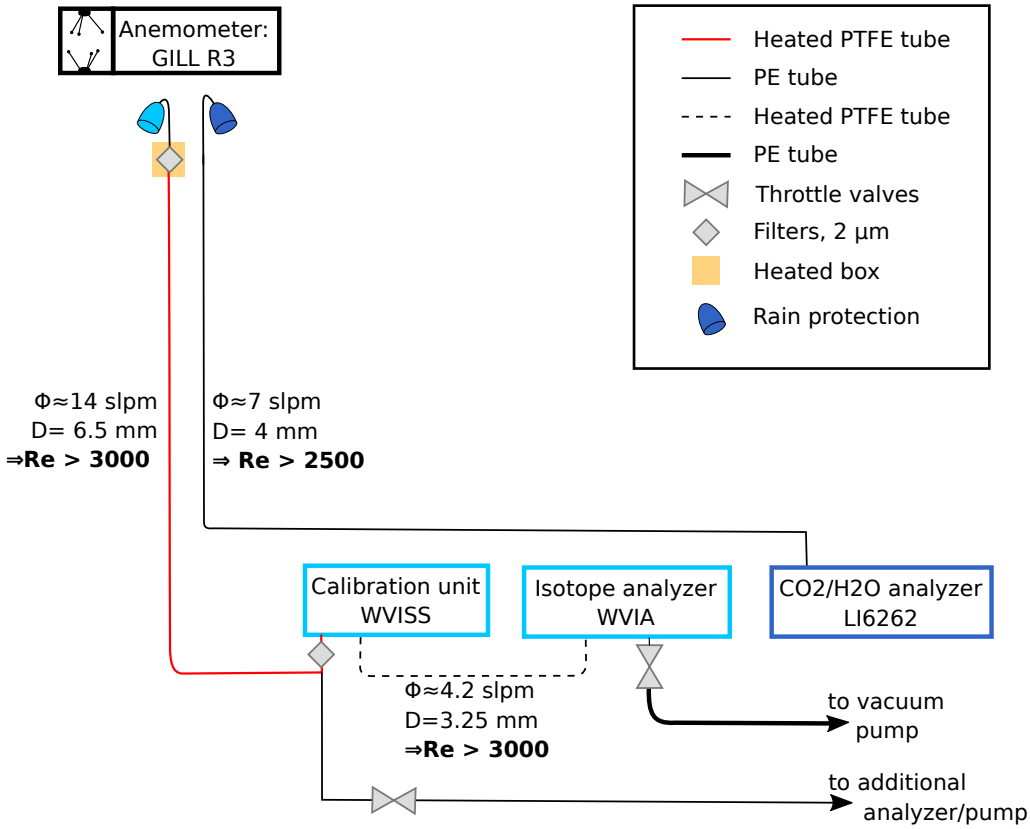

Figure 3.1: Experimental setup including material, diameters are inner diameters of all tubing used.

analyzers main tube was connected to a purge pump (Thomas VTE-6, *Gardner Denver*, Milwaukee,USA) and the calibration unit (HF-WVISS). The HF-WVISS automatically switched between the sample inlet and the calibration inlet (cf. Fig. 3.1). The material, diameters, and Re numbers for all tubes are shown in Fig. 3.1. The diameters of all tubes ahead of the 2 Hz-HF-WVIA were chosen to face the trade-off between 1) providing turbulent conditions while 2) ensuring an inlet pressure for the 2 Hz-HF-WVIA that allows the required flow rate[1].

3.3.3.3 Data structure and synchronization

We calibrated the 2 Hz-HF-WVIA hourly for approximately 10 minutes. Additionally, we excluded the half hourly time periods during which another analyzer - connected to the same gas tube - was calibrated (see Fig. 3.2). The calibration of the other analyzer caused pressure jumps at the 2 Hz-HF-WVIA inlet, that led to artifacts in the measured δ values. The 2 Hz-HF-WVIA took measurements of $C_{\mathrm{H2O,v}}$, δ^{18}O and δD with a frequency of 2 Hz

1 If the inlet pressure was too low, the analyzers automatic pressure control did not reach its setpoint (p_{cell}≈40 T) at the analyzer's flow rate of 4.2 slpm.

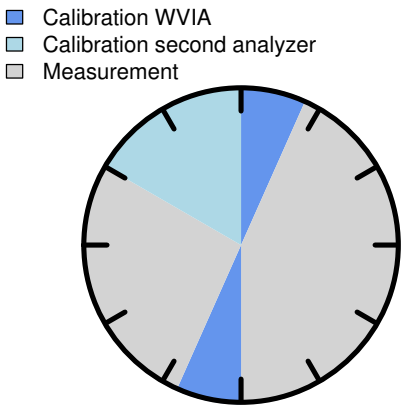

Figure 3.2: Hourly and half-hourly calibrations of two analyzers, that shared a common gas inlet, produced considerable data gaps.

and the data contained gaps related to calibration. The influence of the comparable low measurement frequency on the measured net fluxes is evaluated in section 3.4.2.1.

To synchronize the data stream of the 2 Hz-HF-WVIA with the anemometer's data, the measured data was sent to a PC via a serial connection. The timestamp of the PC was added to each data point using a visual software for measuring technology (ProfiLabExpert 4.0, *Abacom*, Germany). On the same PC, the 20 Hz data from the anemometer (and the LI-6262 gas analyzer, *LiCor Biosciences Inc.*, Lincoln, USA) was recorded with a self written program (in C) to convert the binary data stream to ASCII and add the PC's timestamp to each datapoint (Andre Ringeler, Bioclimatology, Goettingen). Before the anemometer data was sent to the PC via a serial connection, the analogue data from the LI-6262 was added to the anemometer data, the data was A/D-converted and send through a self-manufactured half duplex RS232 serial spy[1]. During data processing, we realized that the anemometer (and LI-6262) data was subject to a consistent delay of 10 s throughout the entire measurement period (yielding negative time lags between w and $C_{\mathrm{H2O,2\,Hz-HF-WVIA}}$) and corrected for this delay.

3.3.3.4 Calibration Strategy

Water vapor mole fraction calibration

To calibrate the water vapor mole fractions that were measured with the 2 Hz-HF-WVIA, we performed repeated manual measurements with a dew point generator (DPG) (LI-610, *Licor, Lincoln, USA*). All measurements with the DPG were performed in the analyzers 'low flow mode' with a flow rate of 0.1 to 0.2 slpm (we did not see any flow rate dependency of the measured mole fractions). The measurements with the DPG were performed on different days in the lab as well as in the field, based on the following procedure. The DPG was pre-cooled for at least 15 minutes and set up to produce a gas flow of 1.5 slpm. Afterwards, the DPG was connected to the inlet of the 2 Hz-HF-WVIA with an overblow

1 https://www.lammertbies.nl/comm/cable/RS-232-spy-monitor.html

and a completely open flow meter. We set the DPG to a temperature setpoint between 5 and 23 °C and waited for at least 20 min until the measured mole fraction stabilized. We repeated this measurement twice for each temperature setpoint with one measurement that was preceded by a higher temperature and one measurement that was preceded by a lower temperature. Based on this method, we estimated an upper and a lower limit for the respective measured mole fraction C_{meas}. The difference between higher and lower limit (typically between 50 to 200 ppm) was further used as error estimate for the respective measurement. We calculated C_{DPG}, the water vapor mole fraction produced by the DPG as a function of pressure and temperature by using the Magnus formula (Deutscher Wetterdienst, 1976). The temperature setpoint of the DPG had an accuracy of $\Delta T \approx 0.2K$. The ambient pressure was measured with a barometer, (GDH 12 AN, *GHM Greisinger*, Erolzheim, Germany) with an accuracy of $\Delta p \approx 1\,mbar$. The propagation of the error of the temperature setpoint of the DPG (that dominated over barometer errors) yields a relative accuracy of the water vapor mole fraction of the DPG of approximately 3×10^{-3}. The resulting linear relationship between C_{meas} and C_{DPG} was further used to calibrate C_{meas}.

δ value calibration

To calibrate the δ values, measured with the 2 Hz-HF-WVIA at the field site, we took hourly measurements with the calibration unit HF-WVISS (see section 3.3.3.1). As liquid water standard for this calibration, we used distilled tap water with δ values, that were measured with IRMS at the *Centre for Stable Isotope Research and Analysis* (*KOSI, Goettingen, Germany*) before and after the water tank of the HF-WVISS was refilled. During the measurement campaign, the HF-WVISS had to be adjusted to span the required mole fraction range. This involved using two different nebulizers C50/C100 within the HF-WVISS (cf. section 3.3.3.1). In winter the HF-WVISS was equipped with the C50 nebulizer and produced a mole fraction range of approximately 5000 to 13 000 ppm. In summer the C100 nebulizer was used to deliver a mole fraction range of approximately 10 000 to 26 000 ppm. For each calibration run, the HF-WVISS produced water with a constant δ value over the respective mole fraction range for summer/winter and the calibration cycle involved multiple switches between higher and lower mole fractions to reveal potential hysteresis effects. Each calibration run was initialized by 10 s of gas flow stabilization (cf. Los Gatos Research Inc., 2012) and took 7.5 minutes. Additionally, the calibration runs were preceded and followed by purging and stabilizing of the HF-WVISS for 30 and respectively 60 s to avoid clogging of the used nebulizer. The resulting data points were used to fit the analyzer's nonlinear mole fraction dependency $\delta_{\mathrm{H2Ocal}}(C_{\mathrm{raw}})$ by a polynomial of 8^{th} order $P(C_{\mathrm{raw}})$. During post-processing, all measured δ values were corrected with the following function for the non-linear C-dependency $P(C_{\mathrm{raw}})$ and offset δ_{Offset}:

$$\delta_{\mathrm{calibrated}} = \underbrace{\delta_{\mathrm{raw}} - P(C_{\mathrm{raw}})}_{\delta_{\mathrm{c-corrected}}} + \delta_{\mathrm{H2Ocal}} \tag{3.8}$$

Here, δ_{H2Ocal} is the δ value of the calibration water, $P(C_{\mathrm{raw}})$ is the hourly measured polynomial of 8^{th} order, and δ_{raw} and C_{raw} are the respective raw values. This calibration

procedure assumes the same mole fraction dependency for water with different δ values and is evaluated in chapter 3.4.1.

3.3.4 Additional Measurements

3.3.4.1 Measurements to evaluate the calibration strategy

We quantified the accuracy of the δ values measured with the 2 Hz-HF-WVIA by using the HF-WVISS to produce calibration gas with known isotopic compositions over a large mole fraction range. For this measurement, we used five liquid water standards (*Los Gatos Research. Inc*, San Jose, USA) in combination with the HF-WVISS. The used liquid water standards had $\delta^{18}O$ values ranging from approximately -2.7 to -19.5 ‰ and δD values from approximately -9.2 to -154 ‰, (measured with IRMS, see Table 3.2).

3.3.4.2 Isotope analysis of rain

We took rain samples for isotope analysis using three self-manufactured integrated rain samplers (Gröning et al., 2012). Each rain sampler was subsampled twice and replaced and dried biweekly. The respective subsamples of the isotopic composition of rain, integrated over approximately two weeks were analyzed with IRMS at the KOSI.

3.3.4.3 Eddy covariance (EC) and meteorological measurements

Experimental set-up

We used a sonic anemometer (Gill-R3, *Gill Instruments*, Lymington, UK) to measure the three-dimensional wind velocities and the sonic temperature in 44 m height above ground level with a sampling frequency of 20 Hz. The anemometer was placed on a meteorological tower on an extension arm in a north-northeast direction. In the vicinity of the anemometer, air was pumped through a 50 m long polyethylene (PE) intake tube with an inner diameter of 4 mm connected to a closed path gas analyzer (LI-6262, *LiCor Inc.*, Lincoln, USA), as shown in Fig. 3.1. This gas analyzer took measurements of the mole fractions of CO_2 and H_2O_v with a data acquisition rate of 20 Hz and an effective measurement frequency of approximately 3-4 Hz (due to the analyzers cell turnover). We used the 20 Hz raw data, to calculate the eddy flux densities of CO_2, H_2O_v, momentum, latent and sensible heat with the EC method.

Besides the EC setup, we measured standard meteorological parameters such as air temperature and relative humidity with a temperature and relative humidity sensor (HMP45D, *Vaisala*, Helsinki, Finland), long- and shortwave up- and downwelling radiation with a four component net radiometer (CNR1, *Kipp&Zonen B.V.*, Delft, The Netherlands).

	$\delta^{18}O$ [‰]	δD [‰]
Standard 1	-2.69	-9.2
Standard 2	-7.94	-51.6
Standard 3	-13.39	-97.3
Standard 4	-16.24	-123.7
Standard 5	-19.49	-154.0

Table 3.2: Five liquid water standards with different isotopic compositions ($\delta^{18}O$ and δD) were used to determine the analyzer's accuracy. All δ values are given on VSMOW scale.

Additionally, we measured precipitation above the canopy with a tipping bucket rain gauge (*Thies Clima*, Goettingen, Germany) as well as soil temperature and -moisture using moisture sensors (ML-2X, *Delta-T Devices Ltd.*, Cambridge, UK) in different depths. For more information about the instrumental setup see Anthoni et al. (2004).

Raw data processing

We used the open source EddyPro® Eddy-Covariance software, version 6.2.0 (LiCor Biosciences, 2016) to calculate net water vapor fluxes, averaged over an interval of 30 or 60 minutes. During data processing with EddyPro®, we used block averaging (for Reynolds decomposition) and double rotation (to rotate the horizontal wind component into the mean wind direction). We chose an automatic time lag optimization method to calculate time lags that occurred due to the horizontal separation of the sonic anemometer and the gas intake of the LI-6262 as well as due to the 50 m long tube. This method calculates plausibility windows as a function of relative humidity and applies a cross-covariance maximization within these plausibility windows (LiCor Biosciences, 2016). We applied this method for ten relative humidity classes. We used the procedure of Horst et al. (2009) to correct for additional effects of instrument separation (crosswind and vertical wind direction). We used the WPL correction to compensate (Webb et al., 1980) for density effects, and the Schotanus correction (Schotanus et al., 1983), which corrects the measured sensible heat flux for the sonic temperature's humidity dependency. Spikes were removed following the procedure of Vickers et al. (1997).

We set up the flux calculations to correct high-pass filtering effects on turbulent fluxes following Moncrieff et al. (2005) and to correct low-pass filtering effects according to the method suggested by Ibrom et al. (2007).

Quantification of effects on turbulent fluxes due to reduced measuring frequencies and gappy data structure

We used the standard EC measurements with the LI-6262 gas analyzer, as a reference dataset for our measurements with the 2 Hz-HF-WVIA. The two different gas analyzers record data with a different sampling frequency of 20 Hz (LI-6262) and 2 Hz (2 Hz-HF-WVIA). To evaluate the effects of reduced measurement frequency on the turbulent fluxes, we reduced the temporal resolution of the standard EC dataset by averaging the 20 Hz data down to 2 Hz. Afterwards, the same raw data processing settings were applied to the 20 Hz and the 2 Hz dataset.

Additionally, the 2 Hz-HF-WVIA dataset contains systematic data gaps due to frequent calibration (cf. Fig. 3.2). We studied the effect of these data gaps on the calculated turbulent fluxes by using a dataset with artificially produced data gaps. For this, we replaced measured values with block-wise occurring missing values (based on the 2 Hz EC dataset described above). This newly created data was then used to evaluate for which raw data processing settings the data gaps had a systemic impact on the measured fluxes. In detail, we used different averaging times of 20, 30 and 60 minutes. Additionally, we increased the maximum number of missing values to be 40 % to allow flux calculations also for datasets with large gaps.

3.4 Results and discussion

3.4.1 Evaluation of the setup

3.4.1.1 Precision (Allan deviation)

We evaluated the precision of the 2 Hz-HF-WVIA by calculating the Allan deviation (Werle et al., 1993) based on a 52 min long nighttime measurement at a water vapor mole fraction of approximately 10 000 ppm in the field. The measured Allan deviation at an averaging time of $\tau = 0.5\,s$ was approximately 0.45 ‰ for δ^{18}O and below 1.3 ‰ for δD. Longer averaging times reduced the measured Allan deviation with $\tau^{-1/2}$ (Fig. 3.3) as expected for white frequency noise (International Radio Consultative Committee, 1986). The measured Allan deviations are dominated by white frequency noise until an averaging period of approximately 500 s for δ^{18}O, and 300 s for δD. At these averaging times, the Allan deviations reach their minima at approximately 0.02 ‰ for δ^{18}O and 0.08 ‰ for δD. In general, the measured Allan deviation of the 2 Hz-HF-WVIA is comparable to the values reported for different (slow) versions of the WVIA (Aemisegger et al., 2012; Sturm et al., 2009). Based on lab measurements, these authors report minimal Allan deviations that are similar to our measurements for δ^{18}O, but by a factor between 1.1 to 4 smaller than in our measurement for δD. The Allan deviations of the 2 Hz-HF-WVIA under field conditions are within the range of IRMS measurements of liquid water samples (including sample preparation and handling) that is approximately 0.5 to 1 ‰ for δD and 0.024 to 0.1 ‰ for δ^{18}O (Sturm et al., 2009).

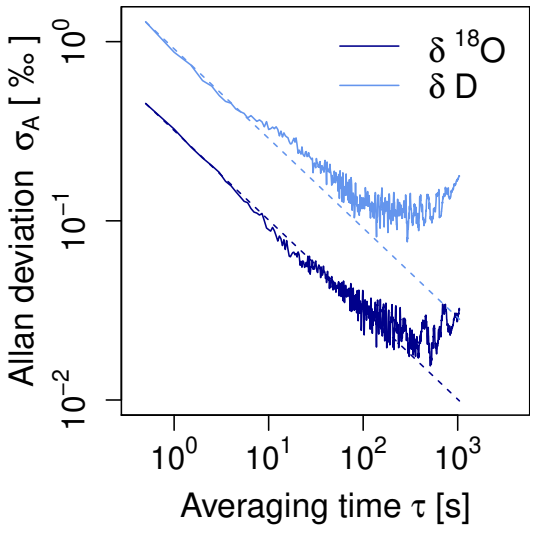

	δD [‰]	δ^{18}O [‰]
σ_A (0.5 s)	1.3	0.45
σ_A (1 s)	0.87	0.32
σ_A (5 s)	0.41	0.14
σ_A (15 s)	0.30	0.07
σ_A (15 min)	0.15	0.03
σ_A ($\tau_{\min}$)	0.08	0.02

Figure 3.3: The measured Allan deviations have their minima at $\tau_{\min} \approx 290\,s$ for δD and $\tau_{\min} \approx 500\,s$ for δ^{18}O.

3.4.1.2 Evaluation of the calibration strategy

The calibration strategy described in section 3.3.3.4 is based on the following relationships:

- A nonlinear relationship between measured δ values and mole fractions that is persistent for different δ values (Fig. 3.4).
- A linear relationship with a slope of one between calibrated δ values and mole fraction corrected δ values $\delta_{\mathrm{c-corrected}}$ (Fig. 3.5).
- A linear relationship between measured and real water vapor mole fraction $C_{\mathrm{H2O,v}}$ (Fig. 3.15).

The isotopic compositions measured with the 2 Hz-HF-WVIA showed a mole fraction dependency that spans a range of about 3.6 ‰ for δ^{18}O and about 12.7 ‰ for δD over a mole fraction range from approximately 5000 to 26 000 ppm (Fig. 3.4). For different δ values, this mole fraction dependency was only shifted by an offset (Fig. 3.4). We corrected this mole fraction dependency by a nonlinear fit of 8^{th} order, fitted separately for the high/low mole fraction range of the used nebulizer between 5000 to 13 000 ppm and 10 000 to 26 000 ppm (see section 3.3.3.4).

The mole fraction-corrected δ values are linearly related to the real (IRMS-measured) δ values with a slope of one (Fig. 3.5). The respective linear regressions have R^2-values above 0.999 for both, δ^{18}O and δD. The 1 σ standard deviation of the residuals from this linear calibration curve (in our case with a slope of one) can be used to quantify an instrument's linearity and potential accuracy (Tuzson et al., 2008). Based on our measurements with five different standards over mole fraction ranges from 4500 to 27500 ppm, the so defined potential accuracy of the 2 Hz HF WVIA is approximately 0.16 ‰ for δ^{18}O and 0.50 ‰ for

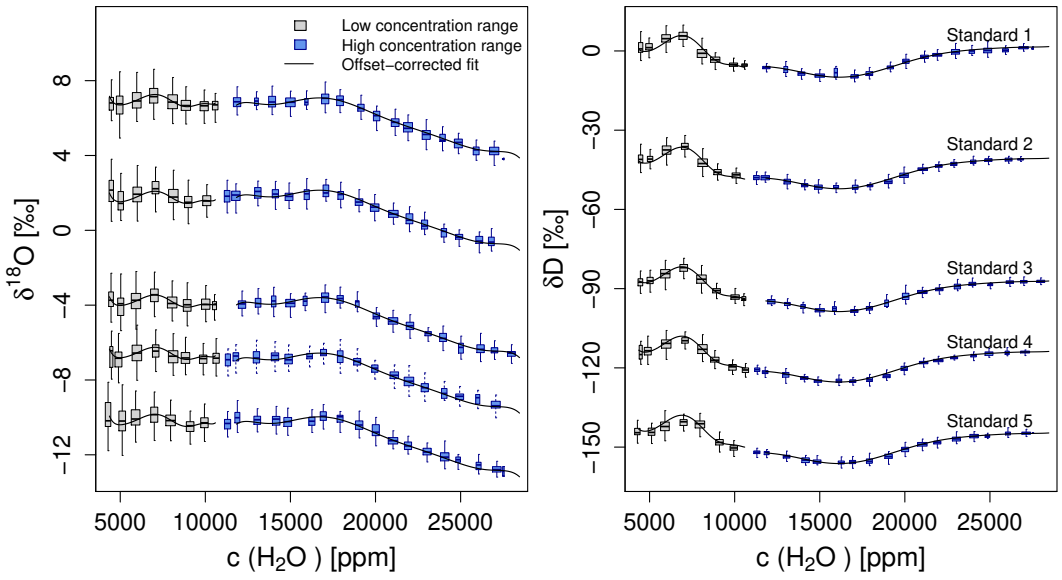

Figure 3.4: The measured (raw) isotopic compositions δ^{18}O and δD depend strongly on (raw) water vapor mole fraction $C_{\mathrm{H2O,v}}$.

δD. Thus, the measured potential accuracy is similar to the accuracy of an older version of the WVIA (without high-flow and high frequency optimization) that has been estimated to be around 0.14 to 0.20 ‰ for δ^{18}O and around 0.44 to 0.73 ‰ for δD (Sturm et al., 2009), based on lab measurements with five standards.

The dew point generator's water vapor mole fraction was a linear and temporarily constant function of the analyzers uncalibrated water vapor mole fraction (Fig. 3.15). This linear relationship is based on a York-type fit that includes error estimates for both axes (Wehr et al., 2017; York, 1968). The slope of this linear fit is 1.12 ± 0.01 and its intercept is -270 ± 95 ppm. The resulting potential accuracy of the mole fraction calibration (defined as the sum[1] of the accuracy of the dew point generator - cf. section 3.3.3.4 - and the 95 % confidence interval of the linear fit) is between 120 and 250 ppm for water vapor mole fractions between 4000 and 30 000 ppm.

One of the disadvantages of the calibration strategy is the need of exchanging not only the calibration water but also the internal nebulizer in the calibration unit when the water vapor mole fraction exceeded the calibration range. This produces some additional maintenance effort as one needs to plan field trips based on changes in both, the measured water vapor mole fraction and the calibration range. Further customization of the WVISS might reduce this effort. Another principle disadvantage of the calibration strategy is, that only one liquid water standard is used for automatic calibration and thus only a

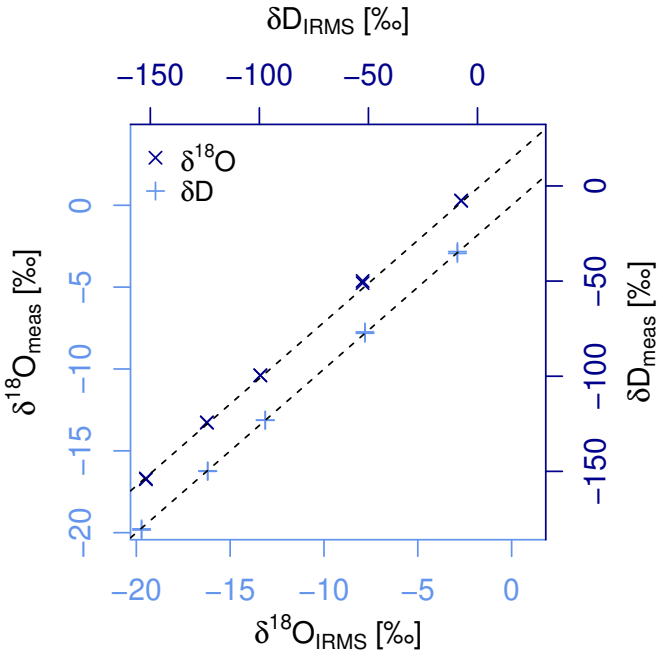

Figure 3.5: After correcting for the mole fraction dependency, the measured δ values are linearly related to the IRMS-measured (real) δ values. The lines are linear regressions with a fixed slope of one. These regressions have coefficients of determination R^2 above 0.999.

1 Here we used a sum to propagate the error as a worst case scenario of a constant offset of all mole fractions calculated with the dew point generator in addition to the random uncertainties captured in the fit.

one-point offset correction is applied. However, the test measurements with five water standards show that this approach yields potential accuracies of 0.16 and 0.50 ‰ for δ^{18}O and δD respectively, which is within the interquartile range of a worldwide inter-laboratory comparison of 120 different analyzers (IRMS and laser spectrometers) (Wassenaar et al., 2012). Based on four different water standards, this inter-laboratory comparison found the average interquartile range of all measurements (after outlier removal) to be approximately 0.18 ‰ for δ^{18}O and 1.3 ‰ for δD (Wassenaar et al., 2012).

3.4.1.3 High-frequency dampening (tubing effects)

Tubing effects become visible in the high frequency domain of the energy spectrum[1] $S_{xx}(f) := |\mathcal{F}[x(t)]|^2$ of a variable $x(t)$. More explicitly, they become visible in a deviation of the respective energy spectrum from the expected slope of $-2/3$ in the inertial sub range (Kaimal et al., 1994). For both analyzers, the 2 Hz-HF-WVIA and the LI-6262, there are considerable deviations from the slope of $-2/3$, whereas the sonic temperature spectrum follows this slope (see Fig. 3.6). These tubing effects depend strongly on relative humidity, hence the deviation from the sonic temperature spectrum appears earlier for higher relative humidity (see Fig. 3.6). Additionally, instrument noise and aliasing becomes visible as a rise in the high frequency end of the energy spectrum. In the normalized energy spectrum (Fig. 3.6), this effect is stronger for higher relative humidity (e.g. at night) because they correspond to smaller fluxes.

In general, the energy spectrum of the 2 Hz-HF-WVIA is very similar to the energy spectrum of the LI-6262 (Fig. 3.6). Over all humidity classes, the high-frequency dampening occurred later for the 2 Hz-HF-WVIA than for the LI-6262. This indicates that tubing effects have a stronger influence for the LI-6262 which had a non-heated inlet tube. Also the rise of the energy spectrum at the high-frequency end of the spectrum is stronger for the LI-6262 than for the 2 Hz-HF-WVIA. Thus, we conclude that with respect to the energy spectrum the 2 Hz-HF-WVIA does perform comparable or slightly better than the LI-6262 that is routinely used to measure water and CO_2 fluxes with the eddy covariance method at this site.

Here we use the isotopologue mole fractions C^{161}, C^{181} and C^{261} separately to calculate the fluxes for the different isotopologues F^{161}, F^{181} and F^{261}. These isotopologue fluxes are further used to calculate the δD and δ^{18}O composition of evapotranspiration using Eq. 3.4. The energy spectra for the three isotopologues show the same high-frequency dampening (Fig. 3.6), indicating that there are no isotope selective tubing effects (such as condensation). The spectral energies for C^{161} and C^{181} are particularly similar, whereas for C^{162} the energy spectrum shows a stronger rise at the high-frequency end of the spectrum. This might reflect that instrument noise is relatively stronger for δD than for δ^{18}O. A generally more noisy signal of δD measurements and potential tubing effects that only affect deuterium were also discussed by Griffis et al. (2010), who measured the energy spectrum based on 3 h of measurements above a corn canopy. For their measurements,

1 The energy spectrum can also be defined as $S_{xx}(f) := \mathcal{F}[R_{x,x}]$ with the auto cross covariance $R_{x,x} := \int x^*(\tau)\, x(\tau + t)\, \mathrm{d}\tau$ (Kaimal et al., 1994). By using the cross correlation theorem it can be shown that $S_{xx}(f) = |\mathcal{F}[x(t)]|^2$, a definition given by (Stull, 1988).

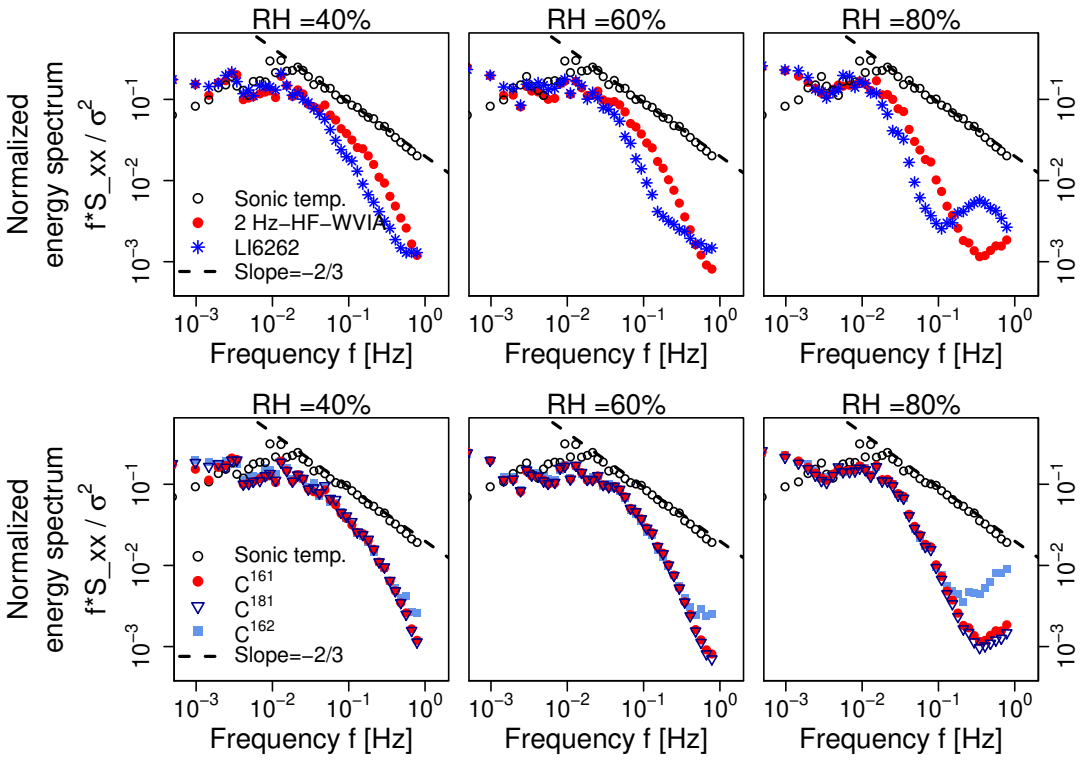

Figure 3.6: Ensemble averaged normalized energy spectra $f \times S_{xx}/\sigma^2$ for temperature in combination with the spectra of the mole fractions of water vapor measured with two different analyzers (top panels), and different isotopologues of water (bottom panels). The horizontally aligned panels show different relative humidities RH. For temperature, $f \times S_{xx}/\sigma^2$ followed the theoretical slope of -2/3 in the inertial subrange (open circles, all panels). The spectra of water vapor mole fractions measured with the 2 Hz-HF-WVIA showed less pronounced tube effects than the LI-6262, as visible in the deviation from the theoretical slope of -2/3 (top panel). For the different isotopologues C^{klm}, all measured with the 2 Hz-HF-WVIA, tube effects were similar but noise had a stronger influence on the less prevalent isotopologues (bottom panel).

the resulting energy spectrum for C^{162} showed a generally higher variability than for the other isotopologues (Griffis et al., 2010). For the energy spectrum obtained during our measurement campaign (Fig. 3.6), such a higher variability in C^{162} did not occur in general, but we measured a rise of energy spectrum at the high-frequency end that we associate with noise.

Further, the cospectra between the respective mole fractions (e.g. C^{klm}) and the vertical wind velocity w can give information about the impact of tube effects on the measured fluxes. The obtained ensemble averaged[1] cospectra $\mathrm{cosp}_{w',C'}$ (plotted in Fig. 3.7 as a function of the non-dimensional frequency f_n) follow the expected slope of -4/3 in the

1 The ensemble averaging was performed by a flux calculation software (EddyPro, *Licor, Lincoln, USA*), see e.g. (LiCor Biosciences, 2016) for details.

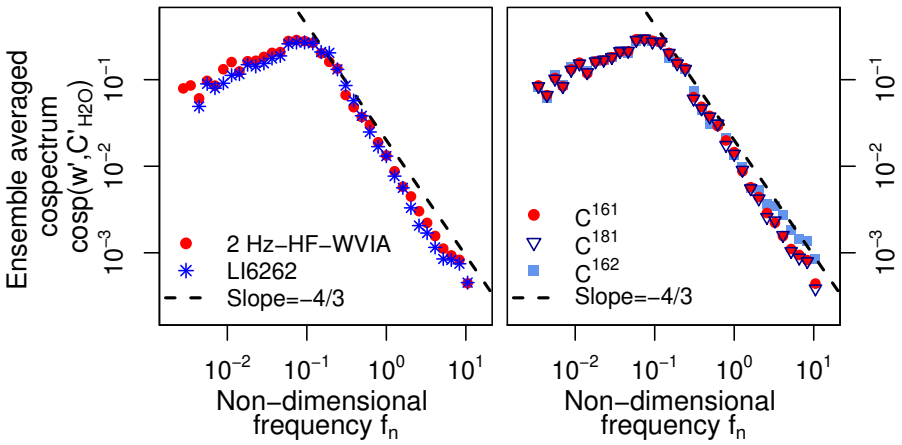

Figure 3.7: The ensemble averaged cospectra $\mathrm{cosp}(w',C'_{\mathrm{H2O}})$ in case of unstable stratification, plotted here as a function of the non-dimensional frequency $f_n = fh_m/\overline{u}$ (with the measurement height h_m and the mean horizontal wind velocity $\overline{u}$) are similar for all isotopologues (left panel) and for both analyzers (right panel).

inertial subrange for the three different isotopologues and for both analyzers. In particular, the obtained cospectra are very similar for the three different isotopologues, indicating that there are no isotopologue selective tubing effects on the measurement of the isotopologue fluxes. For C^{162} the values slightly rise in the high-frequency range, which might be related to the obtained rise in the corresponding energy spectra at the high-frequency end (Fig. 3.6) discussed above.

3.4.2 Measured fluxes and isofluxes

3.4.2.1 Influence of slow measurement frequency and gappy data structure

We analyzed how much the technical limitations of our setup (the comparably slow measurement frequency and the gappy data structure - cf. section 3.3.3.3) influenced the calculated net fluxes. For this purpose, we used the LI-6262 measurements and produced two artificial datasets with firstly a reduced measurement frequency of 2 Hz, and secondly the same gappy data structure in addition to the reduced measurement frequency of 2 Hz. More than 98 % of the variability of the measured EC fluxes based on the slow (2 Hz) dataset is directly linked to the EC fluxes based on the fast (20 Hz) data (the R^2 of the 1:1 line is above 0.98). The good agreement between these datasets goes in line with the fact that for the LI-6262 gas analyzer 20 Hz is only the data acquisition frequency, whereas its real measurement frequency is about 3-4 Hz (cf. section 3.3.4.3). Deviations from the 1:1 line occurred preferentially towards an underestimation of the fluxes calculated with the 2 Hz data set (Fig. 3.8). However, the mean and the median of the difference in fluxes calculated with the fast (20 Hz) and the slow (2 Hz) dataset are only 0.1 and respectively 0.03 $\mathrm{mmol\,m^{-2}s^{-1}}$. When artificial data gaps are added to the 2 Hz LI-6262 data, still more than 88 % of the variability of the measured EC fluxes is directly linked to the EC fluxes based on the fast (20 Hz) data. Deviations from the 1:1 line are considerably larger for this dataset. The standard deviation of the difference between the fast (20 Hz)

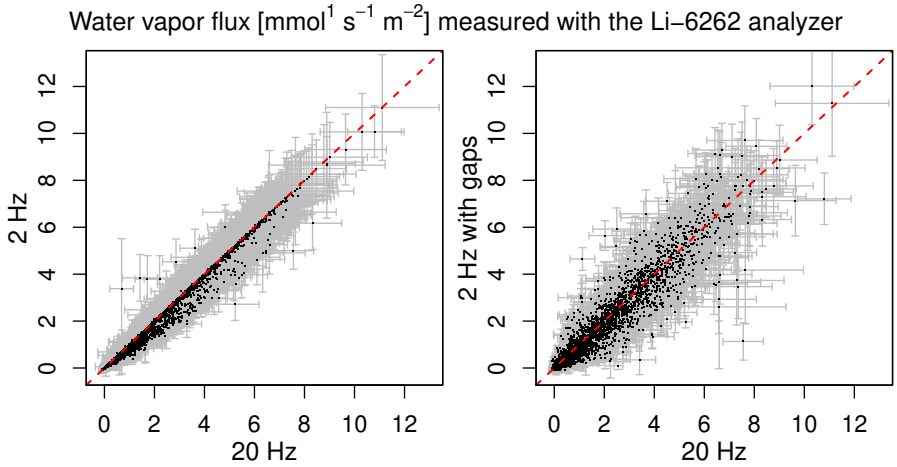

Figure 3.8: Influence of reduced measurement frequency (left panel) and gappy data structure (right panel) on the calculated net water vapor fluxes. The red line is the 1:1-line and errorbars are the respective ML-uncertainties.

and the gappy slow data (2 Hz-gappy) is 0.5 mmol $m^{-2}s^{-1}$. The mean and the median of this difference is 0.07 and 0.03 mmol $m^{-2}s^{-1}$, respectively. Thus, the data gaps introduce deviations from the standard EC-calculations, but they do not lead to an additional bias, even if approximately 40 % of the data is removed.

3.4.2.2 Net water vapor fluxes

The net water flux measured with the 2 Hz-HF-WVIA correlates strongly with the net water fluxes measured with the LI-6262 gas analyzer (Fig. 3.9). The coefficient of determination R^2 of a York-type fit (Wehr et al., 2017; York, 1968), which includes the uncertainties in both variables, is 0.9. The slope of this regression is approximately 0.81, indicating a consistent underestimation of the net water vapor flux measured with the 2 Hz-HF-WVIA. Such a strong underestimation did not occur in the study of Griffis et al. (2010), with slopes of 0.99 and 1.06 and R^2 values above 0.997 for the comparison of the measured net water fluxes of an isotope analyzer to two different infrared gas analyzers (IRGA). Also, measurements with the standard version of the WVIA that has an effective measurement frequency of 0.2 Hz (Good et al., 2012) did not report such a strong underestimation. In this study, the authors used a different high-frequency correction, the mentioned equation is the same as in the low pass filtering correction according to (Moncrieff et al., 1997a), which is normally not recommended for long inlet tubes.[1]

For our dataset, the observed underestimation of the net water flux depends strongly on the applied high-frequency spectral correction. If we use the analytical high frequency correction of tube effects according to Moncrieff et al. (1997a), instead of the standard method for long tubes following Ibrom et al. (2007), the fluxes measured with the two

1 The above mentioned study by Griffis et al. (2010) does not expatiate the used high frequency correction method.

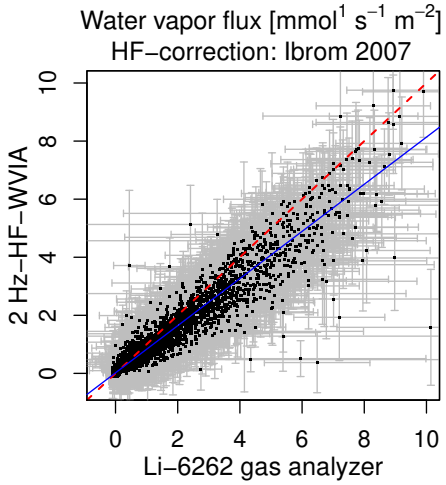

Figure 3.9: Hourly evaluated net fluxes (black points) as measured with the two different analyzers (2 Hz-HF-WVIA, and LI-6262) and their respective ML-uncertainties in gray. The net water vapor flux measured with the 2 Hz-HF-WVIA, underestimated the net water vapor flux measured by the LI-6262 as seen in the deviation from the York-type fit (blue line) with a slope of approximately 0.81 and $R^2 \approx 0.9$ from the 1:1 line (red, dashed line). This underestimation depends on the applied high-frequency correction, here: according to (Ibrom et al., 2007), see text for details.

different analyzers agree better (Fig. 3.14). With this high frequency correction method, the slope of a York-type fit between the net water vapor flux measured with the 2 Hz-HF-WVIA and the LI-6262 is 0.94, with an coefficient of determination R^2 of 0.92. This indicates underestimation of only 6 % by the 2 Hz-HF-WVIA. The method according to Ibrom et al. (2007) is based on a comparison of the spectra of sonic temperature T_s and mole fraction C. The resulting correction factor is applied directly to the measured flux. In the low pass filter correction method according to Moncrieff et al. (1997a) on the other hand, a frequency-dependent correction factor is applied to the cospectrum of C and w. Thus, the observed dependency of the agreement between the two analyzers on the applied high-frequency correction method can be related to the fact that the analyzer's spectra are much more different than the measured cospectra (Fig. 3.6 and 3.7). However, as the spectra and cospectra for the different isotopologues are so similar (Fig. 3.6 and 3.7), the underestimation of the net water fluxes is the same for the three different isotopologues (each scaled with the corresponding abundance). Thus, the underestimation will cancel out when we calculate the isotopic composition of ET, by dividing two isotopologue fluxes by each other (Eq. 3.4). To avoid additional bias that could be added by the data-driven high-frequency correction method according to Ibrom et al. (2007), we further use the spectra calculated with the (simpler) high-frequency spectral correction method of Moncrieff et al. (1997a).

3.4.2.3 Uncertainty of δ_{ET}

The propagated ML-uncertainties, as a function of the magnitude of ET are shown in Fig. 3.10. As expected from Eq. 3.9 in the appendix, the uncertainties of $\delta^{18}O_{ET}$ and δD_{ET} were typically larger when ET is small, because if the random uncertainties do not approach 0 in the same way as fluxes approach 0, the corresponding relative uncertainties increase with decreasing fluxes (Eq. 3.9).[1] For all daytime fluxes above 2 mmol m^{-2}s^{-}1,

1 In general, this is only true, if a) the individual uncertainties σ of the individual eddy fluxes F_i do not approximate 0 in the same way and b) the flux ratio itself does not approximate 0.

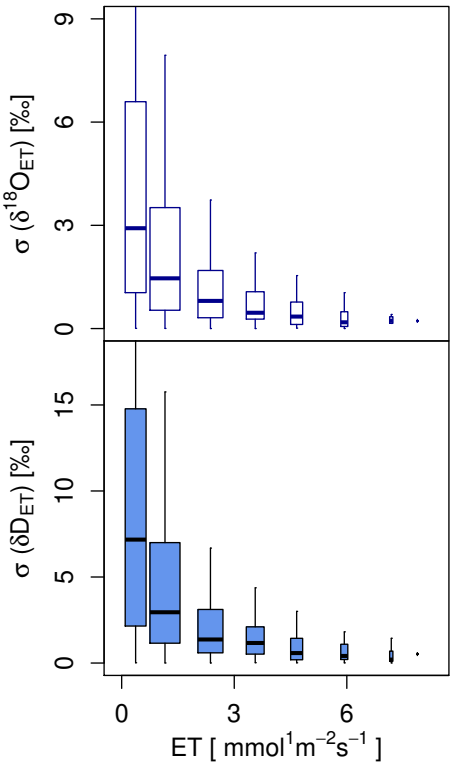

Figure 3.10: Box-whiskers plots, indicating a decrease of the propagated uncertainties σ of the (hourly measured) isotopic composition of ET (δ_{ET}) with increasing ET. Only daytime values are included in this plot.

the median of the propagated uncertainties is approximately 0.5 and 1 ‰ for $\delta^{18}O$ and δD, respectively. Overall, the obtained uncertainties of $\delta^{18}O_{ET}$ are comparable to different (averaged) uncertainty estimates[1] observed by other authors with flux gradient approaches. There estimates reach from approximately 1.4 ‰ above a semi-arid savanna (Good et al., 2012) as well as based on a simulated flux gradient experiment for typical daytime conditions (Lee et al., 2007), to an average uncertainty of 8 ‰ over 6 sunny days above a temperate grassland (Hu et al., 2014). For δD, an average uncertainty of the flux gradient measurements of approximately 6 ‰ was estimated above a semi-arid savanna (Good et al., 2012).

3.4.2.4 Seasonal variability of δ_{ET}

In Figure 3.11, the isotopic composition of ET (δ_{ET}) is shown on diurnal timescale for both isotopologues in combination with potential drivers of δ_{ET} such as temperature T, relative humidity RH, vapor pressure deficit VPD and the amount of rain. The flux-weighted diurnal average of the isotopic composition of ET ($\delta^{18}O_{ET}$ and δD_{ET}) varied from approximately -19 to 0 ‰ for $\delta^{18}O$ and from approximately -140 to -25 ‰ for δD (Fig. 3.11). Before

1 The quoted authors use different estimates of the uncertainty of flux gradient measurements, such as a simulated flux gradient measurement with a dew point generator under typical daytime conditions (Lee et al., 2007), standard deviations from 4 minute data to hourly means (Hu et al., 2014) and standard uncertainty estimation of the underlying linear regression (Good et al., 2012).

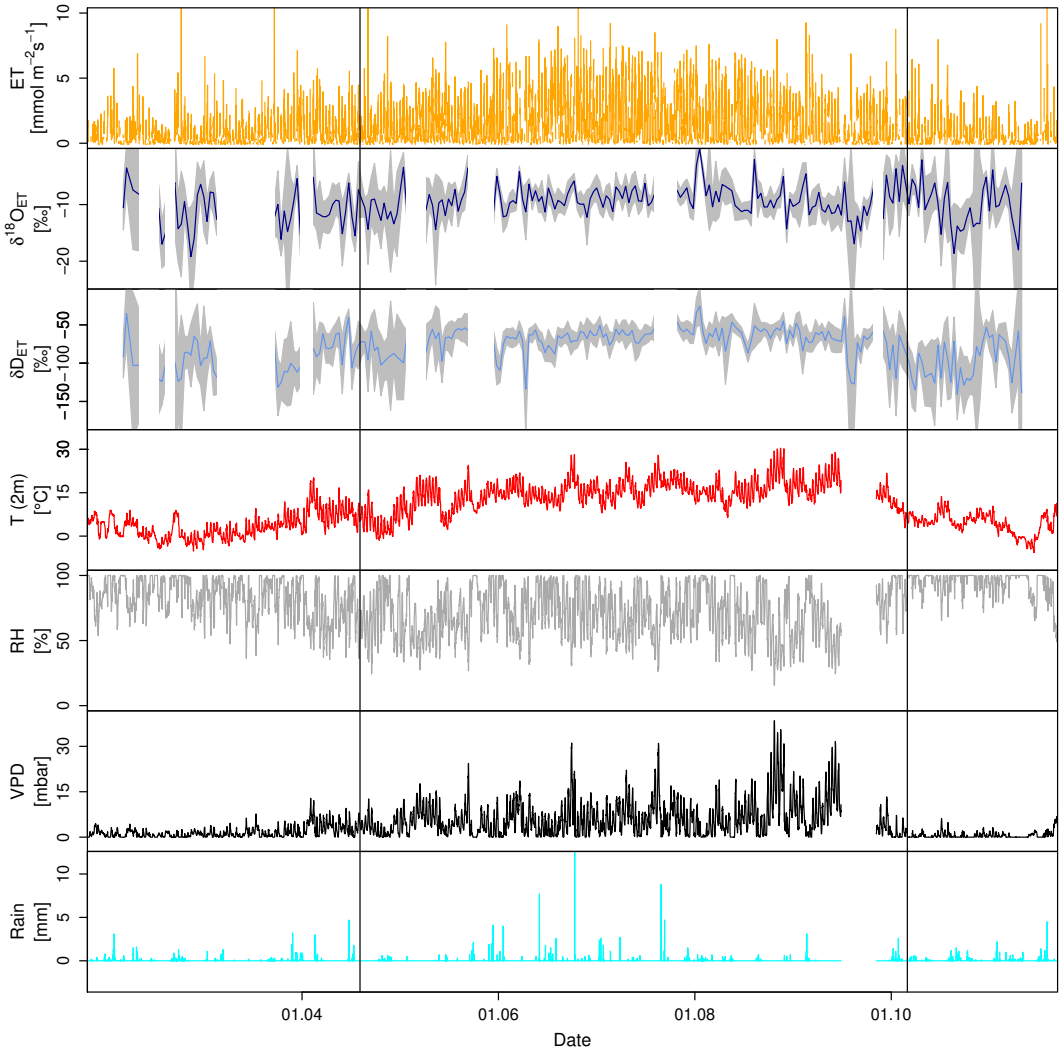

Figure 3.11: Time series of evapotranspiration (ET) and its isotopic composition $\delta^{18}O_{ET}$ and δD_{ET} in combination with meteorological measurements of temperature in 2 m height [T(2m)], relative humidity (RH), vapor pressure deficit (VPD), and the amount of rain. The vertical lines mark the times of the beginning of leaf unfolding on 19. April 2016 and the beginning of leaf coloring on 6. October 2016. All time series except $\delta^{18}O_{ET}$ and δD_{ET} are shown here on 30 min timescale, whereas for $\delta^{18}O_{ET}$ and δD_{ET} the flux weighted diurnal averages are shown here in combination with their uncertainties (shaded in grey).

Table 3.3: Monthly averaged quantities. For δ_{ET} the averages are flux-weighted.

Month	C_{H2O} [ppm]	$\delta^{18}O_v$ [‰]	δD_v [‰]	ET $\left[\frac{mmol}{m^2 s}\right]$	$\delta^{18}O_{ET}$ [‰]	δD_{ET} [‰]
February	6712	-20.9	-159	0.6	-12.0 ± 1.4	-99 ± 11
March	6859	-21.0	-160	1.2	-10.9 ± 1.3	-105 ± 10
April	7566	-18.4	-136	1.3	-11.3 ± 0.7	-80 ± 5
May	11717	-16.6	-122	1.4	-9.8 ± 0.8	-67 ± 5
June	16112	-16.2	-122	2.4	-9.3 ± 0.4	-70 ± 2
July	15654	-15.2	-114	2.4	-8.7 ± 0.4	-62 ± 3
August	15370	-15.9	-117	2.1	-9.3 ± 0.5	-61 ± 2
September	15424	-16.4	-120	1.3	-10.6 ± 0.6	-69 ± 3
October	10894	-21.0	-152	1.0	-9.2 ± 0.8	-96 ± 6
November	7257	-22.4	-162	0.6	-8.5 ± 1.8	-75 ± 11

leaf unfolding and after leaf coloring, when ET is comparably small, the uncertainties of $\delta^{18}O_{ET}$ and δD_{ET} were typically larger, as ET was small (cf. section 3.4.2.3). On a monthly timescale, the flux-weighted mean of $\delta^{18}O_{ET}$ and δD_{ET} spanned a range of about -3.5 ‰ for $\delta^{18}O_{ET}$ and about −40 ‰ for δD (Table 3.3). Compared to the variability of the isotopic composition of ambient δ values, the variability of δ_{ET} is a factor of 2 smaller in the case of $\delta^{18}O$, but only a factor of approximately 1.2 smaller for δD (Table 3.3).

3.4.2.5 Diurnal variability of δ_{ET}

The mean diurnal cycles of the isotopic compositions of ET ($\delta^{18}O_{ET}$ and δD_{ET}) are shown in Fig. 3.12 for spring (March to May), summer (from June to August) and autumn (September to November). These diurnal cycles were only evaluated for daytime (7h-21h GMT+1), as the uncertainties rise with decreasing ET. For both delta values, the isotopic composition of ET generally rose throughout the day. This rise throughout the day is expected for a water source that enriches during the course of the day and thus for non-steady state conditions. Such a rise of δ_{ET} was found for all mean diurnal cycles shown in Fig. 3.12, except for δD_{ET} in summer that shows a rather constant behaviour, indicating that during this time, equilibrium conditions were reached for δD, but not yet for $\delta^{18}O$.

To quantify potential effects of ET on the isotopic composition of the atmosphere, we calculated isoforcing according to Eq. 3.5, that can be interpreted as the rate of change of the atmospheric δ value multiplied by the boundary layer height h (see Eq. 3.6). For this calculation, we used the data points measured at 44 m as atmospheric composition δ_a in Eq. 3.6. All calculated hourly isoforcing values were positive, corresponding to an enrichment of the atmospheric δ value due to ET. This is also true on monthly timescale, with $\delta_{ET} > \delta_v$ (Table 3.3). The mean diurnal cycles of isoforcing are dominated by the mean diurnal cycle of ET and have diurnal maxima of 0.08 and 0.6 ‰ $m^{-2}s^{-1}$, for $\delta^{18}O$

and δD respectively (Fig. 3.12), comparable to the results found by other authors (Hu et al., 2014; Lee et al., 2007; Welp et al., 2008).

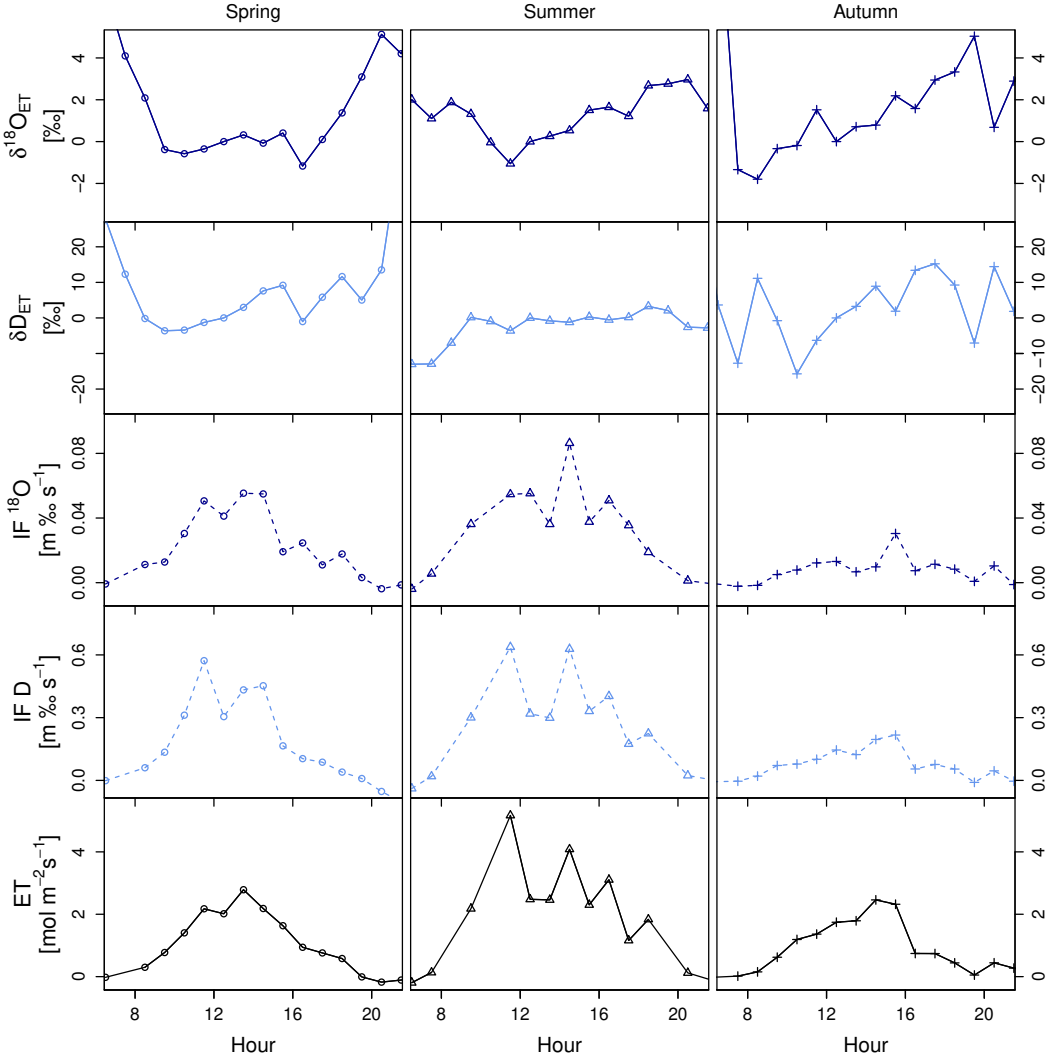

Figure 3.12: Diurnal cycles of the isotopic composition of ET δ_{ET}, isoforcing IF and ET during daytime (7h-21h GMT+1).

3.4.2.6 Dual isotope analysis of δ_{ET}

In the δ^{18}O-δD-plane, effects that influence δD and δ^{18}O differently (e.g. non-equilibrium fractionation) become visible (Dansgaard, 1964). The local meteoric water line (LMWL), can be defined by the linear regression of rain samples (Bowling et al., 2017, see e.g.), with a typical slope of 8 in the northern hemisphere (Dansgaard, 1964). Processes with non-equilibrium fractionation, such as evaporation, change the isotopic compositions in the δ^{18}O-δD-plane along shallower slopes for both, the evaporated water (Gat, 2000; Twining et al., 2006) and for the remaining liquid water (Cappa et al., 2003; Gat, 1996; Gat, 2000;

Twining et al., 2006). Thus, deviations from the LMWL can be interpreted as indications for non-equilibrium fractionation. For our dataset, dual isotope analysis (as shown in Fig. 3.13) provides evidence that ET is not dominated by non-equilibrium fractionation when there is transpiration (i.e. in the period between leaf unfolding and leaf coloring). During this time period δ_{ET} fluctuates around the LMWL. For the period when we do not expect transpiration (before leaf unfolding on 19. April and after leaf coloring on 6. of October) we find indications for non-equilibrium effects as the isotopic compositions of ET falls below the LMWL. This could be related to non-equilibrium effects of evaporation from different (enriched) water pools in the ecosystem that were subject to evaporation before. Additionally to this general difference between the transpiration-dominated and the

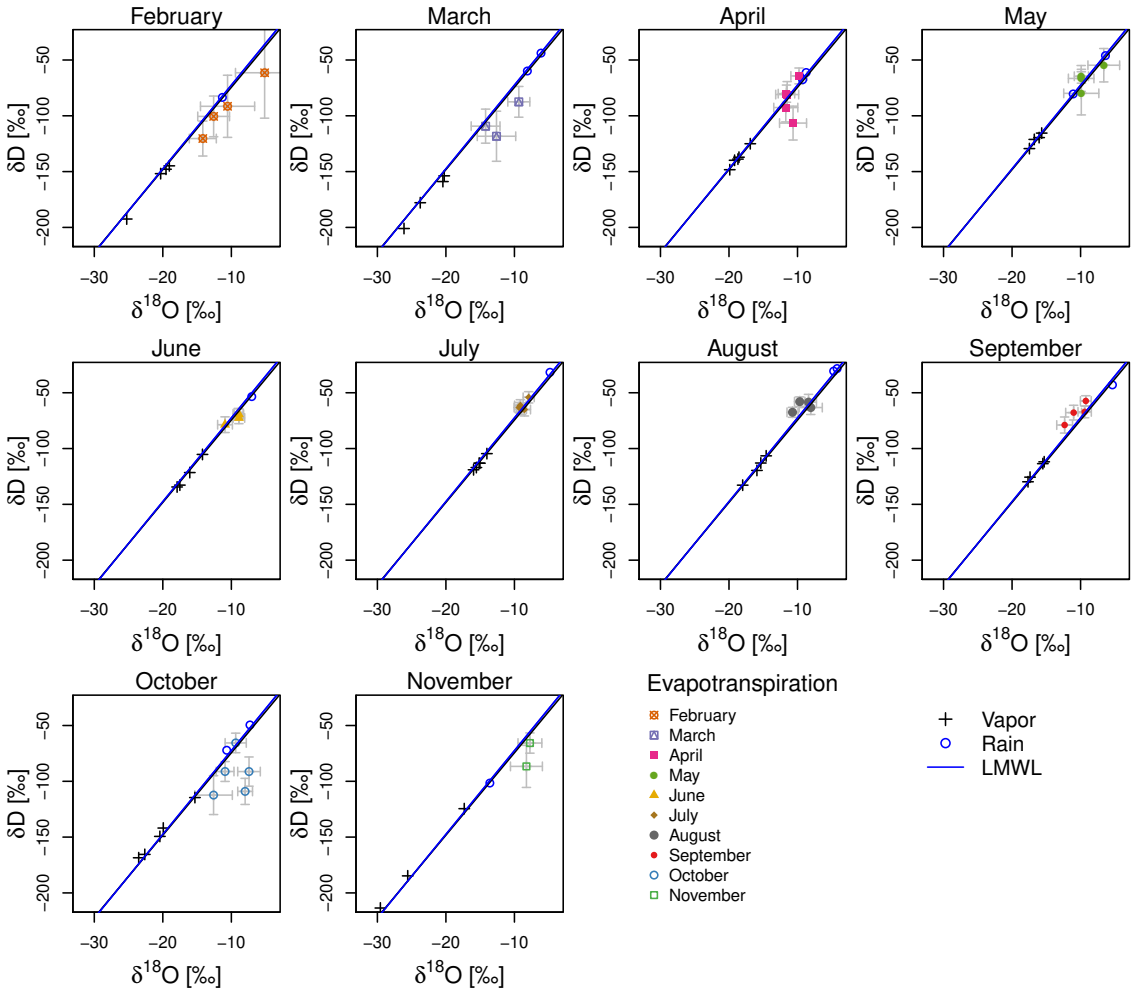

Figure 3.13: The flux-weighted weekly averages of δ_{ET}, plotted in the δD-δ^{18}O plane in combination with the corresponding weekly means of δ_v and biweekly sampled isotopic composition of (integrated) rain, plotted seperately for different months. The blue line is the local meteorologic water line with a slope of 7.4.

evaporation-dominated time periods, there is a period in August and September when δ_{ET} lies slightly above the LMWL. These two months have higher VPD than the other months (see Fig. 3.11). We propose that related to the higher VPD in these months evaporation increases in this period.

When water evaporates from water sources that were not strongly enriched in the preceeding period, the measured δ_{ET} can deviate positively from the LMWL. This has been discussed for the case of the GMWL by (Twining et al., 2006). In particular non-equilibrium evaporation from a limited amount of water (e.g. fast evaporation) could shift the isotopic composition into this direction (Dansgaard, 1964). However, such processes could be investigated further by combining direct simultaneous EC measurements of $\delta^{18}O$ and δD with chamber measurements, modeling, and sampling of plant and soil water components.

More generally, the LMWL at our field site (shown in Fig. 3.13) had a slope of 7.4, reflecting the interplay of different drivers of the isotopic composition of rain such as the isotopic composition of water vapor, the dew point and temperature during rainout as well as the way of cooling (Dansgaard, 1964). The so-defined LMWL should be interpreted with caution because our measurement period spans different seasons and thus the precipitation could be related to air masses with different water sources, which would indicate that the interpretation of the LMWL is not straightforward in all cases (Gat, 1996). However, the measured isotopic compositions of water vapor and rain are comparably close to the LMWL throughout all months.

3.5 Conclusions

Here, we demonstrated that the high-flow and high-frequency optimized water vapor isotope analyzer (2 Hz-HF-WVIA), in combination with an intense calibration is capable of eddy covariance measurements of the isotopic composition of water vapor above a forest ecosystem. Based on the measured spectra and cospectra, we conclude that in our setup, the measured fluxes are exposed to tubing effects. But these tubing effects are not isotope selective (such as condensation). Further, the obtained spectra and cospectra are comparable (slightly better) to the standard EC measurements at this field site. The uncertainties of the measured isotopic composition of ET as determined by propagated ML-uncertainties of the individual isotopologue fluxes are comparable to different uncertainty estimates of flux gradient approaches. In particular, the propagated ML-uncertainties decrease, with generally increasing net fluxes, yielding more reliable measurements in summer, when fluxes are larger. Overall, our measurements imply that EC measurements of the isotopic composition of water vapor can provide insights into the dynamics of the hydrological cycle on an ecosystem scale, in particular on weekly or monthly timescale and for periods when the net water vapor fluxes are high. A combination of EC measurements of δ_{ET} with chamber measurements, leaf, soil and twig-water sampling and modeling approaches, could help to partition ET into its components . As a proof of concept, the analysis of δ_{ET} in the $\delta^{18}O$-δD-plane highlights the potential of dual isotope analysis of δ_{ET}. We propose that such analysis, if applied in combination with measurements of different water pools and fluxes, will further help to understand the dynamics of the hydrological cycle. This is particularly interesting at sites where flux gradient approaches have limited

applicability.

3.6 Author contribution

All isotope-related measurements were planned, performed, evaluated, described and discussed by Jelka Braden-Behrens and Alexander Knohl. The data processing for the eddy covariance measurements with the standard LI-6262 analyzer were performed and interpreted by Christian Markwitz, Jelka Braden-Behrens and Alexander Knohl. Chapter 3.3.4.3, that describes the standard eddy covariance and meteorological measurements, was written by Christian Markwitz, whereas all other chapters of this manuscript were written by Jelka Braden-Behrens. All authors read and made editorial comments on the manuscript.

3.7 Competing interests

We declare that we have no conflict of interest.

3.8 Acknowledgements

This project was partly funded by a Dorothea-Schlözer Fellowship of the University of Goettingen, the German Research Foundation (DFG, project ISOFLUXESKN582/7-1), the german federal ministry of education and research (BMBF, project BonaRes, Modul A: Signal 031A562A) and the European Research Council under the European Union's Horizon 2020 research and innovation programme (grant agreement no. 682512 - OXYFLUX). We want to thank Dave Bowling for the scientific discussions, in particular for the idea of using the obtained data in a dual isotope approach and his suggestions on visualization (Fig. 3.13). Further, we thank Rijan Tamrakar for estimating storage effects for water vapor fluxes at our field site. We are very thankful for the technical support by Robert Provencal from (*Los Gatos Research. Inc*, San Jose, USA), who helped us to optimize both, the analyzer and the calibration unit for fast flow and fast measurements. We thank the technicians of the bioclimatology group of the University of Goettingen, in particular Dietmar Fellert, Frank Tiedemann and Edgar Tunsch, as well as the student assistants Martin Lindenberg and Elke Schäpermeier, who helped extensively with the experimental setup and maintenance. We thank Rick Wehr and Rachel Chang for sharing the code for the York-type fit and Andre Ringler for writing the code for the synchronization. Additionally, we are very thankful that the forest manager Ulrich Breitenstein allowed the experimental setup at this site.

3.9 Appendix

3.9.1 Propagation of the uncertainty of δ_{ET}

According to equation 3.4, the isotopic compositions of evapotranspiration (ET) are based on the ratio of two fluxes (e.g. $F_1 = F^{181}$ and $F_2 = F^{161}$). The corresponding uncertainties propagate to the ratio in the following way:

$$\frac{\sigma(F_1/F_2)}{F_1/F_2} = \sqrt{\left(\frac{\sigma(F_1)}{F_1}\right)^2 + \left(\frac{\sigma(F_2)}{F_2}\right)^2 - 2r_{F_1,F_2}\frac{\sigma(F_1)}{F_1}\frac{\sigma(F_2)}{F_2}} \tag{3.9}$$

With the correlation coefficient $r_{F_1,F_2} := \overline{F_1' F_2'}/(\sigma_{F_1}\sigma_{F_2})$ between F_1 and F_2. As the measured r_{F_1,F_2}, based on all measured data, is above 0.999, we approximate r_{F_1,F_2} with 1 in Eq. 3.9.

3.9.2 Filtering criteria for flux measurements

We used the following criteria to remove outliers from the hourly measured (isotopologue) fluxes, following the standard methodology at this site:

- We removed all data with a quality flag of 2, using the flagging policy 'Mauder and Foken, 2004' in EddyPro (see LiCor Biosciences, 2016).
- We removed water vapor fluxes below -0.1 $\mathrm{mmol\,m^{-2}s^{-1}}$.
- We filtered out the fluxes with a variance of H_2O above its 97.5-percentile.

Additionally, we removed outliers of δ_{ET} that exceeded a range from -20 to 0 ‰ for $\delta^{18}O$ and from -150 to -10 ‰ for δD.

3.9.3 Comparison of net fluxes (Moncrieff)

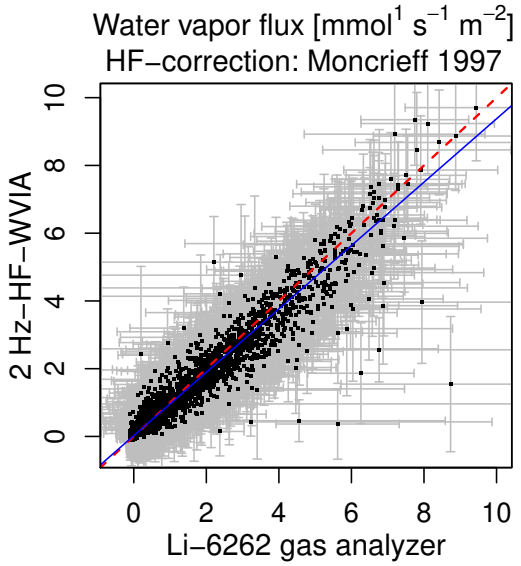

Figure 3.14: Hourly evaluated net fluxes (black points) as measured with the two different analyzers (2 Hz-HF-WVIA, and LI-6262) with their ML-uncertainties in gray. A York-type fit (blue line) with a slope of 0.94 and a R^2 of 0.92 is shown in comparison to the 1:1 line (red, dashed line). The accordance of the net fluxes measured with the different analyzers depends on the applied high-frequency correction, here: according to Moncrieff et al. (1997a).

3.9.4 Calibration of $C_{\mathrm{H2O,v}}$

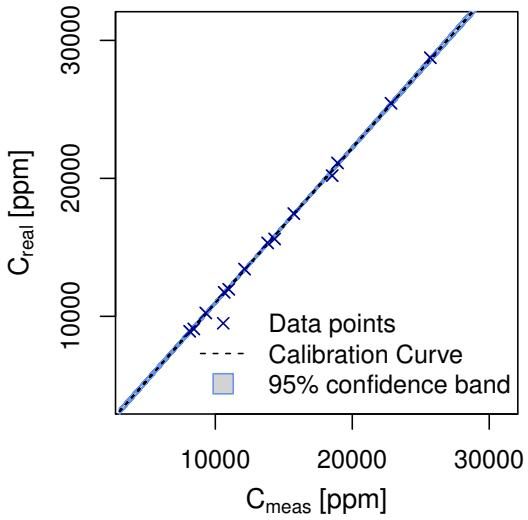

Figure 3.15: The mole fraction calibration was linear with a slope of approximately 1.12 and a coefficient of determination R^2 above 0.999.

3.10 Supplementary material

3.10.1 The effect of storage on net water vapor fluxes

We used standard EC measurements (described in section 3.3.3) in combination with profile measurements at nine inlet heights that range from 0.1 to 45 m to estimate the contribution of storage effects (see chapter 3.3.2.3) to evapotranspiration throughout the year 2016. This calculation of storage fluxes was carried out by Rijan Tamrakar (Bioclimatology group, Göttingen University). Based on a linear regression of ET against the measured eddy flux density with a slope of 0.97 and an R^2 of 0.94, we conclude that at our field site the contribution of storage to ET is below the general uncertainty of the EC method.

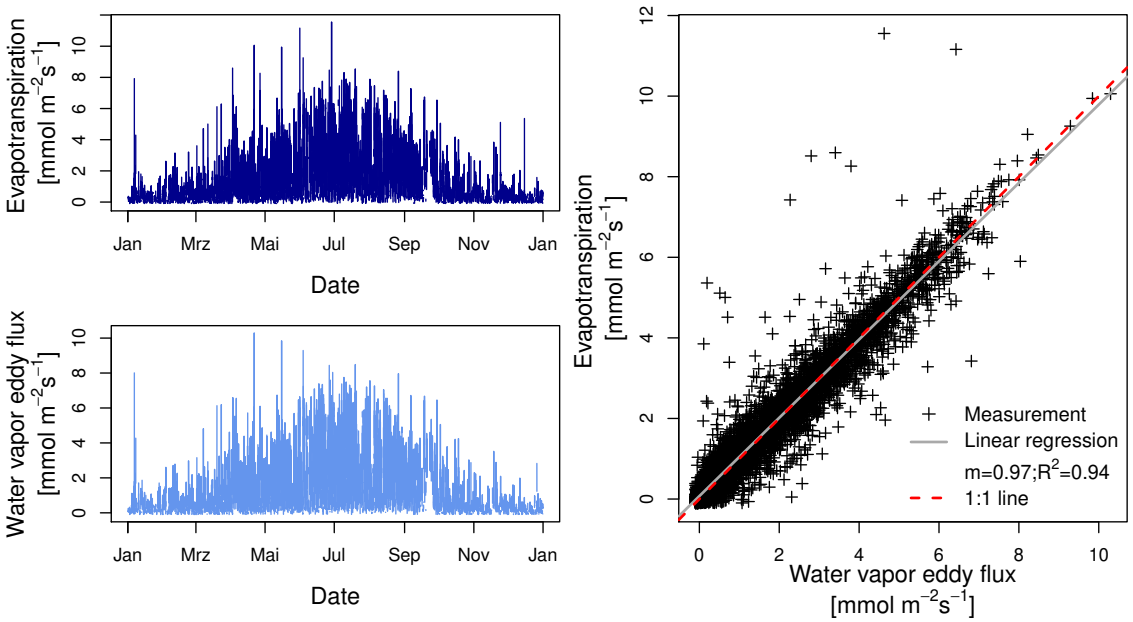

Figure 3.16: The left panels show the time series of ET in dark blue (based on storage corrected EC measurements) and the water vapor eddy flux (without storage correction) in light blue. The right panel shows a direct comparison of ET and water vapor eddy flux, resulting in a linear regression with a slope of 0.97 and an R^2 of 0.94.

CHAPTER 4

Does local evapotranspiration drive seasonal and diurnal variations in the isotopic composition of water vapor above a managed beech forest?

Manuscript to be submitted to 'Biogeosciences' (Braden-Behrens et al., 2018a)

4.1 Abstract

Measurements of the isotopic composition of water vapor as well as measurements of the isotopic composition of evaporation and transpiration provide valuable insights in the hydrological cycle. Here we present measurements of the isotopic composition of water vapor δ_v in the surface boundary layer (SBL) in combination with eddy covariance (EC) measurements of the isotopic composition of evapotranspiration δ_{ET} for both δD as well as δ^{18}O over a full growing season of a managed beech forest in central Germany. We used these measurements in combination with meteorological and standard EC measurements to evaluate the influence of local ET and entrainment on the isotopic in the SBL. We test the hypothesis, during summer, when transpiration is high, local ET is a dominant control of δ_v at our measurement position, in only 10 m above the canopy. We found that even for spring and summer, when transpiration is high, ET dominates the diurnal cycle of δ_v in the SBL in the mornings and evenings, while entrainment effects overrule ET from approximately 10 to 16 h. On a diurnal timescale, the isotopic composition of water vapor in the SBL is alternately dominated by local ET and entrainment. On a seasonal timescale, we found no evidence for a dominant control of δ_v by entrainment or local ET. A significant correlation between δ_v and the logarithm of the water vapor mole fraction C_{H2O} with a comparably small R^2 of approximately 0.35 ($p < 10^{-20}$) implied, that Rayleigh distillation might explain a limited part of the observed variability. However, we obtained a comparably stronger significant correlation between δ_v and temperature (with $R^2 \approx 0.52$ and $p < 10^{-35}$). Based on these measurements, we propose that the observed seasonal variability of δ_v was neither dominated by Rayleigh processes, entrainment nor local ET, but could be linked to temperature-related processes such as fractionation during evaporation from sources that do not correspond to the sources of local ET. such as large-scale moisture sources.

4.2 Introduction

The isotopic composition of water vapor (δ_v) in the atmosphere can provide insights into the hydrological cycle on scales ranging from leaf scale to global scale (Gat, 1996; Huang et al., 2014; Jouzel et al., 2000; Wen et al., 2010; Yakir et al., 2000). Potential drivers of the temporal variability of δ_v are the removal of rain from the atmosphere (Gat, 2000), vertical atmospheric mixing, transpiration and evaporation from open water bodies, various (temperature dependent) fractionation processes of ET (Gat, 2000), and selective ET from different water sources (Gat, 2000; McDonnell, 2014). Continuous measurements of δ_v were carried out above various ecosystems (see e.g. Huang et al., 2014, for a list of such measurement sites). Fewer studies discuss the importance of ET and entrainment based on directly measured δ_{ET} (and/or the corresponding isoforcing). Such direct measurements of $\delta^{18}\mathrm{O}_{\mathrm{ET}}$ have been carried out based on flux gradient measurement above a temperate forest (Lee et al., 2007), above an arid artificial oasis (Huang et al., 2014) and above a corn/soybean canopy (Welp et al., 2008) as well as based on eddy covariance measurements above a corn/soybean canopy (Griffis et al., 2010; Griffis et al., 2011). The measurements by (Huang et al., 2014) additionally captured $\delta\mathrm{D}_{\mathrm{ET}}$.

On a diurnal timescale δ_v is driven by multiple processes such as ABL growth and decay

(Lee et al., 2012a), vertical atmospheric mixing (Noone et al., 2013), or entrainment of drier and isotopically lighter air from the free atmosphere, land-sea breeze circulation, ET, advection, and in-cloud condensation and precipitation (Lee et al., 2006) as well as the origin and the different histories of air masses and the sublimation of snow (Noone et al., 2013). Entrainment is a mixing process driven by the gradients at the capping inversion between the atmospheric boundary layer (ABL) and the free atmosphere (Lee et al., 2012a). Thus, entrainment transports dry and isotopically more depleted air into the ABL (Lee et al., 2012a). Transpiration on the other hand, the major part of ET on global scale (Jasechko et al., 2013), isotopically enriches[1] the vapor in the surface layer (Lee et al., 2006). Multiple authors find that at various field sites, entrainment and ET are the dominant drivers of the variability of δ_v on a diurnal timescale. The influence of entrainment and ET in particular was discussed based on large eddy simulations (Lee et al., 2012a), repeated profile measurements (Lai et al., 2011; Noone et al., 2013), measured time series of δ_v (Huang et al., 2014; Welp et al., 2012; Zhang et al., 2011), as well as direct measurements of δ_{ET} (Griffis et al., 2010; Huang et al., 2014; Lee et al., 2007; Welp et al., 2008). In summary, these studies discuss the influence of entrainment and ET on the obtained diurnal cycles of δ_v, concluding a dominance of entrainment (Griffis et al., 2010; Lai et al., 2011; Lee et al., 2007), ET (Huang et al., 2014; Zhang et al., 2011), both (Lee et al., 2012a; Noone et al., 2013; Welp et al., 2012), or both in combination with dew formation (Welp et al., 2008). However, it is worth to point out, that only four of these studies (Griffis et al., 2010; Huang et al., 2014; Lee et al., 2007; Welp et al., 2008) are based on measurements of δ_{ET} (see the list of the used methods above). In these cases, the mentioned dominant controls of δ_v were based on a the obtained diurnal cycles of δ_v in combination with positive isoforcing values (Griffis et al., 2010; Huang et al., 2014) and also on a quantification of the magnitude of the isoforcing-related change in δ_v (Lee et al., 2007; Welp et al., 2008).

On a seasonal timescale, δ_v is related to the removal of rain from the atmosphere. This is a complex process, including the origin of the air masses, the degree of cooling since the beginning of condensation (Ambach et al., 1968), fractionation during condensation, evaporation from falling droplets and isotopic exchange between falling droplets and the surrounding air masses, as well as the thermodynamic conditions during cooling (see e.g. Dansgaard, 1964). Effects that influence the isotopic composition if precipitation and the surrounding air masses are the 'amount effect' (small amounts of rain are enriched) and the 'temperature effect' (higher condensation temperature is related to higher δ-values of precipitation) (e.g. Dansgaard, 1964). At a global level, the geographical and seasonal variation in the isotopic composition in precipitation can be described by 1) the latitude effect, 2) the elevation effect 3) the continental effect, the 4) seasonal effect and 5) the amount effect (described above) as discussed e.g. by (Michener et al., 2007). However, in a simplified model the removal of rain from the atmosphere can be described as a Rayleigh

1 This statement is mentioned by Lee et al. (2006) particularly for $\delta^{18}O$. For δD, it can be derived from the above cited statement for $\delta^{18}O$ in combination with the fact that transpiration is not expected to change local deuterium excess d_{local} (Gat, 1996).

distillation process (Gat, 2000; Lee et al., 2006), i.e. the removal of material from an open system (Gat, 1996). Rayleigh distillation yield a log-linear relationship between the isotopic composition of water vapor δ_v and its mole fraction C_{H2O} - this refers to the linearized form of the Rayleigh equation (see e.g. Lee et al., 2006).

$$\delta_v = \delta_{v,0} + (\alpha - 1) \times \log\left(\frac{C_{\mathrm{H2O}}}{C_{\mathrm{H2O},0}}\right) \tag{4.1}$$

With the subscript 0 as a label for the values at the source (before Rayleigh rain-out) and the (temperature dependent) equilibrium fractionation factor α. Such a log-linear relationship has been found by many authors with R^2 values ranging from approximately 0.15 (Huang et al., 2014) to 0.78 (Lee et al., 2006; Wen et al., 2010) indicating different importance of Rayleigh processes as drivers of the seasonal variability of δ_v. Additionally or alternatively to Rayleigh rain-out, the seasonal variability of δ_v can be related to local ET. Indications for the influence of local ET are discussed by Huang et al. (2014), who obtained a correlation between daytime δ_v and δ_{ET} (based on flux gradient measurements). Further evidence of the importance of ET in the ABL water budget was found based on modeling and flux gradient measurements of $\delta^{18}\mathrm{O}_{\mathrm{ET}}$ (and for some month also $\delta\mathrm{D}_{\mathrm{ET}}$) at a tall tower above a dryland crop/grassland ecosystem (Griffis et al., 2016). Based on their measurements and modeling, they estimated the relative contribution of ET to the water in the ABL and found values spanning the range from 0 to close to 100 %, with a median of 34% (Griffis et al., 2016).

Here we present a time series of measurements of the stable isotopic composition of water vapor in $\delta^{18}\mathrm{O}_v$ and $\delta\mathrm{D}_v$ in the SBL above a managed beech forest in central Germany in combination with direct eddy covariance measurements of the magnitude and the isotopic composition of ET and standard meteorological measurements. Our objectives are to evaluate the influence of entrainment and local ET on δ_v in the SBL based on these measurements. Our measurements were carried out at a height of approximately 10 m above the top of the canopy in the SBL and thus we expect high transpiration during summer. Further, a high contribution of ET to the water vapor in the atmospheric boundary layer (ABL) has been found even at a crop/grassland site at 185 m above ground (Griffis et al., 2016). Thus we hypothesize, that at our field site, ET is an important driver of δ_v, in particular during summer. However, as discussed above, many authors found evidence for an additional influence of entrainment on the diurnal variability of δ_v at various field sites (Griffis et al., 2010; Lai et al., 2011; Lee et al., 2012a; Lee et al., 2007; Noone et al., 2013; Welp et al., 2012; Welp et al., 2008). Thus, we further hypothesize, that at our field site, the variability of $\delta^{18}\mathrm{O}_v$ and $\delta\mathrm{D}_v$ is dominated by entrainment on a diurnal timescale, but local ET might be important on a seasonal timescale.

Table 4.1: Nomenclature and abbreviations used in this publication

	Stable isotope specific notations
R_{std}	Isotopic ratio of a standard material
δ	Relative deviation of the measured isotope ratio from R_{std}
δ_v	Isotopic composition of water vapor
δ_v	Isotopic composition of water vapor
IF	Isoforcing; IF := $\overline{w'\delta'}$
	Abbreviations
ABL	Atmospheric boundary layer
SBL	Surface boundary layer
EC	Eddy covariance
ET	Evapotranspiration
WVIA	Water vapor isotope analyzer
2 Hz-HF-WVIA	WVIA for 2 Hz measurements (with high flow plumbing)
WVISS	Water vapor isotope standard source
HF-WVISS	WVISS optimized for high flow
DPG	Dew point generator
VSMOW	Vienna standard mean ocean water
IRMS	Isotope ratio mass spectrometry
GMWL	Global meteoric water line
LMWL	Local meteoric water line
	Meteorological quantities
RH	Relative humidity
VPD	Vapor pressure deficit
TKE	Turbulent kinetic energy
u^*	Friction velocity
C_{H20}	Water vapor mole fraction

4.3 Material and methods

4.3.1 Field site

The field site of this study is located in central Germany (51°19'41,58" N; 10°22'04,08" E; approximately 450 meters above sea level) and vegetated by a managed beech forest (dominated by *Fagus sylvatica L.*). The forest in the surroundings of the tower has a relatively homogeneous top-weighted canopy structure (Anthoni et al., 2004; Braden-Behrens et al., 2017a). The forest height (defined as the average height of the highest 20 % of the trees) was 37 m in 2004 and the maximum leaf area index was approximately $4\,m^2m^{-2}$ (Anthoni et al., 2004).

4.3.2 Stable isotope measurements of δ_{H2O}

We used a customized version of a commercially available water vapor isotope analyzer (2 Hz-HF-WVIA, *Los Gatos Research. Inc.,San Jose, USA*) to measure the water vapor mole fraction C_{H2O} and its stable isotopic compositions $\delta^{18}O_v$ and δD_v at 44 m height above the forest floor. The non-customized version of this instrument has been described in detail (cf. Aemisegger et al., 2012; Los Gatos Research Inc., 2013). This analyzer is an off-axis integrated-cavity output spectrometer in near infrared, i.e. a laser-based absorption spectrometer that uses a high-finesse optical cavity to enhance the optical path length (Los Gatos Research Inc., 2013). The customization of this instrument is described in detail by Braden-Behrens et al. (2018b) and enabled us to take measurements with a frequency of 2 Hz at a flow rate of approximately 4.2 slpm. The 2 Hz-HF-WVIA was calibrated hourly with a customized version of the water vapor isotope standard source (WVISS, *Los Gatos Research. Inc.*,San Jose, USA). In brief, this calibration unit dries and compresses ambient air and mixes it with nebulized liquid water, that is further diluted to yield water vapor with different mole fractions at a constant isotopic composition (see e.g. Aemisegger et al., 2012; Los Gatos Research Inc., 2012). We customized this calibration unit to enable calibration at the analyzer's flow rate of 4.2 slpm over a broad mole fraction range (see Braden-Behrens et al., 2018b).

4.3.3 Eddy covariance measurements of δ_{ET}

We measured the three dimensional wind velocity and the sonic temperature at 44 m height above the forest floor with a measurement frequency of 20 Hz using a sonic anemometer (Gill-R3, *Gill Instruments*, Lymington, UK). The inlet of the $\delta^{18}O_v$ and δD_v measurements was in the vicinity of this anemometer with a 5 cm northward, a 10 cm eastward and a 20 cm vertical separation. We combined the 20 Hz anemometer measurements with the 2 Hz measurements of $\delta^{18}O_v$ and δD_v to calculate the magnitude and the isotopic composition of ET using the eddy covariance software EddyPro®, version 6.2.0 (LiCor Biosciences, 2016). Further specification of this setup such as tubing material, tube heating, flow rates and the different data processing settings are described in detail by Braden-Behrens et al. (2018b). In brief, the tubing to the 2 Hz-HF-WVIA was made of PTFE (teflon) and heated to avoid condensation. The flow rates in the main tubes were chosen to guaranty turbulent conditions within the tubes upstream of the analyzer. Data processing settings included double rotation and block averaging, spike removal, correction for instrument separation, as well as spectral corrections in the high frequency and low frequency range (Braden-

Behrens et al., 2018b). Additionally to the stable isotope eddy covariance measurements, the meteorological tower is also equipped with a standard closed path CO_2 and H_2O_v analyzer (LI-6262 *LiCor Inc.*, Lincoln, USA). The inlet of this analyzer is in the vicinity of the anemometer with -5 cm northwards, 10 cm eastwards and 20 cm vertical separation. We used this analyzer in combination with the sonic anemometer for standard eddy covariance measurements and to evaluate our stable isotope setup. A direct comparison of both EC setups shows that if an high frequency correction according to Moncrieff et al. (1997a) is applied, the 2 Hz-HF-WVIA underestimated the net H_2O_v flux by approximately 6 % (Braden-Behrens et al., 2018b). The regression against the standard measurement of the H_2O_v flux has a slope of 0.94 and an R^2 of 0.92 (Braden-Behrens et al., 2018b).

4.3.4 Calculation of isoforcing

We quantified potential effects of ET on the isotopic composition of the atmosphere, by calculating isoforcing, based on EC measurements of the magnitude and the isotopic composition of ET (described in Braden-Behrens et al., 2018b). Isoforcing (see e.g. Lee et al., 2009) can be interpreted as the rate of change of the atmospheric δ value multiplied by the boundary layer height h, if a simple isotopic mass balance model (see e.g. Lai et al., 2006) is assumed with only a flux component from the surface and no horizontal advection or entrainment from above (see also Braden-Behrens et al., 2018b; Sturm et al., 2012).

$$\mathrm{IF} = \frac{F}{C_a \rho_a}(\delta_F - \delta_a) = h\frac{\mathrm{d}\delta_a}{\mathrm{d}t} \tag{4.2}$$

With the flux F (e.g. ET), its isotopic composition δ_F (e.g. δ_{ET}), the atmospheric mole fraction C_a, the molar density of atmospheric air ρ_a, the atmosphere's isotopic composition δ_a and the boundary layer height h.

4.3.5 Additional meteorological and isotopic measurements

Additionally to the stable isotope measurements and the EC measurements, the meteorological tower at this site is equipped with standard meteorological measurements (see Anthoni et al., 2004, for details). Among other variables, the air and soil temperatures are measured at 2 m and 44 m height and at 2, 8, 16, 32 and 64 cm depth, respectively. Relative humidity (RH), vapor pressure deficit (VPD), precipitation amount, as well as wind direction and velocity are measured at 44 m height. A set of different radiation sensors measure diffuse, up- and downwelling longwave, shortwave, photosynthetically active radiation as well as net radiation (see also Braden-Behrens et al., 2018b). In this experiment, we also measured the isotopic composition of rain above the canopy using three integrated rain samplers. We build the integrated rain samplers based on the description of Gröning et al. (2012). Every second week, we took two samples out of each of the integrated rain samplers and analyzed them for their $\delta^{18}O$ and δD composition at the centre for stable isotope research and analysis (*KOSI*, University of Goettingen) using isotope ratio mass spectrometry (IRMS). After the subsamples were taken, the bottles of the integrated rain samplers were replaced by dry bottles. The uncertainty of our rain sample measurements, as quantified by the median of the standard deviations of the 6 respective subsamples of each data point was approximately 0.2 ‰ for $\delta^{18}O$ and 1.5 ‰ for

δD.

4.4 Results and discussion

4.4.1 Diurnal variability

The mean diurnal cycles (Fig. 4.1) in combination with the positive isoforcing values show conclusively that local ET does not dominate the diurnal variability of δD_v and $\delta^{18}O_v$, even if our measurement position is only 10 m above the treetops. In particular, this is also the case during summer, when transpiration is high. Thus, the measured data does not support our hypothesis that during summer, local ET is an important driver of δ_v. In summer (June to August) the obtained diurnal cycles of δD_v and $\delta^{18}O_v$ values resemble a sine curve with an enrichment from midnight until approximately 10 h local winter time (GMT+1)[1] followed by a depletion throughout the day until 16 h by approximately 1 ‰ for δ^{18}O and 4.5 ‰ for δD. All isoforcing values (calculated with Eq. 4.2) were positive, and thus correspond to an enrichment of the atmospheric δ value due to ET. Over the course of the mean diurnal cycle, the isoforcing values rose in the mornings and decreased in the afternoon. In summer, the period with the most pronounced diurnal cycles, the amplitude was approximately 0.08 and 0.6 m‰ s^{-1} for δ^{18}O and δD respectively (Figure 4.1). Comparably large isoforcing values were found by other authors (Hu et al., 2014; Lee et al., 2007; Welp et al., 2008). Uning Eq. 4.2 and assuming a boundary layer height h of 1000 m and only one flux from the land surface, these amplitudes of IF would correspond to a change $d\delta_a/dt$ of approximately 0.3 ‰ h^{-1} and 2.2 ‰ h^{-1} for δ^{18}O and δD respectively. Thus, within three hours, the isoforcing related to ET (in summer) would yield an increase in δ_v with an amplitude, that is comparable to the observed diurnal variability of approximately 1 ‰ and 6 ‰, for δ^{18}O and δD respectively (see Fig. 4.1). But whereas isoforcing would yield a progressive enrichment of δ_v, the observed diurnal cycles of δ_v, show different shapes. Around midday, when ET is large, the mean diurnal cycles of both $\delta^{18}O_v$ and δD_v show the opposite trend with decreasing δ_v from 10 to 16h in summer, and from 11 to 16h in spring, and a rather constant δ_v in autumn.

Diurnal cycles that deviate from this sine-shaped pattern (Fig. 4.1) were obtained at various sites and were related to different drivers by the respective authors: Negative concave diurnal cycles of δ^{18}O have been associated to synoptic meteorology (Griffis et al., 2010), a combination of dew formation, ET and boundary layer mixing (Welp et al., 2008), and land-sea breeze circulation (Lee et al., 2006). A steady increase in δ_v was obtained during the peak growing season of a winter wheat canopy and associated with a dominant influence of ET on δ_v (Zhang et al., 2011). Further, more complex diurnal cycles were observed over an artificial oasis cropland in the late growing season and associated to the interaction between local ET and entrainment (Huang et al., 2014). However, diurnal cycles of δ_v that are similar to the observed sine-shaped diurnal cycle have been obtained at field sites with less transpiration such as an urban cite in Bejing (Zhang et al., 2011), or an artificial oasis cropland in the late growing season (Huang et al., 2014). However, a similar diurnal cycle can also be found in a large eddy simulation (Lee et al., 2012a;

1 All times given in this paper refer to local winter time (GMT+1).

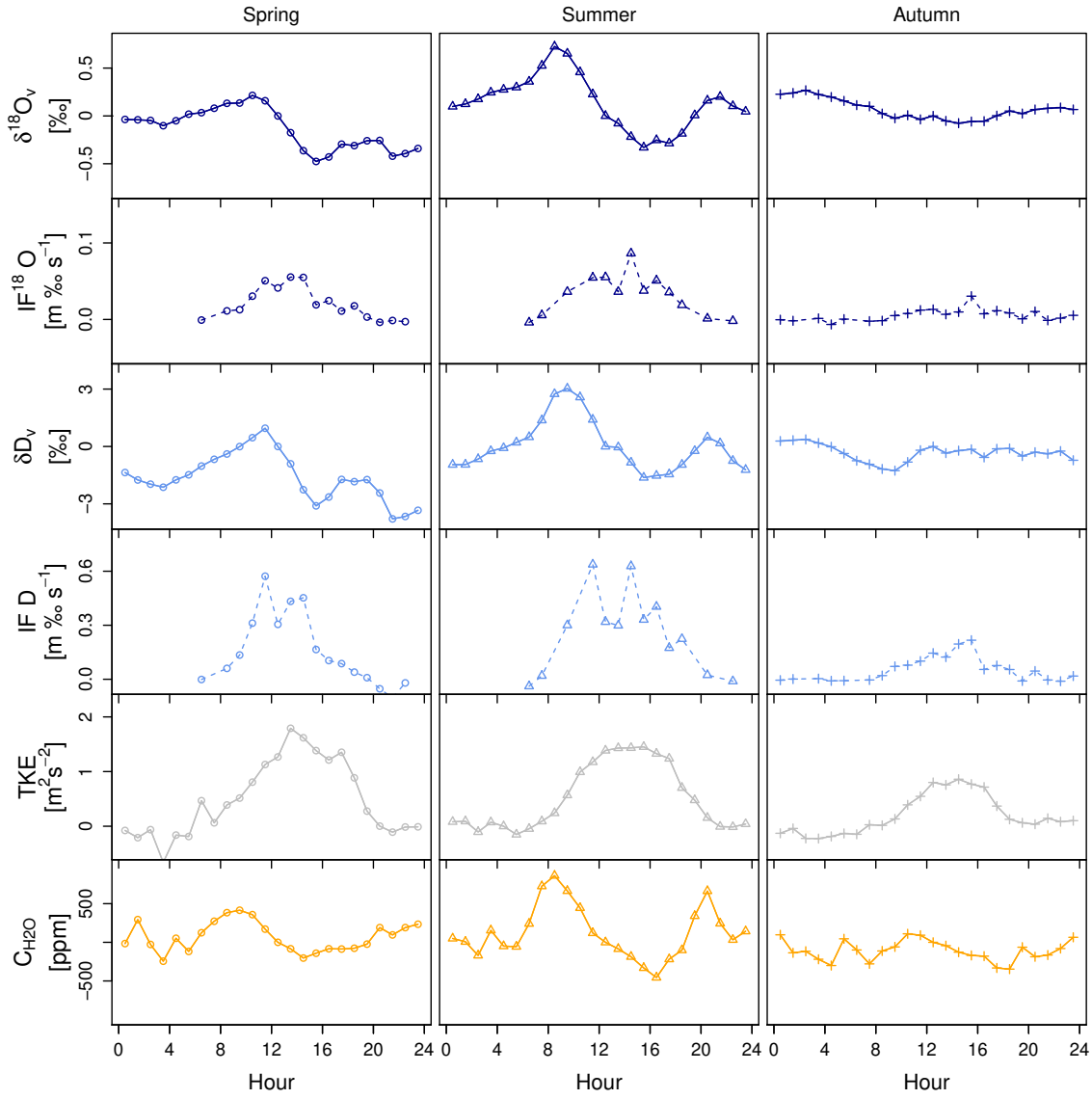

Figure 4.1: Mean diurnal cycles of the isotopic composition of water vapor δ_v, isoforcing IF, turbulent kinetic energy TKE and water vapor mole fraction C_{H2O} for spring (March to May), summer (June to August) and autumn (September to November).

Lee et al., 2012b).[1] The authors of the above mentioned studies discuss boundary layer mixing effects (or entrainment) as a dominant factor for the obtained decrease of δ_v from the forenoon to the afternoon (Huang et al., 2014; Lee et al., 2012a; Zhang et al., 2011). The observed diurnal cycles indicate, that such a dominant influence of entrainment from

1 The latter simulation observes a depletion of $\delta^{18}O_v$ close to the surface (0 to 100 m) throughout the day with an amplitude above 2 ‰ from the forenoon to the afternoon (Fig S3(e) in Lee et al., 2012b).

the forenoon to the afternoon can even be found closely above a forest canopy during summer, when transpiration is high.

The diurnal cycles of TKE and C_{H2O} (Fig. 4.1) support the hypothesis that the diurnal cycle of δ_v is alternately dominated by entrainment and local ET throughout the day. As turbulence increases boundary layer mixing, we assume that larger TKE corresponds to larger entrainment. The observed decreasing δ_v values throughout the day occur during a time period with larger TKE (Fig. 4.1). Additionally, spring and summer show a diurnal cycle of TKE that is larger than in autumn, when there is only little indication for entrainment in the diurnal cycle of δ_v (Fig. 4.1). Further indications for the dominant influence of entrainment can be found in the diurnal cycle of the water vapor concentration C_{H2O}. In particular during summer, the diurnal cycle of C_{H2O} shows a rise of C_{H2O} before 9 and after 16 h and a decrease of C_{H2O} between 9 and 16 h. The concurrent trends in the diurnal cycles of C_{H2O} and δ_v indicate, that the rise in δ_v in the morning and in the afternoon is related to a water source (e.g. local ET) whereas the decrease of δ_v throughout the day is related to mixing with dry air (entrainment).

4.4.2 Seasonal variability and potential drivers of δ_v

Over the growing season, the hourly averaged water vapor mole fraction C_{H2O} at 44 m height varied from approximately 4000 to 25 000 ppm, while the corresponding isotopic compositions δ_v varied from approximately -33 to -12 ‰ for $\delta^{18}O_v$ and from −147 to -12 ‰ for δD_v (Fig. 4.2). Similar ranges for $\delta^{18}O_v$ and δD_v over a full year have been measured at various sites (e.g. Griffis et al., 2016; Huang et al., 2014; Welp et al., 2012). Potential processes that could drive the observed seasonal variability of δ_v are local ET, rain-out (Rayleigh distillation), selective water use by plants and (temperature dependent) fractionation.

In particular for our measurement position in the SBL (at 44 m height, i.e. only 7 m above the approximately 37 m high forest) local ET could be an important driver of δ_v because the measurements are carried out close to the evaporating source. To evaluate if local ET drives the seasonal variability of δ_v, we calculated the correlations between δ_v and the respective local isoforcing (measured with eddy covariance) based on daily averaged data (Fig: 4.3). Over the whole measurement period (period: 'all times' in Fig: 4.3) the calculated correlations between δ_v and isoforcing (IF D, IF ^{18}O) are insignificant (p>0.1). But for the time period between leaf unfolding and leaf senescence in fall (period: 'green leaves' in Fig: 4.3), when we expect transpiration, there are significant ($p < 10^{-10}$) correlations between δ_v and the corresponding isoforcing values IF for both, δD_v ($R^2 \approx 0.25$) and $\delta^{18}O_v$ ($R^2 \approx 0.33$). These correlations between IF and δ_v are negative (as shown in Fig. 4.3). If local ET drove the isotopic composition of ambient water vapor, we would obtain a positive correlation between IF and δ_v. Thus, we discard the hypothesis that the local ET of the forest drives the seasonal variability of δ_v measured at 44 m above the forest floor. This is in contrast to the conclusion by Huang et al. (2014), who interpreted a correlation between the (daytime) δ_v and δ_{ET} as an indication for the influence of local ET. In our dataset, we indeed find a similar (also positive) correlation between δD_{ET} and δD_v (see Table 4.2), but this correlation is not accompanied by a positive correlation to isoforcing. However, the obtained significant negative correlations of δ_v to IF for both

isotopic species imply, that at the field site of our measurement campaign ET does not dominate the seasonal variability of δ_v.

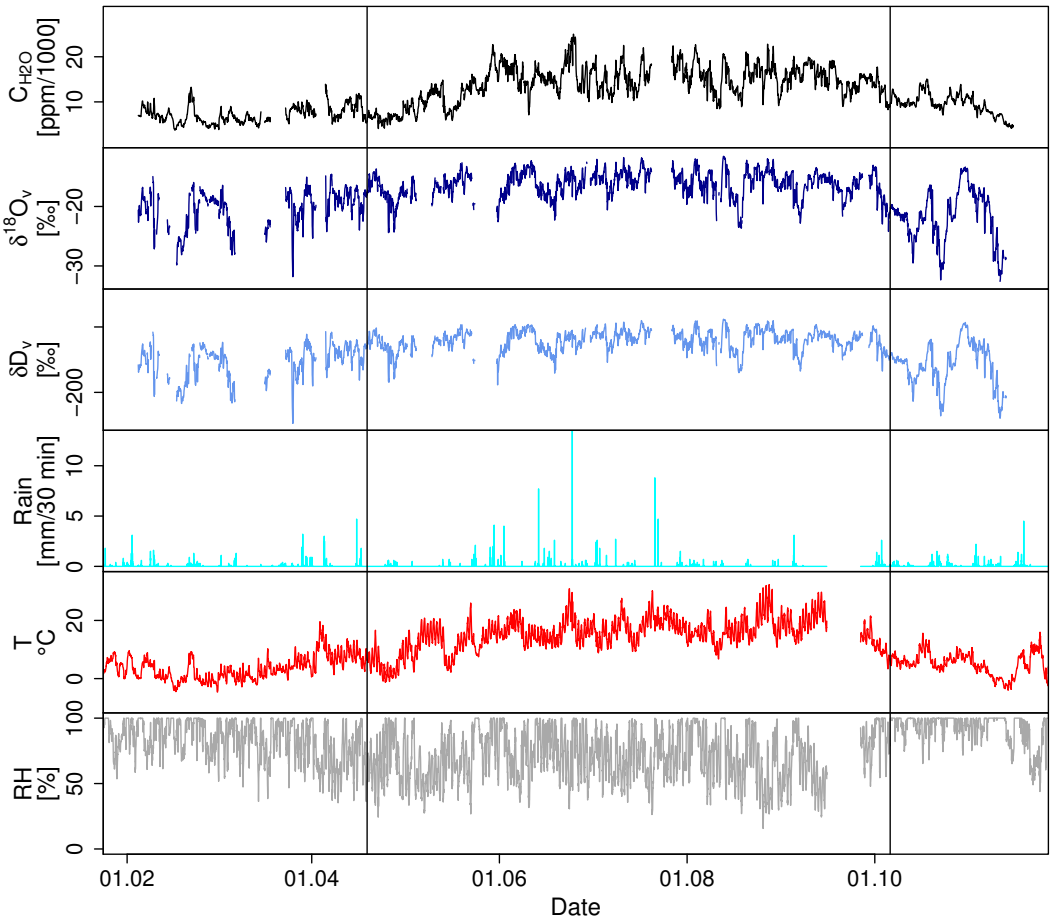

Figure 4.2: Time series of the measured water vapor mole fraction C_{H2O} (black) and its isotopic composition in δ^{18}O (dark blue) and δD (light blue) in combination with rain above the canopy (cyan), temperature in 2 m height (red) and relative humidity (grey). The vertical lines mark the times of the beginning of leaf unfolding on 19. April 2016 and the beginning of leaf senescence on 6. October 2016.

Rayleigh rain-out is another potentially important driver of the seasonal variability of δ_v. As Rayleigh distillation processes yield a log-linear relationship between δ_v and C_{H2O} (Eq. 4.1), we test for a dominant control of the seasonal variability of δ_v by a linear regression between δ_v and $\log(C_{H2O})$ (see Fig. 4.4). Throughout the whole measurement period, both δ_v values correlate only moderately with each other (with R^2 values around 0.4), but significantly (with $p < 10^{-25}$) to $\log(C_{H2O})$ (see Table 4.2). This relationship is dominated by the period before leaf unfolding and the period after leaf senescence in fall (Fig. 4.4) and is particularly weak during the period between leaf unfolding and coloring, with R^2 values below 0.2 (Table 4.2). This moderate correlation that gets weaker when green leaves are present implies, that Rayleigh distillation drives some variability in δ_v, but in particular during summer Rayleigh distillation does not dominate changes in δ_v. Stronger correlations between δ_v and $\log(C_{H2O})$ on a seasonal timescale have been reported at various other sites, for $\delta^{18}O$ (Griffis et al., 2016; Lee et al., 2007; Lee et al., 2006; Welp et al., 2008; Wen et al., 2010; Zhang et al., 2011) and also for δD (Wen et al., 2010; Zhang et al., 2011). However, even smaller correlation coefficients (below 0.2) were obtained above an arid artificial oasis (Huang et al., 2014). Similar to the results of our study, the correlation obtained by Huang et al. (2014) also gets weaker in summer.

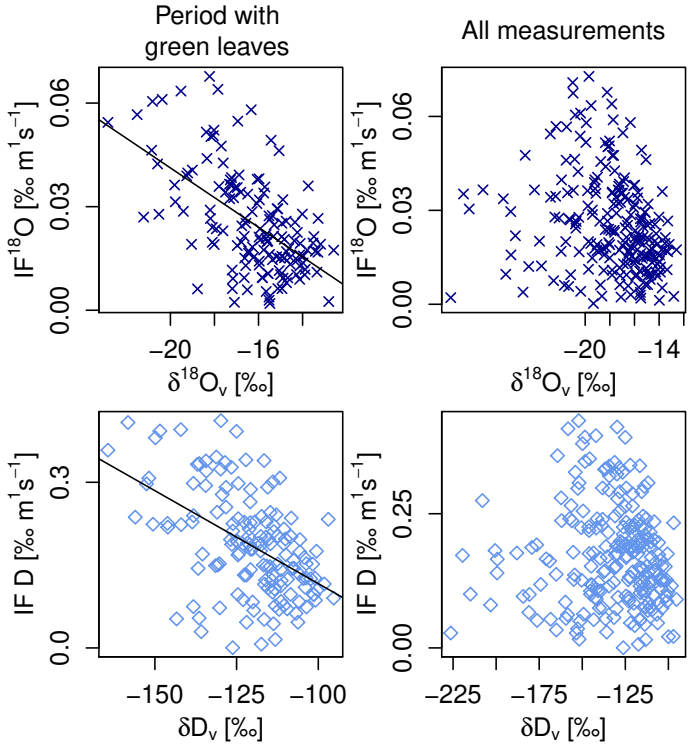

Figure 4.3: The isotopic composition of vater vapor δ_v plotted against isoforcing IF on a diurnal timescale. The black lines are significant linear regressions with $R^2 \approx 0.25$, $p < 10^{-7}$ for δD and $R^2 \approx 0.33$, $p < 10^{-10}$ for $\delta^{18}O$.

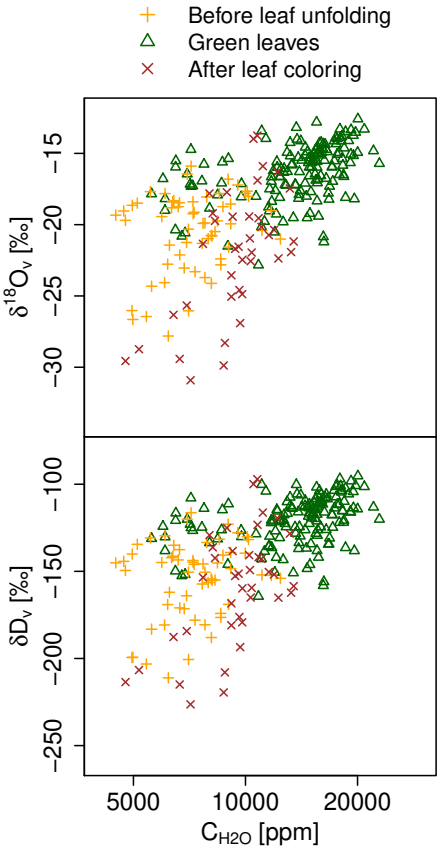

Figure 4.4: Semi-logarithmic plot of δ_v against C_{H2O}, based on diurnal averages. The different symbols are different periods: The period before leaf unfolding (orange crosses), the period with green unfolded leaves (green triangles) and the period after the beginning of leaf senescence in fall (brown diagonal crosses). A log-linear relationship would indicate a system that is dominated by Rayleigh distillation.

In the δ^{18}O-δD-plane, deviations from Rayleigh distillation processes can be further evaluated (see e.g. Bowling et al., 2017; Dansgaard, 1964; Gat, 2000). In the δ^{18}O-δD-plane, meteoric waters (precipitation and waters from rivers and lakes) from globally distributed locations[1] are aligned along the so-called global meteoric water line (GMWL, δD=8δ^{18}O+10) (Craig, 1961), that corresponds to equilibrium fractionation during Rayleigh rain-out (Dansgaard, 1964). Local precipitation samples can deviate from this line and a local meteoric water line (LMWL) can be defined by the linear regression of rain sample data (Bowling et al., 2017; Dansgaard, 1964). At our field site, the LMWL had a slope of approximately 7.4 ± 0.3. A slope of the LMWL below 8 might reflect the influence of non-Rayleigh-distillation processes such as local evaporation (from open water bodies) and selective transpiration but also evaporation from falling raindrops (Gat, 2000). However, the LMWL is to be interpreted cautiously, if the underlying rain samples span different seasons (Gat, 1996). Here we use the LMWL and the GMWL only to compare the slopes of the measured isotopic composition of water vapor with these lines. The dual isotope analysis further reveals that the measured δ_v values over the season clustered into

1 Except East African rivers and lakes and waters from closed basins (Craig, 1961)

three groups: Before leaf unfolding on DOY 110, the measured (daily averaged) δ_v values followed the GMWL (with a slope of 8.0 ± 0.2), whereas after leaf senescence on DOY 280, the slope in the δ^{18}O-δD-plane was 7.3 ± 0.1 and thus closer to the LMWL. For the period with green leaves, an even lower slope of 6.9 ± 0.1 was measured. This becomes more visible when deviations from the GMWL and LMWL are plotted versus time (Fig. 4.5). While the GMWL with its slope of 8 seems to describe the variability of δ_v before leave unfolding, the obtained values after leaf senescence in fall are in average better represented by the LMWL, indicating some influence of local conditions or fluxes. Between leaf unfolding and leaf senescence in fall, the variation in the measured difference from both the LMWL and the GMWL shows a seasonal cycle which might be related to seasonal shifts in the source (but in general also in the fractionation) of water vapor.

Other processes that drive the seasonal variability of δ_v could be revealed by testing correlations with other meteorological quantities that are related to entrainment or the isotopic composition of different water pools and fluxes in the ecosystem. Thus we calculated the Pearson correlation coefficient R_{pear} for different meteorological quantities (shown in Table 4.2) such as turbulent kinetic energy TKE or friction velocity u^* (which are related to turbulence and entrainment), as well as temperature, relative humidity RH, vapor pressure deficit VPD and water vapor mole fraction C_{H2O} (which are related to the isotopic composition of different components of the water cycle). We found no indication that the day-to-day variability of δ_v is driven by the variability of entrainment, as we found no significant correlation between δ_v and TKE and u^* (see Table 4.2). For the whole measurement period, the observed seasonal variability of δ_v was strongest correlated to temperature ($R^2 > 0.5\,, p < 10^{-35}$). This correlation was stronger than the correlation to

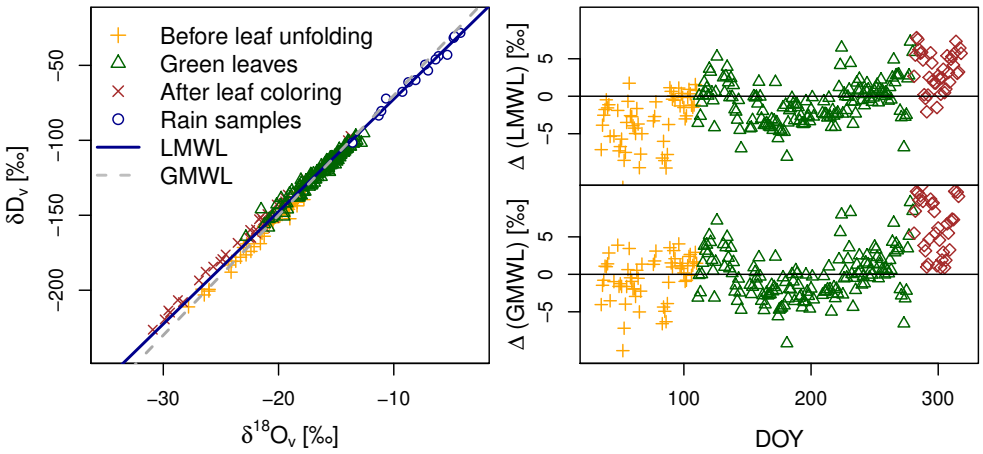

Figure 4.5: Plot of the diurnal averages of the isotopic composition of water vapor in the δ^{18}O-δD-plane in combination with the GMWL and the LMWL (left panel). The right panels show the deviations Δ from the GMWL and LMWL plotted against the day of the year (DOY). Different symbols represent different periods: The period before leaf unfolding (orange crosses), the period with green unfolded leaves (green triangles) and the period after the beginning of leaf senescence in fall (brown diagonal crosses). Before leaf unfolding δ_v fluctuates around the GMWL and after leaf unfolding δ_v gets closer to the LMWL.

$\log(C_{\mathrm{H2O}})$, discussed above as an indicator for Rayleigh distillation processes. In particular, the observed correlation with temperature at a 2 m height above the ground had an R^2 of 0.52 and was slightly stronger than the correlation with temperature at 44 m above the ground for both isotopic species. Similarly, the soil temperature at 2 cm depth is much stronger correlated to δ_v than the soil temperature at 64 cm depth. These height dependencies indicate, that the temperatures close to the surface is an important driver of δ_v. In general, the correlation between temperature and δ_v might be linked to temperature dependent fractionation at the site of evaporation of the measured water vapor. However, the day-to-day-variability is not fully reflected by the obtained correlations of δ_v with temperature and temperature-related quantities such as LWDR, VPD and RH (see Table 4.2). This becomes clearer, when correlations between δ_v and its potential drivers are calculated only for the time period between leaf unfolding and leaf senescence in fall (period: 'green leaves' in Table 4.2). For this time period, the obtained correlations with temperature-related quantities get weaker. The correlation with temperature at a 2 m height is still significant ($p < 10^{-10}$) but has R^2-values of only 0.27 and 0.28 for $\delta\mathrm{D}_v$ and $\delta^{18}\mathrm{O}_v$, respectively. In general, the positive correlation with temperature related quantities implies that fractionation and evaporation might be relevant drivers of δ_v. As we did not find indications that local ET drives the seasonal variability of δ_v, the dominant source of the measured water vapor might be further away, but the temperature during evaporation might still be correlated to the temperature during the measurement.

Table 4.2: Results of the analysis of potential drivers of δ_v for all data points ('all times') and for the period with green unfolded leaves ('green leaves'). For each correlation the Pearson correlation coefficient R_{pear} is given in combination with the significance levels, marked with (*) for $p < 10^{-5}$, (*) for $p < 10^{-10}$, (*) for $p < 10^{-15}$ and so on.

	δD_v		$\delta^{18}O_v$	
	all times	green leaves	all times	green leaves
IF D	-0.08	-0.50 **	-0.07	-0.48 *
IF ^{18}O	-0.26	-0.59 **	-0.25	-0.57 **
Temperature (44 m)	0.71 ****	0.50 *	0.71 ****	0.51 **
Temperature (2 m)	0.72 ****	0.52 **	0.72 ****	0.53 **
Soil temperature (-2 cm)	0.67 ****	0.43 *	0.66 ****	0.45 *
Soil temperature (-64 cm)	0.48 **	0.26	0.44 **	0.25
LWUR	0.71 ****	0.50 *	0.71 ****	0.52 **
LWDR	0.39 *	0.27	0.40 *	0.35
PARD	0.48 **	0.10	0.48 **	0.07
PARU	0.33 *	0.02	0.33 *	-0.00
RH	-0.52 ***	-0.31	-0.51 ***	-0.24
VPD	0.54 ****	0.40 *	0.53 ****	0.36
Log (C_{H2O})	0.59 ****	0.35	0.60 ****	0.41 *
C_{H2O}	0.61 ****	0.40 *	0.62 ****	0.46 *
δD_{ET}	0.65 ****	0.44 *	0.65 ****	0.44 *
$\delta^{18}O_{ET}$	0.32 *	0.17	0.32 *	0.21
TKE	-0.06	-0.17	-0.03	-0.17
u^*	-0.09	-0.19	-0.06	-0.20

4.5 Conclusions

Here we evaluate laser spectroscopic measurements of the isotopic composition of water vapor (δD_v and $\delta^{18}O_v$) in the SBL and local ET (δD_{ET} and $\delta^{18}O_{ET}$) in combination with meteorologic and turbulence-related quantities on a diurnal and on a seasonal timescale above a managed beech forest in central Germany. We found indications that the diurnal cycle of δ_v is alternately dominated by local ET and entrainment, in particular in spring and summer. On a seasonal timescale we found no indication that local ET and entrainment dominate the observed variability. This could be related to the fact, that at this field site, the effects of entrainment and local ET seem to cancel each other out and do not yield seasonal variability. Further, the remaining variability of δ_v over the full growing season can only partly be explained by Rayleigh distillation (linked to approximately 35 % of the variability). This fraction further decreases for the period when green leaves were present (and transpiration is expected). A larger fraction of 50 % of the observed seasonal variability of δ_v was linked to temperature, indicating some influence of temperature related processes, such as fractionation during evaporation from different water pools. We conclude that the temporal variability of the isotopic composition of water vapor in the SBL, even if measured close to a managed beech forest, might not be dominated by local ET on both, diurnal and seasonal timescale. However, the simultaneous measurement of δ_v and δ_{ET} in combination with meteorological and turbulence-related quantities seems a promising approach to increase the understanding of the temporal variability in δ_v.

4.6 Code availability

The EddyPro® sourcecode is available on github.

4.7 Data availability

All data used for the figures presented here is provided in the supplementary material.

4.8 Author contributions

The research presented here was planned, carried out, described and interpreted by Jelka Braden-Behrens, supervised by Alexander Knohl. Both authors read and made editorial comments to the manuscript.

4.9 Competing interests

We declare that we have no conflict of interest.

4.10 Acknowledgements

This project was partly funded by the Dorothea-Schlözer-Fellowship and by the German Research Foundation (DFG, project ISOFLUXES KN 582/7-1). Additionally this work was supported by the European Research Council via the European Union's Horizon 2020 research and innovation programme (grant agreement no. 682512-OXYFLUX). We thank Dave Bowling and Lukas Siebicke for reading and commenting on the manuscript.

CHAPTER 5

Synopsis

5.1 Summary and discussion

In the PhD thesis ´The isotopic composition of CO_2 and H_2O_v fluxes in a managed beech forest' I present two experiments that use high-precise laser spectrometers to measure the isotopic composition of a flux (or flux component) in the coupled CO_2 and H_2O_v cycle above a managed beech forest in central Germany. In the first experiment, the isotopic composition of ecosystem integrated nighttime CO_2 exchange R_{eco}[1] was measured with a spatial Keeling plot approach (see chapter 2). For this experiment, a newly developed laser-based analyzer in mid infrared is used (Delta Ray *Thermo Scientific Inc., Waltham, USA*). In the second experiment, the isotopic composition of evapotranspiration (ET) was measured with the eddy covariance (EC) method (see chapters 3 and 4). For this experiment we used a high flow rate and high-frequency enabled laser-based cavity-enhanced absorption spectrometer in near infrared (2 Hz-HF-WVIA, *Los Gatos Research Inc.*, San Jose, CA, USA). In both experiments the isotopic composition of the respective flux (or flux component) is measured in a dual isotope approach - with measurements of $\delta^{13}C$ and $\delta^{18}O$ for CO_2 for and measurements of δD and $\delta^{18}O$ for H_2O_v.

5.1.1 Instrument tests

For both experiments, a first set of results deals with instrument tests including a detailed evaluation of the calibration strategy. For both analyzers, the calibration strategy needs to address the large and non-linear mole fraction range dependency of the uncalibrated δ values (see Fig. 2.4 for CO_2 and Fig. 3.4 for H_2O_v). The analyzers accuracy (subsequent to the correction of mole fraction range dependency) and its precision (Allan deviation) is quantified for each analyzer. In Table 5.1 the obtained values for precision and accuracy are

Table 5.1: Precision and accuracy for the two different laser-based analyzers used in this study. As a measure of precision, we use the minimal Allan deviation σ_A, whereas potential accuracy is quantified by one standard deviation from the linear fit used for calibration, as defined by Tuzson et al. (2008). The uncertainty estimates of the fluxes are a) the mean value of the standard errors of the Keeling plot intercepts based on 90 min timescale (see section 2.11.1) and b) the propagated Mann and Lenschow flux uncertainties on 60 min timescale (see section 3.4.2.3). All values in this table are in ‰.

	CO_2 analyzer		H_2O_v analyzer	
	$\delta^{13}C$	$\delta^{18}O$	$\delta^{18}O$	δD
Minimal Allan deviation	0.02	0.03	0.02	0.08
Potential accuracy	0.24	0.3	0.16	0.5
Uncertainty estimate (flux)	0.8[a]	0.8[a]	0.5[b]	1[b]
Obtained range (ambient)	-11 to -7	-6 to 2	-33 to -12	-147 to -12
Obtained δ range (flux)	-32 to -26	-46 to -10	-19 to 0	-140 to -25

1 For $\delta^{13}C$ this is respiration, whereas for $\delta^{18}O$, this is respiration after ^{18}O exchange between H_2O and CO_2.

summarized for both analyzers (see also chapters 2 and 3 for a more detailed description). The measured Allan deviations are in the range of minimal Allan deviations and precisions that have been reported for other laser spectrometers (see Tables 1.1 and 2.2). The measured potential accuracy is in the range of an inter-laboratory comparison for H_2O_v (Wassenaar et al., 2012) and in the range of the repeatability of other laser spectrometers for CO_2 (Sturm et al., 2012; Sturm et al., 2013; Vogel et al., 2013). It is worth pointing out that for CO_2 isotope analysis, higher accuracy can be achieved with isotope ratio mass spectrometry (IRMS), as a long-term flask air inter-comparison experiment illustrates (Masarie et al., 2001). However, flask measurements have their own challenges and limitations, such as high costs and sample preparation effort (Griffis, 2013) and potential storage effects. Based on the conducted instrument tests and data analysis in the field, we conclude that both used analyzers are suitable for continuous, precise and accurate field measurements of the respective δ values. This refers to the measurement of $\delta^{13}C$ and $\delta^{18}O$ in CO_2 in case of the Delta Ray analyzer and to the measurement of $\delta^{18}O$ and δD in H_2O_v in the case of the 2 Hz-HF-WVIA.

5.1.2 Evaluation of the applied methods

Not only the instruments, but also the applicability of the used methods needed to be tested. The spatial Keeling plot method has been used by various authors before to measure the isotopic composition of nighttime (and even daytime) net CO_2 fluxes above various ecosystems (see e.g. Barbour et al., 2011; Bowling et al., 2002; Knohl et al., 2005b). However, as the Keeling plot method relies on strong assumptions, we introduced some measures to approve the applicability of these assumptions following recommendations from the literature (discussed in chapter 2.11.1). Examples for these measures are outlier removal and the use of data acquired within a comparably short time period (90 min) for each individual Keeling plot. To further test if the spatial distribution of measurement points influence the calculated Keeling plot intercepts, we compared the intercepts based on including and excluding data from heights below 2 m. Based on this comparison, we found that the inclusion of data from heights below 2 m did not bias the data, but improved the uncertainty of the measured isotopic compositions of R_{eco} by a factor of 2. Thus, we conclude that our Keeling plot setup is capable of measurements of the isotopic composition of nighttime CO_2 exchange. This conclusion is additionally based on the measured repeatability during the field campaign of 0.2 ‰ for $\delta^{13}C$ and below 0.25 ‰ for $\delta^{18}O$ (cf. section 2.4.1.3) and the measured response time below 60 s (cf. section 2.4.1.4).

In contrast to the broad use of Keeling plot measurements of the isotopic composition of (nighttime) CO_2 exchange, eddy covariance measurements of the isotopic composition of ET δ_{ET} on the other hand are very rare. Such measurements have been carried out with a fast analyzer above a corn/soybean canopy (Griffis et al., 2010; Griffis et al., 2011) and with a slow analyzer above a semi-arid savanna (Good et al., 2012). Hence there is currently only one other application that uses an analyzer that is fast enough for EC measurements. The 2 Hz-HF-WVIA used in our setup was newly configured for the purpose of EC measurements of δ_{ET}. Thus, the method and also the setup needed to be evaluated. Based on the observed spectra and cospectra of the turbulent time series, we found that tubing effects were not isotope selective and thus did not compromise measurements of δ_{ET}.

Additionally, the tubing effects of our isotope EC setup were less pronounced than those of a standard EC setup that is routinely used at the field site of our studies. With the spectral correction of high-frequency attenuation according to Moncrieff et al. (1997a), we obtained an underestimation of the measured net H_2O_v fluxes of only 6 % if compared to the standard EC measurements at the same site. Based on spectral analysis and a good agreement of the measured net fluxes to a standard EC system at this field site, we conclude that our EC setup is capable to measure δ_{ET}.

5.1.3 Specific features of the obtained seasonal variability

With the two different laser-based spectrometers and ecosystem scale methods, we measured the isotopic composition of different parts of the coupled CO_2 and H_2O cycle at our field site at a managed beech forest in central Germany. During a field experiment in autumn 2015, we measured the $\delta^{13}C$ and $\delta^{18}O$ composition of nighttime CO_2 exchange R_{eco} (chapter 2) and throughout the year 2016, we measured the $\delta^{18}O$ and δD composition of evapotranspiration δ_{ET}, see chapter 3. The obtained seasonal[1] variability of R_{eco} and δ_{ET} exceeds the corresponding uncertainty and is considerably larger than the variability in the measured atmospheric δ values (see Table 5.1).

The time series of the isotopic composition of nighttime CO_2 fluxes shows particularly different features for $\delta^{13}C$ and $\delta^{18}O$. The obtained difference in the characteristics of $\delta^{13}C$ and $\delta^{18}O$ are expected due to the different underlying processes: While the $\delta^{13}C$ composition of respiration can be related to photosynthetic discrimination of the heavier ^{13}C isotope and all drivers of autotrophic and heterotrophic respiration, the $\delta^{18}O$ composition is controlled by oxygen exchange between H_2O and CO_2, when CO_2 gets dissolved in water (see e.g. Miller et al., 1999). However, one particularly strong feature in the measured $R^{18}_{eco}O$ is a sharp decrease of about 30 ‰ within 10 days after an early snow event in October 2015. Subsequent to this sharp decrease, it took three weeks for $R^{18}_{eco}O$ to recover. Based on this observation, we conclude that even short snow or frost events might have substantial effects on the $\delta^{18}O$ composition of CO_2. The time series of the $\delta^{13}C$ composition showed a more complex behavior which is discussed under consideration of meteorological drivers in the next section.

The time series of the isotopic composition of water vapor and ET showed a clear and continuous (potentially temperature related) seasonal cycle for both isotopologues. A plot of the two measured isotopic compositions of ET in the $\delta^{18}O$-δD-plane in combination with the measured isotopic compositions of precipitation and water vapor illustrates the benefits of dual isotope approaches (see Fig. 5.1). In the $\delta^{18}O$-δD-plane, the measured isotopic compositions can be compared to the local meteoric water line (LMWL) based on a linear fit of the isotopic compositions of precipitation samples. The data presented in this thesis shows that the isotopic composition of ET falls below the LMWL when ET is dominated by evaporation (i.e. before leaf unfolding and after leaf coloring), indicating the influence of non-equilibrium fractionation. In the period after leaf unfolding and before leaf coloring,

1 The field campaign was three months long for the Keeling plot measurement of the isotopic composition of nighttime CO_2 flux (respiration). For the EC measurement of the isotopic composition of ET, the field campaign was nine months long.

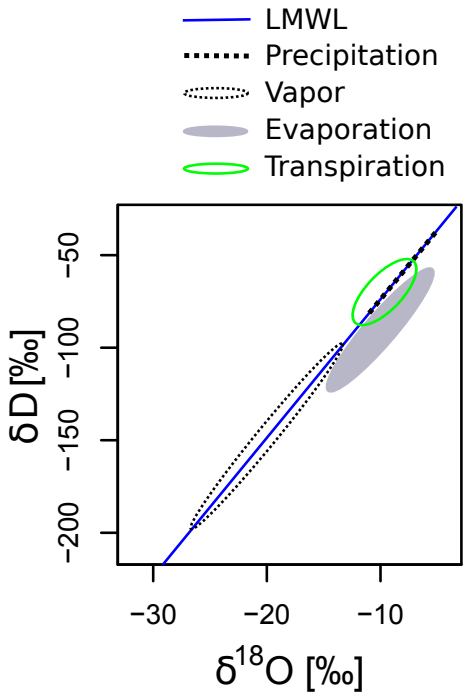

Figure 5.1: True-to-scale drawing of the measured isotopic compositions of water vapor, precipitation, evaporation-dominated and transpiration-dominated evapotranspiration in the δ^{18}O-δD-plane in combination with the local meteoric water line (LMWL, based on all precipitation samples). Here the transpiration-dominated period is defined as the time between leaf unfolding and leaf coloring, whereas the other times are evaporation-dominated. The transpiration-dominated flux follows the LMWL, indicating no kinetic fractionation during transpiration. The evaporation-dominated flux on the other hand falls clearly below the LMWL, due to the importance of kinetic fractionation during evaporation.

the measured isotopic composition of ET fluctuates around the LMWL, indicating that transpiration under steady state conditions dominates ET during this period.

5.1.4 Correlations with potential (meteorological) drivers

We used the measured isotopic compositions of a) nighttime CO_2 flux and b) local ET in combination with the observed meteorological, isotopic and turbulence-related quantities to achieve a better understanding of the underlying processes. This analysis focuses on two main questions, as discussed below:.

- **In how far can we explain the variability of the ^{13}C isotopic composition of respiration by the isotopic composition of recent assimilates which is in turn controlled by meteorological drivers during photosynthesis?**
  We address this question for the measurement period in autumn 2015 before the first snow, when the ecosystem was a net CO_2 sink. For this time period, the measured ^{13}C composition of respiration is significantly ($p<10^{-4}$) correlated with time-lagged net radiation. The time lag of this correlation is 2-5 days, which is consistent to the expected time lag between assimilation and respiration (Kuzyakov et al., 2010). As net radiation is a driver of photosynthesis and photosynthetic discrimination of ^{13}C, we suggested the hypothesis that the isotopic composition of respiration is related to the isotopic composition of recent assimilates. We tested this hypothesis by using an iterative biophysical multilayer model to calculate the isotopic composition of recent assimilates and evaluated its correlation with net radiation. This comparison shows that the time lagged measured isotopic composition of respiration and the modeled isotopic composition of recent assimilates correlate with net radiation in the opposite

way. Thus, we discarded the hypothesis that the observed correlation between $R^{13}_{\mathrm{eco}}\mathrm{C}$ and net radiation reflects a link of the isotopic composition of respiration to the isotopic composition of recent assimilates. As an alternative, we discuss the hypothesis that the measured correlation is related to changes in the amount of recent (autotrophic) assimilates rather than to their isotopic composition. Based on a comparison with literature data, we find that this second hypothesis might be true, but we could not prove it without additional independent measurements.

- **Does local evapotranspiration (ET) drive the diurnal and seasonal variability of the isotopic composition of water vapor δ_v in the surface boundary layer (SBL) above a managed beech forest?**
  On diurnal timescale, we found no evidence that δ_v above the managed beech forest is dominantly controlled by local ET. The obtained diurnal cycles of isoforcing (IF), the isotopic composition of water vapor δ_v, the water vapor concentration C_{H2O} and the turbulent kinetic energy (TKE) rather support the hypothesis that the diurnal cycles of δ_v are alternately driven by entrainment and ET, particularly in spring and summer. This is consistent with previous studies above various ecosystems (Huang et al., 2014; Lee et al., 2012a; Welp et al., 2008; Zhang et al., 2011). Further, we find no evidence that local ET drives the temporal variability on seasonal timescale. This is also the case for the time when green leaves are present and transpiration dominates over evaporation. This result is based on correlating the directly measured isoforcing values with δ_v. Instead of a positive correlation, we find a negative correlation between these quantities. However, this correlation should not be over-interpreted, in particular because we find a stronger correlation between δ_v and surface temperature, indicating an important influence of temperature-related processes (such as fractionation at the site of evaporation of the measured water vapor). The fact that we do not see evidence for a dominant control of δ_v by local ET does not match with the expectations that we developed based on other studies (Griffis et al., 2016; Huang et al., 2014) and from the fact we measured δ_v very close to the forest canopy.

5.2 The broader context: Dual isotope and dual species approaches

In both experiments presented in this thesis, we simultaneously measured two different δ values of a molecule, which we refer to as a dual isotope approach. In the Keeling plot application (see chapter 2) we use the Delta Ray IRIS to measure $\delta^{13}\mathrm{C}$ and $\delta^{18}\mathrm{O}$ in CO_2, whereas in the eddy covariance application (see chapters 3 and 4) we use the 2 Hz-HF-WVIA to measure $\delta\mathrm{D}$ and $\delta^{18}\mathrm{O}$ in H_2O_v. In both cases, the dual isotope approach provide improved opportunities to investigate the underlying processes. Even broader than a dual isotope approach is the simultaneous measurement of isotopic compositions in different molecules (isotopic dual species approach).

5.2.1 Dual isotope approaches in this thesis

In the Keeling plot application the dual isotope approach enabled us to simultaneously analyze two different processes: a) We investigated how the $^{13}\mathrm{C}$ discrimination during photosynthesis is reflected in the temporal variability of the $^{13}\mathrm{C}$ composition of respiration;

b) We measured how the $\delta^{18}O$ composition, reflecting the isotopic exchange between CO_2 and H_2O reacted to an early snow event. For future research, the response of the $\delta^{18}O$ measurements of nighttime CO_2 exchange would be interesting to analyze in a dual species approach in combination with measurements of the isotopic composition of soil water and snow. Thus, by analyzing $\delta^{18}O$ in CO_2 we can get deeper understanding of the exchange of oxygen between CO_2 and different water pools. In the eddy covariance approach, the dual isotope analysis of $\delta^{18}O_{ET}$ and δD_{ET} enabled us to get a clear separation of evaporation-dominated and transpiration-dominated periods in the $\delta^{18}O$-δD-plane. An analysis of the temporal variability of δ_{ET} in this plane is particularly interesting, because it allows to analyze the importance of non-equilibrium processes.

5.2.2 Dual isotope approaches in related work

There are multiple dual isotope or even isotopic dual species approaches that use the additional information obtained by measuring different isotopic compositions for various applications. Some of these applications are discussed in the next paragraph and shown in Table 5.2 to highlight the broad range of dual isotope and dual species applications. An evident application of dual isotope or dual species approaches is the simultaneous use of two isotopes to improve existing partitioning estimates by expanding an existing two component mixing model to three components (Blagodatskaya et al., 2011; Phillips et al., 2001). However, a frequently used dual isotope approach is the the simultaneous analysis of $\delta^{18}O$ and δD in precipitation (Ambach et al., 1968; Dansgaard, 1964). Similarly, measurements of $\delta^{18}O$ and δD in water vapor (Griffis et al., 2016; Welp et al., 2012) provided insights into the potential drivers of δ_v. Further, the depth (Meissner et al., 2014) or the source and structure (Bowling et al., 2017) of the water pools used by plants has been discussed based on $\delta^{18}O$ and δD measurements of different water pools (such as snow, xylem, soil, stream and ground water).

In the case of CO_2 measurements, dual isotope approaches have been used for example to study the effects of elevated CO_2 and higher temperature on different components of soil respiration (Lin et al., 1999). An application of a dual species approach is the simultaneous study of $\delta^{18}O$ in H_2O and CO_2. With such an approach, the CO_2 hydration efficiency was evaluated with chamber-based (Wingate et al., 2009) and eddy covariance (Griffis et al., 2011) techniques. Further, the inclusion of measurements of accelerated CO_2 hydration rates into global modeling simulations improved global C^{826}_{CO2} budget estimations (Wingate et al., 2009).

Further, a notable dual isotope and dual species application in the broader context of this thesis focuses on the effect of turbulence on kinetic fractionation based on two experiments at two sites with different surface roughnesses (Lee et al., 2009). One of the two experiments that underly the study of Lee et al. (2009) is based on flux gradient measurements of $\delta^{18}O$ of ET (cf. Welp et al., 2008) in combination with EC measurements of $\delta^{18}O$ and $\delta^{13}C$ in net CO_2 exchange (cf. Griffis et al., 2008) above a soybean canopy. The second experiment that is used in the study of Lee et al. (2009) is based on flux gradient measurements of $\delta^{18}O$ of ET without direct measurements of $\delta^{18}O$ and $\delta^{13}C$ in net CO_2 exchange. Both experiments also include water sampling (precipitation, soil, xylem and in case of the soybean experiment also leaf water) and an application of the

Table 5.2: Examples for dual isotope or even dual species approaches in this thesis and in related literature.

Study	Focus	H_2O		CO_2	
		δD	δ^{18}O	δ^{13}C	δ^{18}O
Dansgaard, 1964	precipitation	√	√		
Bowling et al., 2017	plant's water use	√	√		
Meissner et al., 2014	plant's water use	√	√		
Welp et al., 2012	drivers of δ_v	√	√		
Griffis et al., 2016	drivers of δ_v	√	√		
Thesis chapter 3	variability of δ_{ET}	√	√		
Thesis chapter 4	drivers of δ_v	√	√		
Lin et al., 1999	drivers of respiration components			√	√
Thesis chapter 2	variability of respiration			√	√
Griffis et al., 2011	CO_2 hydration		√		√
Wingate et al., 2009	CO_2 hydration		√		√
Wingate et al., 2008	CO_2 hydration		√		√
Lee et al., 2009	canopy-scale fractionation		√	√	√

Craig-Gordon model. Based on these measurements, Lee et al. (2009) conclude that turbulence enhances kinetic fractionation at the ecosystem scale, in particular for δ^{18}O in CO_2. Further, their results imply that surface roughness might play an important role in the C^{826}_{CO2} budget. In this context, EC measurements of δ^{18}O in ET, as presented in this thesis could provide new possibilities to further evaluate these fractionation effects in particular above rough canopies (when flux gradient measurements are less reliable).

5.3 Outlook and future work

The two newly configured and newly developed laser-based spectrometers presented in this thesis are examples of instruments that are capable of dual isotope analysis. With further developments in laser-based measurement systems, a more frequent use of such instruments seems promising. However, this thesis presents two separate experiments that measure each two isotopic compositions in the coupled CO_2 and H_2O_v cycle. As a short overview about dual isotopes in related literature suggests, dual isotope approaches can help to answer various questions about the underlying exchange processes and drivers. A possible next step on the basis of the research presented in this thesis is a further evaluation of the measured isotopic composition of the respective net fluxes in combination with the isotopic composition of different pools and flux components in the respective cycle. In case of the Keeling plot measurements of R^{18}_{eco}O and R^{13}_{eco}C, such measurements would be

interesting in combination with measurements of the isotopic composition of autotrophic and total soil respiration (e.g. with a trenching experiment). These measurements could further help to test hypothesis 2 of chapter 2 of this thesis, which relates the observed time-lagged correlation between net radiation and $R^{13}_{eco}C$ to the ratio of autotrophic to total soil respiration. In case of the eddy covariance measurements of δ_{ET}, there are various possible applications that could make use of dual isotope EC measurements on an ecosystem scale. One of these applications is a combination of these measurements with chamber measurements and/or modeling approaches to partition ET into evaporation and transpiration when flux gradient approaches show limited applicability (e.g. above tall ecosystems, see e.g. Griffis, 2013). A combination of EC measurements for $\delta^{13}C$ and $\delta^{18}O$ in CO_2 and $\delta^{18}O$ H_2O fluxes would be particularly interesting to further investigate roughness effects on turbulent kinetic fractionation on canopy scale, as discussed by Lee et al. (2009). Similarly, it would be interesting to evaluate the CO_2 hydration efficiency over the full growing season of the forest ecosystem directly on an ecosystem scale. This would be possible if EC measurements of $\delta^{18}O_{ET}$ are combined with measurements of $\delta^{18}O$ in (daytime and nighttime) net CO_2 exchange, similar to the 74 days long experiment by Griffis et al. (2011).

5.4 General conclusions

This thesis illustrates that dual isotope approaches have a large potential to improve our understanding of ecosystem-atmosphere CO_2 and H_2O exchange processes. Particularly on the ecosystem scale, this potential is enhanced by the development of field applicable, commercially available instruments capable of simultaneous analysis of different isotopic compositions. In this thesis we demonstrate field applicability and evaluate instrument characteristics for two laser-based analyzers that are capable of dual isotope analysis. The ability for dual isotope analysis, in combination with the measured instrument characteristics such as precision and accuracy shows, that these analyzers can compete with other laser-based spectrometers or even with flask-based IRMS surveys. In case of the CO_2 analyzer, stable repeatability, field applicability, automatic internal calibration and limited maintenance effort of the instrument provides opportunities for a broad utilization of this instrument. Thus, we conclude that the analyzer is suitable for various field applications in particular at remote sites. Concerning the EC measurements of δ_{ET} the used analyzer is currently the only commercially available instrument for measurements of $\delta^{13}C$ and δD with a high (>2 Hz) measurement frequency. This analyzer provides exciting new opportunities for ET-studies above tall ecosystems. With a median uncertainty of 0.5 and 1 ‰ for $\delta^{18}O$ and δD, respectively, our uncertainty estimate for δ_{ET} is comparable with different uncertainty estimates of various flux gradient approaches. This proves that EC measurements of δ_{ET} can complement or even compete with flux gradient approaches. A broader application of laser-based spectrometers, capable of dual isotope analysis, has great potential to improve our understanding of the coupled CO_2 and H_2O_v cycle.

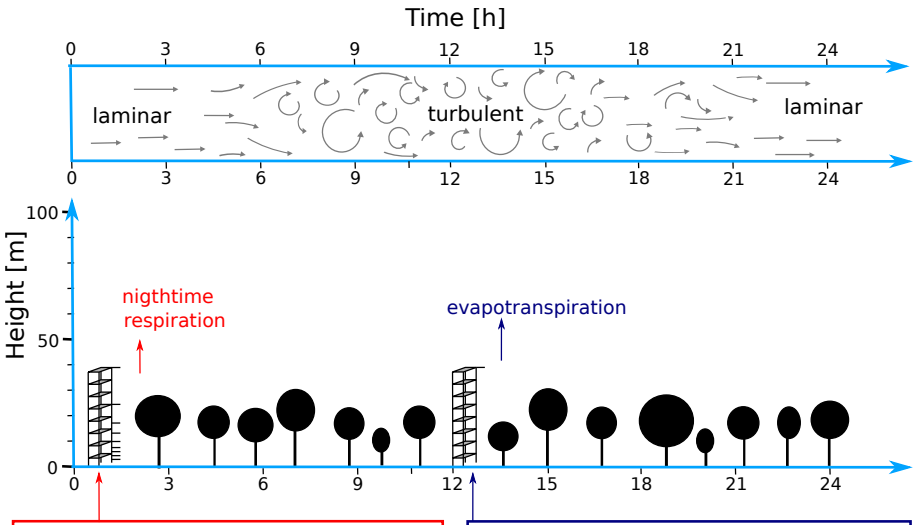

MAIN CONCLUSIONS
EXPERIMENT 1 (chapter 2)

Instrument tests:
- The internally calibrated instrument showed comparably high precision and accuracy for measurements of C_{H2O}, $\delta^{13}C$ and $\delta^{18}O$ in air.

Ecological application:
- Single snow events can strongly influence the isotopic imprint of terrestrial ecosystems on atmospheric CO_2.
- The $\delta^{13}C$ composition of respiration is not related to the isotopic composition of assimilation via the Farquar model.

MAIN CONCLUSIONS
EXPERIMENT 2 (chap. 3 & 4)

Instrument tests:
- The instrument showed comparably high precision and accuracy for $\delta^{18}O_v$ and δD_v measurements and is capable of EC measurements of $\delta^{18}O$ and δD of ET.

Ecological application:
- In the $\delta^{18}O$-δD-plane, we can distinguish between periods dominated by evaporation or transpiration.
- Local ET does not dominate the measured diurnal and seasonal variability of $\delta^{18}O_v$ and δD_v in the SBL.

GENERAL CONCLUSIONS

- The development of field applicable dual isotope instruments enhances the potential of dual isotope approaches to study CO_2 and H_2O exchange processes.

- Various field experiments with laser-based analyzers capable of dual isotope analysis can provide new opportunities to study the coupled CO_2 and H_2O_v cycle.

Figure 5.2: Main thesis conclusions.

Bibliography

Aemisegger, F., P. Sturm, P. Graf, H. Sodemann, S. Pfahl, A. Knohl, and H. Wernli (2012): 'Measuring variations of $\delta^{18}O$ and $\delta^{2}H$ in atmospheric water vapour using two commercial laser-based spectrometers: An instrument characterisation study'. *Atmospheric Measurement Techniques*, vol. 5(7): pp. 1491–1511 (cit. on pp. 9, 10, 63, 64, 70, 94).

Affek, H. and D. Yakir (2014): 'The stable isotopic composition of atmospheric CO_2'. *Treatise on geochemistry*. Ed. by Holland, H. and K. Turekian. 2nd ed. Vol. 5. Elsevier. Chap. 5.7: pp. 179–212 (cit. on pp. 2, 16).

Alstad, K., C.-T. Lai, L. B. Flanagan, and J. R. Ehleringer (2007): 'Environmental controls on the carbon isotope composition of ecosystem-respired CO_2 in contrasting forest ecosystems in Canada and the USA'. *Tree Physiology*, vol. 27(10): pp. 1361–1374 (cit. on p. 5).

Ambach, W., W. Dansgaard, H. Eisner, and J. Møller (1968): 'The altitude effect on the isotopic composition of precipitation and glacier ice in the Alps'. *Tellus*, vol. 20(4): pp. 595–600 (cit. on pp. 3, 91, 113).

Anthoni, P., A. Knohl, C. Rebmann, A. Freibauer, M. Mund, W. Ziegler, O. Kolle, and E. D. Schulze (2004): 'Forest and agricultural land-use-dependent CO_2 exchange in Thuringia, Germany'. *Global Change Biology*, vol. 10(12): pp. 2005–2019 (cit. on pp. 21, 26, 59, 69, 94, 95).

Aubinet, M, J. A. Elbers, J Moncrieff, A Grelle, A Ibrom, R Clement, T Foken, A Ibrom, J Moncrieff, K Pilegaard, Ü Rannik, and C Rebmann (2003): 'Methodology for Data Acquisition, Storage, and Treatment'. *Fluxes of Carbon, Water and Energy of European Forests*. Ed. by Valentini, R. Vol. 163. Berlin, Heidelberg: Springer Berlin Heidelberg: pp. 9–35 (cit. on p. 61).

Baldocchi, D. (2003): 'Assessing the eddy covariance technique for evaluating carbon dioxide exchange rates of ecosystems: past, present and future'. *Global Change Biology*, vol. 9(4): pp. 479–492 (cit. on pp. 7, 60).

– (1997): 'Measuring and modelling carbon dioxide and water vapour exchange over a temperate broad-leaved forest during the 1995 summer drought'. *Plant, Cell and Environment*, vol. 20(9): pp. 1108–1122 (cit. on p. 28).

Baldocchi, D., K. B. Wilson, and L. Gu (2002): 'How the environment, canopy structure and canopy physiological functioning influence carbon, water and energy fluxes of a temperate broad-leaved deciduous forest - An assessment with the biophysical model CANOAK.' *Tree physiology*, vol. 22(15-16): pp. 1065–1077 (cit. on p. 28).

Baldocchi, D. and K. B. Wilson (2001): 'Modelling CO_2 and water vapor exchange of a temperate broadleaved forest across hourly to decadal time scales'. *Ecological Modelling*, vol. 142(1-2): pp. 155–184 (cit. on p. 28).

Baldocchi, D. and D. R. Bowling (2003): 'Modelling the discrimination of $^{13}CO_2$ above and within a temperate broad-leaved forest canopy on hourly to seasonal time scales'. *Plant, Cell and Environment*, vol. 26: pp. 231–244 (cit. on p. 28).

Baldocchi, D., J. D. Fuentes, D. R. Bowling, A. A. Turnipseed, and R. K. Monson (1999): 'Scaling isoprene fluxes from leaves to canopies: Test cases over a boreal aspen and a mixed species temperate forest'. *Journal of Applied Meteorology*, vol. 38(7): pp. 885–898 (cit. on p. 28).

Baldocchi, D., C. A. Vogel, and B. Hall (1997): 'Seasonal variation of carbon dioxide exchange rates above and below a boreal jack pine forest'. *Agricultural and Forest Meteorology*, vol. 83(1): pp. 147–170 (cit. on p. 28).

Ballantyne, A. P., J. B. Miller, I. T. Baker, P. P. Tans, and J. W. C. White (2011): 'Novel applications of carbon isotopes in atmospheric CO_2: What can atmospheric measurements teach us about processes in the biosphere?' *Biogeosciences*, vol. 8(10): pp. 3093–3106 (cit. on p. 17).

Barbour, M. M., J. E. Hunt, N. Kodama, J. Laubach, T. M. McSeveny, G. N. D. Rogers, G. Tcherkez, and L. Wingate (2011): 'Rapid changes in $\delta^{13}C$ of ecosystem-respired CO_2 after sunset are consistent with transient ^{13}C enrichment of leaf respired CO_2'. *New phytologist*, vol. 190(4): pp. 990–1002 (cit. on pp. 5, 17, 109).

Blagodatskaya, E., T. Yuyukina, S. Blagodatsky, and Y. Kuzyakov (2011): 'Three-source-partitioning of microbial biomass and of CO_2 efflux from soil to evaluate mechanisms of priming effects'. *Soil Biology and Biochemistry*, vol. 43(4): pp. 778–786 (cit. on p. 113).

Bolin, B. (1959): 'On the use of tritium as a tracer for water in nature'. *Proc. 2nd Conf. on the Peaceful Uses of Atomic Energy*. Geneva: UN: 18:336–44 (cit. on p. 44).

Bowling, D. R., N. G. McDowell, B. J. Bond, B. E. Law, and J. R. Ehleringer (2002): '^{13}C content of ecosystem respiration is linked to precipitation and vapor pressure deficit'. *Oecologia*, vol. 131(1): pp. 113–124 (cit. on pp. 5, 6, 17, 40, 109).

Bowling, D. R., D. E. Pataki, and J. T. Randerson (2008): 'Carbon isotopes in terrestrial ecosystem pools and CO_2 fluxes'. *New Phytologist*, vol. 178(1): pp. 24–40 (cit. on p. 42).

Bowling, D. R., S. P. Burns, T. J. Conway, R. K. Monson, and J. W. C. White (2005): 'Extensive observations of CO_2 carbon isotope content in and above a high-elevation subalpine forest'. *Global Biogeochemical Cycles*, vol. 19(3): GB3023 (cit. on pp. 9, 48).

Bowling, D. R., N. G. McDowell, J. M. Welker, B. J. Bond, B. E. Law, and J. R. Ehleringer (2003a): 'Oxygen isotope content of CO_2 in nocturnal ecosystem respiration: 1. Observations in forests along a precipitation transect in Oregon, USA'. *Global Biogeochemical Cycles*, vol. 17(4): pp. 3101–3114 (cit. on pp. 6, 17, 47).

– (2003b): 'Oxygen isotope content of CO_2 in nocturnal ecosystem respiration: 2. Short-term dynamics of foliar and soil component fluxes in an old-growth ponderosa pine forest'. *Global Biogeochemical Cycles*, vol. 17(4): GB2082 (cit. on pp. 6, 43).

Bowling, D. R., P. P. Tans, and R. K. Monson (2001): 'Partitioning net ecosystem carbon exchange with isotopic fluxes of CO_2'. *Global Change Biology*, vol. 7(2): pp. 127–145 (cit. on pp. 4, 16).

Bowling, D. R., E. S. Schulze, and S. J. Hall (2017): 'Revisiting streamside trees that do not use stream water: Can the two water worlds hypothesis and snowpack isotopic effects explain a missing water source?' *Ecohydrology*, vol. 10: e1771 (cit. on pp. 59, 81, 101, 113, 114).

Bowling, D. R., S. D. Sargent, B. D. Tanner, and J. R. Ehleringer (2003c): 'Tunable diode laser absorption spectroscopy for stable isotope studies of ecosystem-atmosphere CO_2 exchange'. *Agricultural and Forest Meteorology*, vol. 118(1-2): pp. 1–19 (cit. on pp. 9, 20).

Braden-Behrens, J. and A. Knohl (2018a): 'Does local evapotranspiration drive seasonal and diurnal variations in the isotopic composition of water vapor in the surface boundary layer above a managed beech forest?' *to be submitted to Biogeosciences*, vol. in prep. (Cit. on p. 89).

Braden-Behrens, J., Y. Yan, and A. Knohl (2017a): 'A new instrument for stable isotope measurements of ^{13}C and ^{18}O in CO_2 - instrument performance and ecological application of the Delta Ray IRIS analyzer'. *Atmospheric Measurement Techniques*, vol. 10(11): pp. 4537–4560 (cit. on pp. 12, 15, 46, 94).

Braden-Behrens, J., C. Markwitz, and A. Knohl (2018b): 'Eddy covariance measurements of the isotopic composition of evapotranspiration'. *to be submitted to Agricultural and Forest Meteorology*, vol. in prep. (Cit. on pp. 12, 55, 94, 95).

Braden-Behrens, J., A. Knohl, H.-J. Jost, and M. Mandic (2017b): 'Measuring the isotopic composition of ecosystem respiration in a temperate beech forest'. *Thermo Scientific White Paper*, vol.: WP30385 (cit. on pp. 13, 21, 46).

Cai, M. Y., L. Wang, S. D. Parkes, J. Strauss, M. F. McCabe, J. P. Evans, and A. D. Griffiths (2015): 'Stable water isotope and surface heat flux simulation using ISOLSM: Evaluation against in-situ measurements'. *Journal of Hydrology*, vol. 523: pp. 67–78 (cit. on pp. 8, 10).

Cappa, C. D., M. B. Hendricks, D. J. DePaolo, and R. C. Cohen (2003): 'Isotopic fractionation of water during evaporation'. *Journal of Geophysical Research*, vol. 108(D16): p. 4525 (cit. on p. 81).

Carbone, M. S., A. D. Richardson, M. Chen, E. A. Davidson, H. Hughes, K. E. Savage, and D. Y. Hollinger (2016): 'Constrained partitioning of autotrophic and heterotrophic respiration reduces model uncertainties of forest ecosystem carbon fluxes but not stocks'. *Journal of Geophysical Research: Biogeosciences*, vol. 121(9): pp. 2476–2492 (cit. on p. 42).

Ciais, P., P. P. Tans, J. W. C. White, M. Trolier, R. J. Francey, J. A. Berry, D. R. Randall, P. J. Sellers, J. G. Collatz, and D. S. Schimep (1995): 'Partitioning of ocean and land uptake of COz as inferred by measurements from the NOAA Climate Monitoring and Diagnostics Laboratory Global Air Sampling Network'. *Journal of Geophysical Research*, vol. 100(20): pp. 5051–5070 (cit. on p. 4).

Conway, T. J., P. P. Tans, L. S. Waterman, K. W. Thoning, D. R. Kitzis, K. A. Masarie, and N. Zhang (1994): 'Evidence for interannual variability of the carbon cycle

from the National Oceanic and Atmospheric Administration/Climate Monitoring and Diagnostics Laboratory Global Air Sampling Network'. *Journal of Geophysical Research*, vol. 99(D11): pp. 22831–22855 (cit. on p. 4).

Coplen, T. B. (2011): 'Guidelines and recommended terms for expression of stable-isotope-ratio and gas-ratio measurement results'. *Rapid Communications in Mass Spectrometry*, vol. 25(17): pp. 2538–2560 (cit. on pp. 4, 17, 58, 59).

Craig, H. and L. Gordon (1965): 'Deuterium and oxygen 18 variations in the ocean and the marine atmosphere'. *Stable Isotopes in Oceanographic Studies and Paleotemperatures*. Ed. by E., T. Pisa: Consiglio nationale delle ricerce laboratorio di geologia nucleare. Chap. 1: pp. 9–130 (cit. on p. 4).

Craig, H. (1961): 'Isotopic variations in meteoric waters'. *Science*, vol. 133(3465): pp. 1702–1703 (cit. on p. 101).

Dansgaard, W. (1964): 'Stable isotopes in precipitation'. *Tellus*, vol. 16(4): pp. 436–468 (cit. on pp. 59, 81, 83, 91, 101, 113, 114).

Dawson, T. E., S Mambelli, A. H. Plamboek, P. H. Templer, and K. P. Tu (2002): 'Stable isotopes in plant ecology'. *Annual Review of Ecology and Systematics*, vol. 33(1): pp. 507–559 (cit. on pp. 4, 56).

De Biévre, P., M. Gallet, N. E. Holden, and I. L. Barnes (1984): 'Isotopic abundances and atomic weights of the elements'. *Journal of Physical and Chemical Reference Data*, vol. 13(3): pp. 809–891 (cit. on p. 60).

Denmead, O. and E. Bradley (1985): 'Flux-gradient relationships in a forest canopy'. *The Forest-Atmosphere Interaction*. Dordrecht: D. Reidel Publishing Company: pp. 421–422 (cit. on p. 6).

Deutscher Wetterdienst (1976): *Aspirations- Psychrometer-Tafeln*. 5th ed. Braunschweig: Friedrich Vieweg und Sohn Verlagsgemeinschaft mbH (cit. on p. 67).

Dubbert, M., M. Cuntz, A. Piayda, and C. Werner (2014): 'Oxygen isotope signatures of transpired water vapor: The role of isotopic non-steady-state transpiration under natural conditions'. *New Phytologist*, vol. 203(4): pp. 1242–1252 (cit. on p. 4).

Dubbert, M., M. Cuntz, A. Piayda, C. Maguás, and C. Werner (2013): 'Partitioning evapotranspiration - Testing the Craig and Gordon model with field measurements of oxygen isotope ratios of evaporative fluxes'. *Journal of Hydrology*, vol. 496: pp. 142–153 (cit. on p. 5).

Ekblad, A. and P. Högberg (2001): 'Natural abundance of ^{13}C in CO_2 respired from forest soils reveals speed of link between tree photosynthesis and root respiration'. *Oecologia*, vol. 127(3): pp. 305–308 (cit. on pp. 5, 17, 40).

Ellehoj, M. D., H. C. Steen-Larsen, S. J. Johnsen, and M. B. Madsen (2013): 'Ice-vapor equilibrium fractionation factor of hydrogen and oxygen isotopes: Experimental investigations and implications for stable water isotope studies'. *Rapid Communications in Mass Spectrometry*, vol. 27(19): pp. 2149–2158 (cit. on p. 4).

Esler, M. B., D. W. T. Griffith, S. R. Wilson, and L. P. Steele (2000): 'Precision trace gas analysis by FT-IR spectroscopy. 2. The $^{13}C/^{12}C$ isotope ratio of CO_2'. *Analytical Chemistry*, vol. 72(1): pp. 216–221 (cit. on p. 17).

Farquhar, G. D., J. R. Ehleringer, and K. T. Hubick (1989): 'Carbon isotope discrimination and photosynthesis'. *Annu. Rev. Plant Phys.* Vol. 40(1): pp. 503–537 (cit. on pp. 4, 40).

Farquhar, G. D. and T. D. Sharkey (1982): 'Stomatal conductance and photosynthesis'. *Annu. Rev. Plant Physiol.* Vol. 33(1): pp. 317–345 (cit. on p. 41).

Farquhar, G. D., J. Lloyd, J. A. Taylor, L. B. Flanagan, J. P. Syvertsen, K. T. Hubick, S. C. Wong, and J. R. Ehleringer (1993): 'Vegetation effects on the isotope composition of oxygen in atmospheric CO_2'. *Nature*, vol. 363(6428): pp. 439–443 (cit. on p. 43).

Fassbinder, J. J., T. J. Griffis, and J. M. Baker (2012): 'Interannual, seasonal, and diel variability in the carbon isotope composition of respiration in a C_3/C_4 agricultural ecosystem'. *Agricultural and Forest Meteorology*, vol. 153(January 2017): pp. 144–153 (cit. on p. 5).

Flanagan, L. B. and J. R. Ehleringer (1998): 'Ecosystem–atmosphere CO_2 exchange: interpreting signals of change using stable isotope ratios'. *Trends in Ecology & Evolution*, vol. 13(1): pp. 10–14 (cit. on p. 16).

Foken, T. and B. Wichura (1996): 'Tools for quality assessment of surface-based flux measurements'. *Agricultural and Forest Meteorology*, vol. 78(1-2): pp. 83–105 (cit. on pp. 7, 60).

Friedman, I., L. Machta, and R. Soller (1962): 'Water-vapor exchange between a water droplet and its environment'. *Journal of Geophysical Research*, vol. 67(7): pp. 2761–2766 (cit. on p. 44).

Galewsky, J., H. C. Steen-Larsen, R. D. Field, J. Worden, C. Risi, and M. Schneider (2016): 'Stable isotopes in atmospheric water vapor and applications to the hydrologic cycle'. *Reviews of Geophysics*, vol. 54(4): pp. 809–865 (cit. on p. 5).

Gat, J. R. (1996): 'Oxygen and hydrogen isotopes in the hydrologic cycle'. *Annu. Rev. Earth Planet. Sci.* Vol. 24: pp. 225–262 (cit. on pp. 44, 56, 81, 83, 90–92, 101).

Gat, J. R. (2000): 'Atmospheric water balance - the isotopic perspective'. *Hydrological Processes*, vol. 14(8): pp. 1357–1369 (cit. on pp. 81, 90, 92, 101).

Geldern, R. V., M. E. Nowak, M. Zimmer, A. Szizybalski, A. Myrttinen, J. A. C. Barth, and H.-J. Jost (2014): 'Field-based stable isotope analysis of carbon dioxide by mid-infrared laser spectroscopy for carbon capture and storage monitoring'. *Analytical Chemistry*, vol. 86(24): pp. 12191–12198 (cit. on pp. 9, 19, 20, 29).

Gemery, P. A., M. Trolier, and J. W. C. White (1996): 'Oxygen isotope exchange between carbon dioxide and water following atmospheric sampling using glass flasks'. *Journal of Geophysical Research*, vol. 101(D9): pp. 14415–14420 (cit. on p. 17).

Gentsch, L., P. Sturm, A. Hammerle, R. Siegwolf, L. Wingate, J. Ogée, T. Baur, P. Plüss, M. Barthel, N. Buchmann, and A. Knohl (2014): 'Carbon isotope discrimination during branch photosynthesis of fagus sylvatica: Field measurements using laser spectrometry'. *Journal of Experimental Botany*, vol. 65(6): pp. 1481–1496 (cit. on pp. 4, 64).

Ghashghaie, J. and F. W. Badeck (2014): 'Opposite carbon isotope discrimination during dark respiration in leaves versus roots - a review'. *New Phytologist*, vol. 201(3): pp. 751–769 (cit. on p. 43).

Gillon, J. S. and D. Yakir (2000): 'Naturally low carbonic anhydrase activity in C_4 and C_3 plants limits discrimination against $C^{18}OO$ during photosynthesis'. *Plant, Cell and Environment*, vol. 23(9): pp. 201–213 (cit. on p. 43).

Good, S. P., K. Soderberg, L. Wang, and K. K. Caylor (2012): 'Uncertainties in the assessment of the isotopic composition of surface fluxes: A direct comparison of techniques using laser-based water vapor isotope analyzers'. *Journal of Geophysical Research*, vol. 117: p. D15301 (cit. on pp. 6, 7, 58, 61, 76, 78, 109).

Griffis, T. J. (2013): 'Tracing the flow of carbon dioxide and water vapor between the biosphere and atmosphere: A review of optical isotope techniques and their application'. *Agricultural and Forest Meteorology*, vol. 174-175: pp. 85–109 (cit. on pp. 4, 6, 7, 9, 10, 17, 18, 20, 56, 58, 109, 115).

Griffis, T. J., J. Zhang, J. M. Baker, N. Kljun, and K. Billmark (2007): 'Determining carbon isotope signatures from micrometeorological measurements: Implications for studying biosphere-atmosphere exchange processes'. *Boundary-Layer Meteorology*, vol. 123(2): pp. 295–316 (cit. on p. 6).

Griffis, T. J., S. D. Sargent, X. Lee, J. M. Baker, J. Greene, M. Erickson, X. Zhang, K. A. Billmark, N. Schultz, W. Xiao, and N. Hu (2010): 'Determining the oxygen isotope composition of evapotranspiration using eddy covariance'. *Boundary-Layer Meteorology*, vol. 137(2): pp. 307–326 (cit. on pp. 7, 58, 61, 73, 74, 76, 90–92, 96, 109).

Griffis, T. J., S. D. Sargent, J. M. Baker, X. Lee, B. D. Tanner, J. Greene, E. Swiatek, and K. Billmark (2008): 'Direct measurement of biosphere-atmosphere isotopic CO_2 exchange using the eddy covariance technique'. *Journal of Geophysical Research*, vol. 113(D8): p. D08304 (cit. on pp. 6, 7, 58, 113).

Griffis, T. J., J. D. Wood, J. M. Baker, X. Lee, K. Xiao, Z. Chen, L. R. Welp, N. M. Schultz, G. Gorski, M. Chen, and J. Nieber (2016): 'Investigating the source, transport, and isotope composition of water vapor in the planetary boundary layer'. *Atmospheric Chemistry and Physics*, vol. 16(8): pp. 5139–5157 (cit. on pp. 59, 92, 98, 100, 112–114).

Griffis, T. J., J. M. Baker, S. D. Sargent, B. D. Tanner, and J. Zhang (2004): 'Measuring field-scale isotopic CO_2 fluxes with tunable diode laser absorption spectroscopy and micrometeorological techniques'. *Agricultural and Forest Meteorology*, vol. 124(1-2): pp. 15–29 (cit. on p. 6).

Griffis, T. J., X. Lee, J. M. Baker, K. A. Billmark, N. Schultz, M. Erickson, X. Zhang, J. Fassbinder, W. Xiao, and N. Hu (2011): 'Oxygen isotope composition of evapotranspiration and its relation to C_4 photosynthetic discrimination'. *Journal of Geophysical Research*, vol. 116: G01035 (cit. on pp. 7, 58, 61, 90, 109, 113–115).

Griffith, D. W. T., N. M. Deutscher, C. Caldow, G. Kettlewell, M. Riggenbach, and S. Hammer (2012): 'A Fourier transform infrared trace gas and isotope analyser for atmospheric applications'. *Atmospheric Measurement Techniques*, vol. 5(10): pp. 2481–2498 (cit. on pp. 8, 20).

Griffiths, P. R., J. A. De Haseth, and J. D. Winefordner (2007): *Fourier transform infrared spectrometry*. Chemical analysis: A series of monographs on analytical chemistry and its applications. Wiley (cit. on p. 8).

Gröning, M., H. Lutz, Z. Roller-Lutz, M. Kralik, L. Gourcy, and L. Pöltenstein (2012): 'A simple rain collector preventing water re-evaporation dedicated for δ^{18}O and δ2H analysis of cumulative precipitation samples'. *Journal of Hydrology*, vol. 448-449: pp. 195–200 (cit. on pp. 68, 95).

Guillon, S., E. Pili, and P. Agrinier (2012): 'Using a laser-based CO_2 carbon isotope analyser to investigate gas transfer in geological media'. *Appl. Phys. B-Lasers O.* Vol. 107(2): pp. 449–457 (cit. on pp. 9, 20).

Hatfield, J. and J. Baker (2005): *Micrometeorology in agricultural systems*. Madison, WI, USA: American Society of Agronomy, Inc.: pp. 1–560 (cit. on p. 6).

Haverd, V., M. Cuntz, D. Griffith, C. Keitel, C. Tadros, and J. Twining (2011): 'Measured deuterium in water vapour concentration does not improve the constraint on the partitioning of evapotranspiration in a tall forest canopy, as estimated using a soil vegetation atmosphere transfer model'. *Agricultural and Forest Meteorology*, vol. 151(6): pp. 645–654 (cit. on pp. 8, 10).

Horst, T. W. and D. H. Lenschow (2009): 'Attenuation of scalar fluxes measured with spatially-displaced sensors'. *Boundary-Layer Meteorology*, vol. 130(2): pp. 275–300 (cit. on p. 69).

Hu, Z., X. F. Wen, X. Sun, L. Li, G. Yu, X. Lee, and S. Li (2014): 'Partitioning of evapotranspiration through oxygen isotopic measurements of water pools and fluxes in a temperate grassland'. *Journal of Geophysical Research: Biogeosciences*, vol. 119(3): pp. 358–372 (cit. on pp. 5, 6, 58, 61, 78, 81, 96).

Huang, L. and X. F. Wen (2014): 'Temporal variations of atmospheric water vapor δD and δ^{18}O above an arid artifical oasis cropland in the Heihe River Basin'. *Journal of Geophysical Research: Atmospheres*, vol. 119: pp. 11,456–11,476 (cit. on pp. 6, 61, 90–92, 96–98, 100, 112).

Ibrom, A., E. Dellwik, H. Flyvbjerg, N. O. Jensen, and K. Pilegaard (2007): 'Strong low-pass filtering effects on water vapour flux measurements with closed-path eddy correlation systems'. *Agricultural and Forest Meteorology*, vol. 147(3-4): pp. 140–156 (cit. on pp. 69, 76, 77).

International Atomic Energy Agency (1995): 'Reference and intercomparison materials for stable isotopes of light elements'. *Proceedings of a consultants meeting*. Ed. by IAEA. Vienna: IAEA–TECDOC–825 (cit. on p. 18).

International Radio Consultative Committee (1986): 'Characterization of frequency and phase noise'. *Report 580*: pp. 162–170 (cit. on p. 70).

Jasechko, S., Z. D. Sharp, J. J. Gibson, S. J. Birks, Y. Yi, and P. J. Fawcett (2013): 'Terrestrial water fluxes dominated by transpiration'. *Nature*, vol. 496(7445): pp. 347–350 (cit. on pp. 4, 91).

Jouzel, J., G. Hoffmann, R. Koster, and V. Masson (2000): 'Water isotopes in precipitation: data/model comparison for present-day and past climates'. *Quaternary Science Reviews*, vol. 19(1-5): pp. 363–379 (cit. on p. 90).

Kaimal, J. and J. Finnigan (1994): *Atmospheric boundary layer flows - their structure and measurement*. 1st ed. New York: Oxford Univesity Press, Inc (cit. on pp. 6, 58, 60, 73).

Keeling, C. D. (1958): 'The concentration and isotopic abundances of atmospheric carbon dioxide in rural areas'. *Geochimica et Cosmochimica Acta*, vol. 13(4): pp. 322–334 (cit. on pp. 5, 21, 58).

Kerstel, E. (2004): 'Isotope ratio infrared spectrometry'. *Handbook of stable isotope analytical techniques*. Ed. by Groot, P. de. 1st ed. Amsterdam, NE: Elsevier. Chap. 34: pp. 759–787 (cit. on p. 61).

Kerstel, E. and L. Gianfrani (2008): 'Advances in laser-based isotope ratio measurements: Selected applications'. *Appl. Phys. B-Lasers O.* Vol. 92(3): pp. 439–449 (cit. on pp. 8, 9, 17, 18, 63).

Knohl, A. and D. Baldocchi (2008a): 'Effects of diffuse radiation on canopy gas exchange processes in a forest ecosystem'. *Journal of Geophysical Research*, vol. 113: G02023 (cit. on p. 28).

Knohl, A., R. A. Werner, H. Geilmann, and W. A. Brand (2004): 'Kel-F^{TM} discs improve storage time of canopy air samples in 10-mL vials for CO_2-$\delta^{13}C$ analysis'. *Rapid Communications in Mass Spectrometry*, vol. 18(14): pp. 1663–1665 (cit. on p. 17).

Knohl, A. and N. Buchmann (2005a): 'Partitioning the net CO_2 flux of a deciduous forest into respiration and assimilation using stable carbon isotopes'. *Global Biogeochemical Cycles*, vol. 19(4): GB4008 (cit. on pp. 4, 16).

Knohl, A., A. R. B. Søe, W. L. Kutsch, M. Göckede, and N. Buchmann (2008b): 'Representative estimates of soil and ecosystem respiration in an old beech forest'. *Plant and Soil*, vol. 302(1-2): pp. 189–202 (cit. on p. 42).

Knohl, A., R. A. Werner, W. A. Brand, and N. Buchmann (2005b): 'Short-term variations in ^{13}C of ecosystem respiration reveals link between assimilation and respiration in a deciduous forest'. *Oecologia*, vol. 142(1): pp. 70–82 (cit. on pp. 5, 6, 17, 40, 109).

Kuzyakov, Y. and O. Gavrichkova (2010): 'Review: Time lag between photosynthesis and carbon dioxide efflux from soil: A review of mechanisms and controls'. *Global Change Biology*, vol. 16(12): pp. 3386–3406 (cit. on pp. 40, 41, 111).

Lai, C, J. R. Ehleringer, B. J. Bond, and K. T. P. U (2006): 'Contributions of evaparation, isotopic non-stedy state transpiration and atmospheric mixing on the $d^{18}O$ of water vapour in Pacific Northewest coniferous forests'. *Plant Cell Environ.* Vol. 29: pp. 77–94 (cit. on p. 95).

Lai, C. T. and J. R. Ehleringer (2011): 'Deuterium excess reveals diurnal sources of water vapor in forest air'. *Oecologia*, vol. 165(1): pp. 213–223 (cit. on pp. 62, 91, 92).

Lee, X., J. Huang, and E. G. Patton (2012a): 'A large-eddy simulation study of water vapour and carbon dioxide isotopes in the atmospheric boundary layer'. *Boundary-Layer Meteorology*, vol. 145(1): pp. 229–248 (cit. on pp. 6, 91, 92, 96, 97, 112).

Lee, X., T. J. Griffis, J. M. Baker, K. A. Billmark, K. Kim, and L. R. Welp (2009): 'Canopy-scale kinetic fractionation of atmospheric carbon dioxide and water vapor isotopes'. *Global Biogeochemical Cycles*, vol. 23: GB1002 (cit. on pp. 4, 62, 95, 113–115).

Lee, X., J. Huang, and E. G. Patton (2012b): 'Online supplement: A large-eddy simulation study of water vapour and carbon dioxide isotopes in the atmospheric boundary layer'. *Boundary-Layer Meteorology*, vol. 145(145): Supplement (cit. on p. 97).

Lee, X., K. Kim, and R. Smith (2007): 'Temporal variations of the $^{18}O/^{16}O$ signal of the whole-canopy transpiration in a temperate forest'. *Global Biogeochemical Cycles*, vol. 21: GB3013 (cit. on pp. 6, 58, 61, 78, 81, 90–92, 96, 100).

Lee, X., R. Smith, and J. Williams (2006): 'Water vapour $^{18}O/^{16}O$ isotope ratio in surface air in New England, USA'. *Tellus B*, vol. 58(4): pp. 293–304 (cit. on pp. 3, 6, 91, 92, 96, 100).

Lenschow, D. H., J. Mann, and L. Kristensen (1993): *How long is enough when measuring fluxes and other turbulence statistics?* Tech. rep. Boulder: National Center for Atmospheric Research: NCAR/TN–389+STR (cit. on p. 62).

– (1994): 'How long is long enough when measuring fluxes and other turbulence statistics?' *Journal of Atmospheric and Oceanic Technology*, vol. 11(3): pp. 661–673 (cit. on p. 62).

LiCor Biosciences (2016): *EddyPro (R) software instruction manual*. 12th ed. Lincoln: LI-COR, Inc.: 1–322, Document No. 977–12025 (cit. on pp. 62, 69, 74, 85, 94).

Lin, G., J. R. Ehleringer, P. T. Rygiewicz, M. G. Johnson, and D. T. Tingey (1999): 'Elevated CO_2 and temperature impacts on different components of soil CO_2 efflux in Douglas-fir terracosms'. *Global Change Biology*, vol. 5(2): pp. 157–168 (cit. on pp. 113, 114).

Los Gatos Research Inc. (2013): *Triple water vapor isotope analyzer (T-WVIA) - User manual - Model 912-0034*. 1.B. Mountain View: pp. 1–90 (cit. on pp. 10, 63, 94).

– (2012): *Water vapor isotope standard source with extended humidity range capability - User manual - Model 908-0004-9002 and 908-0004-9003*. 1.A. 908. Mountain View: pp. 1–28 (cit. on pp. 63, 64, 67, 94).

Lu, X., L. L. Liang, L. Wang, G. D. Jenerette, M. F. McCabe, and D. A. Grantz (2017): 'Partitioning of evapotranspiration using a stable isotope technique in an arid and high temperature agricultural production system'. *Agricultural Water Management*, vol. 179: pp. 103–109 (cit. on p. 5).

Majoube, M (1970): *Fractionation Factor of ^{18}O between Water Vapour and Ice.* (Cit. on p. 4).

– (1971): 'Fractionnement en oxygene 18 entre la glace et la vapeur d'eau'. *J. Chim. Phys.* Vol. 68(4): pp. 625–636 (cit. on p. 4).

Mann, J. and D. H. Lenschow (1994): 'Errors in airborne flux measurements'. *Journal of Geophysical Research*, vol. 99(D7): pp. 14519–14526 (cit. on p. 62).

Masarie, K. a., R. L. Langenfelds, C. E. Allison, T. J. Conway, E. J. Dlugokencky, R. J. Francey, P. C. Novelli, L. P. Steele, P. P. Tans, B. Vaughn, and J. W. C. White (2001): 'NOAA/CSIRO Flask Air Intercomparison Experiment: A strategy for directly assessing consistency among atmospheric measurements made by independent laboratories'. *Journal of Geophysical Research*, vol. 106(D17): p. 20445 (cit. on p. 109).

McDonnell, J. J. (2014): 'The two water worlds hypothesis: Ecohydrological separation of water between streams and trees?' *Wiley Interdisciplinary Reviews: Water (WIREs)*, vol. 1: pp. 324–329 (cit. on p. 90).

Meissner, M., M. Köhler, L. Schwendenmann, D. Hölscher, and J. Dyckmans (2014): 'Soil water uptake by trees using water stable isotopes (δ^2H and $\delta^{18}O$)-a method

test regarding soil moisture, texture and carbonate'. *Plant and Soil*, vol. 376(1-2): pp. 327–335 (cit. on pp. 5, 59, 113, 114).

Michener, R. H. and K. Lajtha (2007): *Stable isotopes in ecology and environmental science* (cit. on p. 91).

Miller, J. B. and P. P. Tans (2003): 'Calculating isotopic fractionation from atmospheric measurements at various scales'. *Tellus, Series B: Chemical and Physical Meteorology*, vol. 55: pp. 207–214 (cit. on pp. 5, 6).

Miller, J. B., D. Yakir, J. W. C. White, and P. P. Tansl (1999): 'Measurement of $^{18}O/^{16}O$ in the soil-atmosphere CO_2 flux'. *Global Biogeochemical Cycles*, vol. 13(3): pp. 761–774 (cit. on pp. 43, 44, 110).

Mohn, J., M. J. Zeeman, R. A. Werner, W. Eugster, and L. Emmenegger (2008): 'Continuous field measurements of delta ^{13}C-CO_2 and trace gases by FTIR spectroscopy.' *Isotopes in environmental and health studies*, vol. 44(3): pp. 241–51 (cit. on p. 17).

Mohn, J., R. A. Werner, B. Buchmann, and L. Emmenegger (2007): 'High-precision $\delta^{13}CO_2$ analysis by FTIR spectroscopy using a novel calibration strategy'. *Journal of Molecular Structure*, vol. 834-836(SPEC. ISS.): pp. 95–101 (cit. on p. 20).

Moncrieff, J., J. Massheder, H. de Bruin, J. Elbers, T. Friborg, B. Heusinkveld, P. Kabat, S. Scott, H. Soegaard, and A. Verhoef (1997a): 'A system to measure surface fluxes of momentum, sensible heat, water vapour and carbon dioxide'. *Journal of Hydrology*, vol. 188-189: pp. 589–611 (cit. on pp. 76, 77, 86, 95, 110).

Moncrieff, J., R. Clement, J. Finnigan, and T. Meyers (2005): 'Averaging, detrending, and filtering of eddy covariance time series'. *Handbook of Micrometeorology*, vol. 29: pp. 7–31 (cit. on p. 69).

Moncrieff, J., R. Valentini, S. Greco, S. Guenther, and P. Ciccioli (1997b): 'Trace gas exchange over terrestrial ecosystems: Methods and perspectives in micrometeorology'. *Journal of Experimental Botany*, vol. 48(5): pp. 1133–1142 (cit. on p. 2).

Monin, A. S. and A Obukhov (1954): 'Basic laws of turbulent mixing in the surface layer of the atmosphere'. *Tr. Akad. Nauk SSSR Geophiz. Inst.* Vol. 151: pp. 163–187 (cit. on pp. 6, 58).

Moreira, M., L. Sternberg, L. Martinelli, R. Victoria, E. Barbosa, L. Bonates, and D. Nepstad (1997): 'Contribution of transpiration to forest ambient vapour based on isotopic measurements'. *Global Change Biology*, vol. 3(5): pp. 439–450 (cit. on p. 6).

Moyano, F, O. Atkin, M Bahn, D Bruhn, A Burten, and A. Heinemeyer (2009): 'Respiration from roots and the mycorrhizosphere'. *Soil carbon dynamics*. Cambridge University Press (cit. on pp. 2, 42).

Moyano, F. E., W. L. Kutsch, and C. Rebmann (2008): 'Soil respiration fluxes in relation to photosynthetic activity in broad-leaf and needle-leaf forest stands'. *Agricultural and Forest Meteorology*, vol. 148(1): pp. 135–143 (cit. on p. 42).

Mund, M. (2004): 'Carbon pools of European beech forests (Fagus sylvatica) under different silvicultural management'. *Berichte des Forschungszentrums Waldökosysteme Reihe A*, vol. Band 189: pp. 1–256 (cit. on p. 21).

NIST (2005): *Report of investigation: Reference materials 8535, 8536, 8537*. Tech. rep. Gaithersburg: National Institute of Standards and Technology: pp. 1–5 (cit. on p. 60).

Noone, D., C. Risi, A. Bailey, M. Berkelhammer, D. P. Brown, N. Buenning, S. Gregory, J. Nusbaumer, D. Schneider, J. Sykes, B. Vanderwende, J. Wong, Y. Meillier, and D. Wolfe (2013): 'Determining water sources in the boundary layer from tall tower profiles of water vapor and surface water isotope ratios after a snowstorm in Colorado'. *Atmospheric Chemistry and Physics*, vol. 13(3): pp. 1607–1623 (cit. on pp. 6, 91, 92).

Ogée, J., P. Peylin, P. Ciais, T. Bariac, Y. Brunet, P. Berbigier, C. Roche, P. Richard, G. Bardoux, and J.-M. Bonnefond (2003): 'Partitioning net ecosystem carbon exchange into net assimilation and respiration using $^{13}CO_2$ measurements: A cost-effective sampling strategy'. *Global Biogeochemical Cycles*, vol. 17(2): pp. 3901–3916 (cit. on pp. 4, 16).

Oikawa, P., C. Sturtevant, S. H. Knox, J. Verfaillie, Y.-W. Huang, and D. Baldocchi (2017): 'Revisiting the partitioning of net ecosystem exchange of CO_2 into photosynthesis and respiration with simultaneous flux measurements of $^{13}CO_2$ and CO_2, soil respiration and a biophysical model, CANVEG'. *Agricultural and Forest Meteorology*, vol. 234-235: pp. 149–163 (cit. on pp. 5, 16, 20, 58).

Orlowski, N., P. Kraft, J. Pferdmenges, and L. Breuer (2016): 'Exploring water cycle dynamics by sampling multiple stable water isotope pools in a developed landscape in Germany'. *Hydrology and Earth System Sciences*, vol. 20(9): pp. 3873–3894 (cit. on p. 44).

Pataki, D. E., J. R. Ehleringer, L. B. Flanagan, D. Yakir, D. R. Bowling, C. Still, N. Buchmann, J. O. Kaplan, and J. A. Berry (2003): 'The application and interpretation of Keeling plots in terrestrial carbon cycle research'. *Global Biogeochemical Cycles*, vol. 17(1): pp. 2201–2214 (cit. on pp. 5, 6, 22, 48, 58).

Paya, A. M., T. E. E. Grams, and T. L. Bauerle (2016): 'Seasonal dynamics of $\delta^{13}C$ of C-rich fractions from Picea abies (Norway spruce) and Fagus sylvatica (European beech) fine roots'. *Plant, Cell and Environment*, vol. 39(9): pp. 2004–2013 (cit. on p. 43).

Phillips, D. L. and J. W. Gregg (2001): 'Uncertainty in source partitioning using stable isotopes'. *Oecologia*, vol. 127(2): pp. 171–179 (cit. on p. 113).

Rizzo, A., H.-J. Jost, A. Caracausi, A. Paonita, M. Liotta, and M. Martelli (2014): 'Real-time measurements of the concentration and isotope composition of atmospheric and volcanic CO_2 at Mount Etna (Italy)'. *Geophysical Research Letters*, vol. 41(7): pp. 2382–2389 (cit. on p. 9).

Rosenberg, N. J. (1974): 'Evapotranspiration'. *Microclimate: The biological environment*. New York: John Wiley & Sons,Inc. Chap. 7: pp. 159–205 (cit. on pp. 2, 3).

Rothman, L. S. et al. (2013): 'The HITRAN2012 molecular spectroscopic database'. *Journal of Quantitative Spectroscopy and Radiative Transfer*, vol. 130: pp. 4–50 (cit. on p. 60).

Rothman, L. et al. (2003): 'The HITRAN molecular spectroscopic database: Edition of 2000 including updates through 2001'. *Journal of Quantitative Spectroscopy and Radiative Transfer*, vol. 82: pp. 5–44 (cit. on p. 60).

Saleska, S. T., M. Chamecki, and N. L. Dias (2012): 'Estimating the random error in eddy-covariance based fluxes and other turbulence statistics: The filtering method'. *Boundary-Layer Meteorology*, vol. 144(1): pp. 113–135 (cit. on p. 62).

Savage, K., E. A. Davidson, and J. Tang (2013): 'Diel patterns of autotrophic and heterotrophic respiration among phenological stages'. *Global Change Biology*, vol. 19(4): pp. 1151–1159 (cit. on p. 42).

Schimel, D. (1995): 'Terrestrial ecosystems and the carbon cycle'. *Global change biology*, vol. 1: pp. 77–91 (cit. on p. 4).

Schnyder, H., R. Schäufele, and R. Wenzel (2004): 'Mobile, outdoor continuous-flow isotope-ratio mass spectrometer system for automated high-frequency ^{13}C- and ^{18}O-CO_2 analysis for Keeling plot applications'. *Rapid Communications in Mass Spectrometry*, vol. 18(24): pp. 3068–3074 (cit. on p. 17).

Schotanus, P, F. T. M. Nieuwstadt, and H. A. R. De Bruin (1983): 'Temperature measurement with a sonic anemometer and its application to heat and moisture fluxes'. *Boundary-Layer Meteorology*, vol. 26(1): pp. 81–93 (cit. on p. 69).

Sevastyanov, V. (2015): 'Isotope ratio mass spectrometry: Devices, methods, applications'. *Isotope Ratio Mass Spectrometry of Light Gas-Forming Elements*. Ed. by V.S. Sevastyanov. Boca Raton, FL, USA: CRC Press, Taylor and Francis Group. Chap. 1: pp. 1–118 (cit. on p. 7).

Shim, J. H., H. H. Powers, C. W. Meyer, A. Knohl, T. E. Dawson, W. J. Riley, W. T. Pockman, and N. McDowell (2013): 'Hydrologic control of the oxygen isotope ratio of ecosystem respiration in a semi-arid woodland'. *Biogeosciences*, vol. 10: pp. 4937–4956 (cit. on pp. 6, 17, 43).

Stull, R. (1988): *An introduction to boundary layer meteorology*. 1997th ed. Dordrecht: Kluwer Academic Publishers (cit. on pp. 3, 7, 60, 73).

Sturm, P., W. Eugster, and A. Knohl (2012): 'Eddy covariance measurements of CO_2 isotopologues with a quantum cascade laser absorption spectrometer'. *Agricultural and Forest Meteorology*, vol. 152: pp. 73–82 (cit. on pp. 7, 8, 20, 32, 58, 62, 95, 109).

Sturm, P., B. Tuzson, S. Henne, and L. Emmenegger (2013): 'Tracking isotopic signatures of CO_2 at the high altitude site Jungfraujoch with laser spectroscopy: Analytical improvements and representative results'. *Atmospheric Measurement Techniques*, vol. 6(7): pp. 1659–1671 (cit. on pp. 32, 109).

Sturm, P. and A. Knohl (2009): 'Water vapor δ^2H and δ^{18}O measurements using off-axis integrated cavity output spectroscopy'. *Atmospheric Measurement Techniques Discussions*, vol. 2(4): pp. 2055–2085 (cit. on pp. 9, 10, 64, 70, 72).

Thermo Fisher Scientific (2014): *Delta RayTM Isotope ratio infrared spectrometer: Operating manual*. Bremen: Thermo Scientific (cit. on pp. 9, 19).

Thomson, J. J. (1908): 'Rays of positive electricity'. *Nature*, vol. 79(2037): pp. 52–56 (cit. on pp. 7, 17).

Tuzson, B., J. Mohn, M. J. Zeeman, R. A. Werner, W. Eugster, M. S. Zahniser, D. D. Nelson, J. B. McManus, and L. Emmenegger (2008): 'High precision and continuous field measurements of δ^{13}C and δ^{18}O in carbon dioxide with a cryogen-free QCLAS'. *Appl. Phys. B-Lasers O.* Vol. 92(3): pp. 451–458 (cit. on pp. 6, 17, 30, 71, 108).

Twining, J., D. Stone, C. Tadros, A. Henderson-Sellers, and A. Williams (2006): 'Moisture isotopes in the biosphere and atmosphere (MIBA) in Australia: A priori estimates and preliminary observations of stable water isotopes in soil, plant and vapour

for the Tumbarumba field campaign'. *Global and Planetary Change*, vol. 51(1-2): pp. 59–72 (cit. on pp. 81–83).

Vardag, S. N., S. Hammer, M. Sabasch, D. W. T. Griffith, and I. Levin (2015): 'First continuous measurements of δ^{18}O-CO_2 in air with a Fourier transform infrared spectrometer'. *Atmospheric Measurement Techniques*, vol. 8(2): pp. 579–592 (cit. on pp. 8, 20).

Vickers, D. and L Mahrt (1997): 'Quality control and flux sampling problems for tower and aircraft data'. *Journal of Atmospheric and Oceanic Technology*, vol. 14(3): pp. 512–526 (cit. on p. 69).

Vogel, F. R., L. Huang, D. Ernst, L. Giroux, S. Racki, and D. E. J. Worthy (2013): 'Evaluation of a cavity ring-down spectrometer for in situ observations of $^{13}CO_2$'. *Atmospheric Measurement Techniques*, vol. 6(2): pp. 301–308 (cit. on pp. 9, 20, 32, 109).

Wang, L., K. K. Caylor, J. C. Villegas, G. A. Barron-Gafford, D. D. Breshears, and T. E. Huxman (2010): 'Partitioning evapotranspiration across gradients of woody plant cover: Assessment of a stable isotope technique'. *Geophysical Research Letters*, vol. 37(9): pp. 1–7 (cit. on pp. 4, 56).

Wang, P., X.-Y. Li, Y. Huang, S. Liu, Z. Xu, X. Wu, and Y.-J. Ma (2016): 'Numerical modeling the isotopic composition of evapotranspiration in an arid artificial oasis cropland ecosystem with high-frequency water vapor isotope measurement'. *Agricultural and Forest Meteorology*, vol. 230-231: pp. 79–88 (cit. on pp. 6, 61).

Wang, P., T. Yamanaka, X.-Y. Li, and Z. Wei (2015): 'Partitioning evapotranspiration in a temperate grassland ecosystem: Numerical modeling with isotopic tracers'. *Agricultural and Forest Meteorology*, vol. 208(August): pp. 16–31 (cit. on p. 5).

Wang, X.-F. and D. Yakir (2000): 'Using stable isotopes in evapotranspiration studies'. *Hydrological Processes*, vol. 14: pp. 1407–1421 (cit. on pp. 4, 56).

Wassenaar, L. I., M. Ahmad, P. Aggarwal, M. Van Duren, L. Pöltenstein, L. Araguas, and T. Kurttas (2012): 'Worldwide proficiency test for routine analysis of δ^2H and δ^{18}O in water by isotope-ratio mass spectrometry and laser absorption spectroscopy'. *Rapid Communications in Mass Spectrometry*, vol. 26(15): pp. 1641–1648 (cit. on pp. 73, 109).

Webb, E. K., G. I. Pearman, and R Leuning (1980): 'Correction of flux measurements for density effects due to heat and water vapour transfer'. *Quarterly Journal of the Royal Meteorological Society*, vol. 106(447): pp. 85–100 (cit. on p. 69).

Wehr, R., J. Munger, D. Nelson, J. McManus, M. Zahniser, S. Wofsy, and S. Saleska (2013): 'Long-term eddy covariance measurements of the isotopic composition of the ecosystem-atmosphere exchange of CO_2 in a temperate forest'. *Agricultural and Forest Meteorology*, vol. 181: pp. 69–84 (cit. on pp. 7, 20, 58, 60–62).

Wehr, R., J. W. Munger, J. B. McManus, D. D. Nelson, M. S. Zahniser, E. A. Davidson, S. C. Wofsy, and S. R. Saleska (2016): 'Seasonality of temperate forest photosynthesis and daytime respiration'. *Nature*, vol. 534(7609): pp. 680–683 (cit. on pp. 5, 8, 16, 17, 58).

Wehr, R. and S. R. Saleska (2017): 'The long-solved problem of the best-fit straight line: Application to isotopic mixing lines'. *Biogeosciences*, vol. 14(17): pp. 1–19 (cit. on pp. 72, 76).

Wei, Z., K. Yoshimura, A. Okazaki, W. Kim, Z. Liu, and M. Yokoi (2015): 'Partitioning of evapotranspiration using high-frequency water vapor isotopic measurement over a rice paddy field'. *Water Resources Research*, vol. 51(5): pp. 3716–3729 (cit. on pp. 5, 58).

Welp, L. R., X. Lee, T. J. Griffis, X. F. Wen, W. Xiao, S. Li, X. Sun, Z. Hu, M. Val Martin, and J. Huang (2012): 'A meta-analysis of water vapor deuterium-excess in the midlatitude atmospheric surface layer'. *Global Biogeochemical Cycles*, vol. 26: GB3021 (cit. on pp. 59, 91, 92, 98, 113, 114).

Welp, L. R., X. Lee, K. Kim, T. J. Griffis, K. A. Billmark, and J. M. Baker (2008): 'δ^{18}O of water vapour, evapotranspiration and the sites of leaf water evaporation in a soybean canopy'. *Plant, Cell and Environment*, vol. 31(9): pp. 1214–1228 (cit. on pp. 6, 58, 61, 81, 90–92, 96, 100, 112, 113).

Wen, X. F., X. M. Sun, S. C. Zhang, G. R. Yu, S. D. Sargent, and X. Lee (2008): 'Continuous measurement of water vapor D/H and ^{18}O/^{16}O isotope ratios in the atmosphere'. *Journal of Hydrology*, vol. 349(3-4): pp. 489–500 (cit. on pp. 9, 10).

Wen, X. F., B. Yang, X. Sun, and X. Lee (2016): 'Evapotranspiration partitioning through in-situ oxygen isotope measurements in an oasis cropland'. *Agricultural and Forest Meteorology*, vol. 230-231: pp. 89–96 (cit. on pp. 5, 6, 58, 61).

Wen, X. F., S. C. Zhang, X. M. Sun, G. R. Yu, and X. Lee (2010): 'Water vapor and precipitation isotope ratios in Beijing, China'. *Journal of Geophysical Research Atmospheres*, vol. 115: p. D01103 (cit. on pp. 90, 92, 100).

Wendeberg, M., J. M. Richter, M. Rothe, and W. A. Brand (2013): 'Jena Reference Air Set (JRAS): A multi-point scale anchor for isotope measurements of CO_2 in air'. *Atmospheric Measurement Techniques*, vol. 6(3): pp. 817–822 (cit. on p. 25).

Wenninger, J., P. Koeninger, and P. Schneider (2011): 'Isotopic characterization of snow variability in two mountainous catchments, black forest mountains, Germany'. *International Symposium on Water Resource and Environmental Protection (ISWREP)*: pp. 1004–1007 (cit. on p. 44).

Werle, P, R Miicke, and F Slemr (1993): 'The limits of signal averaging in atmospheric trace-gas monitoring by tunable diode-laser absorption spectroscopy (TDLAS)'. *Appl. Phys. B: Photophys. Laser Chem.* Vol. 57: pp. 131–139 (cit. on p. 70).

Werle, P. W. (2004): 'Diode-laser sensors for in-situ gas analysis'. *Laser in Environmental and Life Sciences: Modern Analytical Methods*. Ed. by Hering, P., J. P. Lay, and S. Stry. Berlin, Heidelberg: Springer: pp. 223–243 (cit. on pp. 8, 17, 18).

Werner, C. et al. (2012): 'Progress and challenges in using stable isotopes to trace plant carbon and water relations across scales'. *Biogeosciences*, vol. 9(8): pp. 3083–3111 (cit. on pp. 7, 17, 58).

Williams, D. G., W. Cable, K. Hultine, J. C. B. Hoedjes, E. A. Yepez, V. Simonneaux, S. Er-Raki, G. Boulet, H. A. R. De Bruin, A. Chehbouni, O. K. Hartogensis, and F. Timouk (2004): 'Evapotranspiration components determined by stable isotope, sap flow and eddy covariance techniques'. *Agricultural and Forest Meteorology*, vol. 125(3-4): pp. 241–258 (cit. on p. 58).

Wingate, L., U. Seibt, K. Maseyk, J. Ogée, P. Almeida, D. Yakir, J. S. Pereira, and M. Mencuccini (2008): 'Evaporation and carbonic anhydrase activity recorded in

oxygen isotope signatures of net CO_2 fluxes from a Mediterranean soil'. *Global Change Biology*, vol. 14(9): pp. 2178–2193 (cit. on p. 114).

Wingate, L. et al. (2009): 'The impact of soil microorganisms on the global budget of $\delta^{18}O$ in atmospheric CO_2'. *Proceedings of the National Academy of Sciences*, vol. 106(52): pp. 22411–22415 (cit. on pp. 43, 44, 113, 114).

Xu, T., S. M. Bateni, S. A. Margulis, L. Song, S. Liu, and Z. Xu (2016): 'Partitioning evapotranspiration into soil evaporation and canopy transpiration via a two-source variational data assimilation system'. *Journal of Hydrometeorology*, vol. 17(9): pp. 2353–2370 (cit. on p. 5).

Yakir, D. and X.-F. Wang (1996): 'Fluxes of CO_2 and water between terrestrial vegetation and the atmosphere estimated from isotope measurements'. *Nature*, vol. 380(6574): pp. 515–517 (cit. on pp. 5, 16, 17, 58).

Yakir, D. and L. d.S. L. Sternberg (2000): 'The use of stable isotopes to study ecosystem gas exchange'. *Oecologia*, vol. 123(3): pp. 297–311 (cit. on pp. 4, 16, 56, 90).

Yepez, E. A., D. G. Williams, R. L. Scott, and G. Lin (2003): 'Partitioning overstory and understory evapotranspiration in a semiarid savanna woodland from the isotopic composition of water vapor'. *Agricultural and Forest Meteorology*, vol. 119(1-2): pp. 53–68 (cit. on pp. 5, 6).

York, D. (1968): 'Least-squares fitting of a straight line'. *Canadian Journal of Physics*, vol. 46(16): pp. 1845–1847 (cit. on pp. 72, 76).

Zhang, J., T. J. Griffis, and J. M. Baker (2006): 'Using continuous stable isotope measurements to partition net ecosystem CO_2 exchange'. *Plant, Cell and Environment*, vol. 29(4): pp. 483–496 (cit. on pp. 5, 6, 16).

Zhang, S., X. Sun, J. Wang, G. Yu, and X. F. Wen (2011): 'Short-term variations of vapor isotope ratios reveal the influence of atmospheric processes'. *Journal of Geographical Sciences*, vol. 21(3): pp. 401–416 (cit. on pp. 91, 96, 97, 100, 112).

Zobitz, J., J. Keener, H. Schnyder, and D. R. Bowling (2006): 'Sensitivity analysis and quantification of uncertainty for isotopic mixing relationships in carbon cycle research'. *Agricultural and Forest Meteorology*, vol. 136(1-2): pp. 56–75 (cit. on pp. 5, 47, 48).

List of Figures

List of Tables

Acknowledgments

I would like to thank Alexander Knohl for supervising this PhD thesis as well as for his support and advice during the last years. I am very grateful for the scientific discussions and encouragement from him and the other members of thesis committee Dave Bowling, Dirk Hölscher and Lukas Siebicke.

The research presented in this thesis was partly financed by the Dorothea-Schlözer-Fellowship, the German Research Foundation (DFG, project ISOFLUXES KN 582/7-1), the European Research Council under the European Union's Horizon 2020 research and innovation programme (grant agreement no. 682512 – OXYFLUX), the German federal ministry of education and research (BMBF, project BonaRes, Modul A: Signal 031A562A) and the bioclimatology group of the faculty of forest sciences and forest ecology of the University of Göttingen.

I thank the whole bioclimatology group of the faculty of forest sciences and forest ecology of the University of Göttingen for the great willingness to support my work with both field work and scientific discussions as well as administration. In particular the collaboration with the additional coauthors of chapter 2 (Yuan Yan) and chapter 3 (Christian Markwitz) of this thesis was very constructive and fruitful. I am really happy to have Christian Stiegler as an office-mate, who also supported me a lot. The extensive experimental installations that needed to be set up for this work would not have been possible without the major support by the technicians of the bioclimatology group, Dietmar Fellert, Frank Tiedemann, Edgar Tunsch and Claudia Schulz. Additionally the student assistants Martin Lindenberg, Elke Schäpermeier and Raphael Tubbesing helped substantially with setup and maintenance of the experiments. Additionally I want to thank the forest manager Ulrich Breitenstein for allowing the large experimental setup for this long period.

The layout of this thesis is based on a LaTeX-Template by Matthias Pospiech http://www.matthiaspospiech.de/latex/ and I am very thankful that he shared it.

For a lot of support, that cannot be easily put into words, I would like to thank my husband Christoph Behrens and my family. In particular, I want to thank my parents Heiner Braden and Ingrid Weyers-Braden and my grandparents Elsbeth Weyers, Elisabeth Braden, Hubert Weyers and Dr. Franz Braden, who always supported my education and studies in many ways.